POLITECNICO DI MILANO

Master of Science in Materials Engineering and Nanotechnology

School of Industrial and Information Engineering

Binder Jetting 3D Printing of Copper

Supervisor: Prof.ssa Nora Lecis

Co-Supervisor: Eng. Marco Mariani

Master Thesis Candidate:

Simone Pisani

ID: 919792

Academic Year 2020-2021

Table of contents

List of figures

List of tables

Abstract

Binder Jetting is a non-fusion based additive manufacturing technique which consists in the selective deposition of a liquid binder layer-by-layer on a powder bed to obtain non-conventional geometries. After printing, several post-processing techniques are performed: curing to obtain sufficient strength for cleaning and handling of the green, debinding which burns out polymeric binder and sintering to achieve the desired densification and mechanical properties.

In this thesis work, pure copper parts were printed with an Innovent+ 3D printer by ExOne. A study to assess the best printing parameters, as the optimal value of binder saturation, and the best post-processing thermal cycle to obtain adequate values of densification was realized.
The solid-state sintering mechanisms were studied through dilatometry analysis performed at different temperatures and controlled atmospheres. Finally, all the specimens were observed with optical microscopy and scanning electron microscopy (SEM) to evaluate the microstructure.

The highest values of final relative density were obtained with separate debinding and sintering treatments: the former is executed in argon atmosphere, while the latter is performed in vacuum at 1000 °C, with a holding time of 3 hours.
Finally, the possibility of a sintering treatment in air in presence of graphite was explored as a viable alternative to more complex and expensive procedures.

Keywords

Binder Jetting, Additive Manufacturing, Copper, Dilatometry, Thermal Treatment, Sintering.

Riassunto

Il Binder Jetting è una tecnica di manifattura additiva senza fusione che consiste nella deposizione selettiva di un legante liquido strato per strato su un letto di polvere e permette di ottenere pezzi con varie geometrie. Al termine della stampa, è necessario effettuare alcuni trattamenti termici: il trattamento di curing permette di ottenere pezzi verdi abbastanza resistenti per essere maneggiati e per eliminare la polvere in eccesso, successivamente con il debinding il legante polimerico viene bruciato ed eliminato. Infine, si esegue il trattamento di sinterizzazione così da aumentare la densità e le proprietà meccaniche del componente.

In questo lavoro di tesi, sono stati stampati dei pezzi di rame puro con la stampante 3D Innovent+ 3D della ExOne al fine di trovare i parametri di stampa migliore, in particolare il valore di saturazione del legante, e il migliore ciclo termico in modo da ottenere buoni valori di densità. Sono stati studiati i meccanismi di sinterizzazione allo stato solido tramite analisi di dilatometria eseguite a diverse temperature e in diverse atmosfere. Infine, tutti i campioni sono stati osservati con il microscopio ottico e il microscopio elettronico a scansione (SEM) per valutare la microstruttura.

I risultati migliori per quanto riguarda la densità relativa del pezzo finale sono stati ottenuti grazie alla separazione dei trattamenti di debinding e sinterizzazione: il primo è stato eseguito in un'atmosfera contenente argon, invece il secondo è stato compiuto in vuoto a 1000 °C con un mantenimento di 3 ore.
Infinte, la possibilità di effettuare il trattamento di sinterizzazione in aria in presenza di grafite è stata studiata come alternativa a procedure più complesse e costose.

Parole chiave

Binder Jetting, Manifattura Additiva, Rame, Dilatometria, Trattamento Termico, Sinterizzazione.

1. Introduction

1.1. Copper

Copper and copper alloys are one of the major groups of commercial metals. They are widely employed for their exceptional thermal and electrical conductivities, ease of fabrication and good mechanical properties [1].

Pure copper is mostly used for cables, wires and electrical contacts. Copper alloys are generally not used for electrical applications because the added elements reduce the electrical conductivity of pure copper, depending on their concentrations and positions in the crystalline lattice.
Indeed, these will scatter electrons and consequently decrease electrical conductivity: for example, solute elements cause a local strain due to the fact that their atomic size is different, producing scattering of electrons and hence decreasing conductivity [1].
In addition, if the alloying element creates a second phase with copper, electrical conductivity is reduced as result of the decrease of volume where the current can pass, as can be seen in Figure 1 [2]. This typically occurs when oxygen combines with copper, forming CuO and Cu_2O oxides.
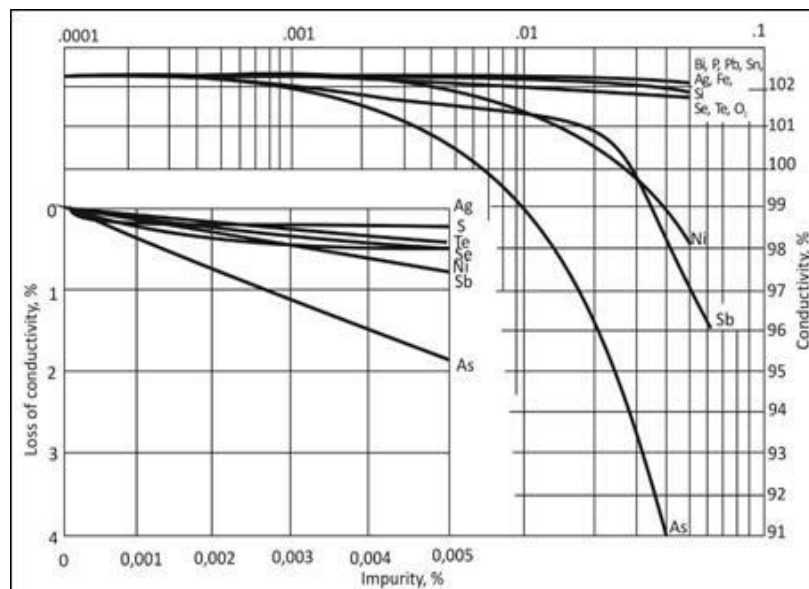
Figure 1 - Decrease in electrical conductivity of copper in the function of impurity content. From [2].

Regarding thermal properties, the reduction of thermal conductivity of copper has the same trend of electrical conductivity because solutes increase the metal specific heat, and thus its enthalpy and free energy [1].
The melting point of pure copper is around 1083 °C, but it may varies as shown in Figure 2 [3].

Concerning the mechanical properties, copper is considered a soft and ductile metal [1].
The strength and hardness of copper can be improved by alloying, although it results in a reduction of conductivity, as mentioned before.
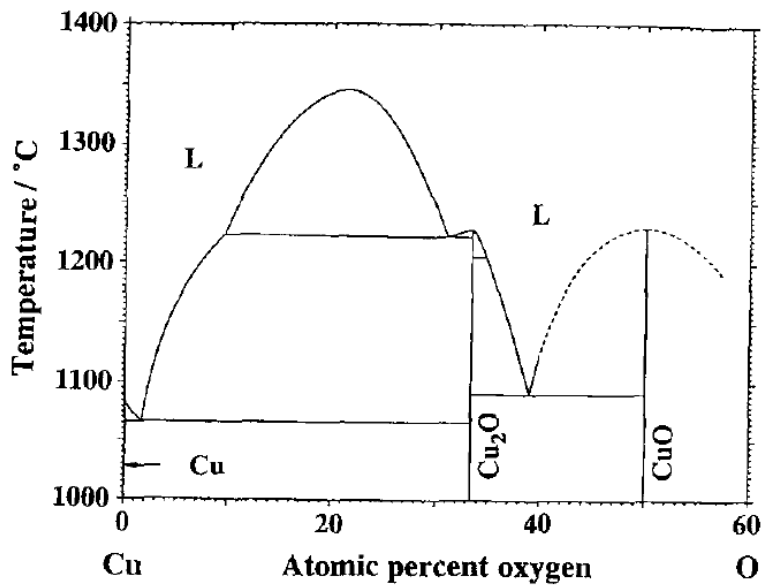
Figure 2 - Phase diagram of the copper-oxygen system. From [3].

Copper can form two different oxides [4].

The first one is cuprous oxide Cu_2O, also known as cuprite. It has a cubic structure, where copper atoms arrange in a fcc sublattice and oxygen atoms in a bcc sublattice. It is characterized by a red or yellow color, depending on the size of the particles.

The other compound is cupric oxide CuO, also called tenorite. It assumes a monoclinic structure, where the copper atom is coordinated by 4 oxygen atoms in a square planar configuration and has a typical black color.

1.2.   Powder metallurgy

Powder metallurgy is a term used to define different operating processes in which the starting material is metal powder.

Generally, powder metallurgy processing consists of powder production, blending of powder with additives like solid lubricants, powder compaction and consolidation through pressing and sintering. Optional secondary and finishing processing can be done in order to obtain particular properties [5].

Powder metallurgy allows to produce parts with controlled density, adequate dimensional and surface quality and suitable mechanical properties.

Despite these advantages, powder metallurgy processes may not be economically advantageous due to high cost of the initial raw material and the mold and the need of secondary operations [6].

In addition, powders have high surface area to volume ratio, so they are very reactive and can be used as catalysts in various chemical or metallurgical reactions [7].

1.2.1. Production of metal powders

There are four major methods of producing metal powders [1].

In case of copper, the most used and established technique is the reduction of particular copper oxide inside a continuous bell furnace performed at medium-high temperature, from 425 to 650 °C. The reducing gases are a mixture of hydrogen, dissociated ammonia, carbon monoxide and water-reformed natural gases. Hydrogen is very effective, especially at low temperature. The obtained

product is a porous cake, like a sponge, and it is broken in a jaw crusher and grinded finely in hammer mills [1].

Alternatively, electrolysis is widely used in the production of copper powders for specialist applications since high purity materials can be obtained and it is more expensive compared to the other methods.
The process is performed in an electrolytic cell, consisting of a lead cathode, a copper anode and copper sulfate as the electrolyte. It is possible to vary operating conditions to affect the final product.
If the cathode current density is high and the electrolyte is characterized by high acid content and low copper ion concentration, a formation of powdery deposit is favored. High temperature increases the current efficiency and reduces the cell voltage.
The final product deposits on the cathode, so it is necessary to remove it in a mechanical way by brushing [1].

In atomization processes, the metal is melted and broken up into small droplets which are rapidly frozen and solidify before coming in contact with each other or with a surface. The thin stream of molten metal is usually disintegrated with a jet of water or gas, like air, nitrogen and argon, as can be seen in Fig. 3 [8]. Generally, water atomized powder have less regular particle shape, while it is possible to obtain nearly spherical particles with atomization by inert gas or air [1]. This technique is the most relevant for the production of raw material for additive manufacturing, given the extremely fine control on both particles shape and size distribution.
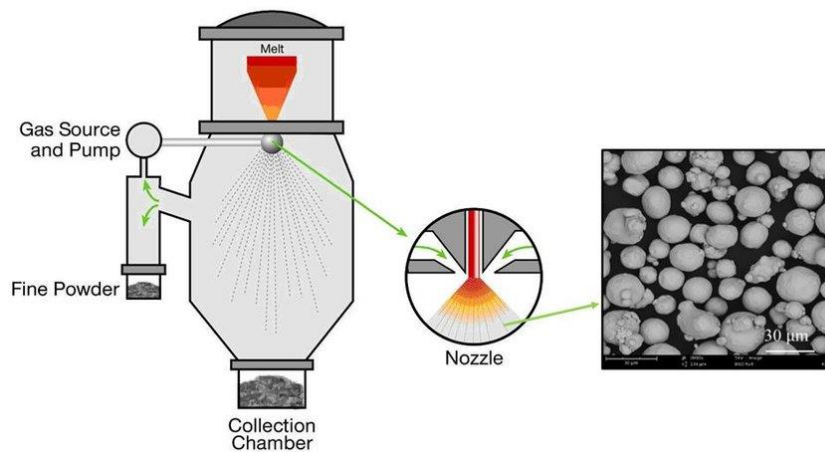
Figure 3 - Scheme of atomization system for powder production. From [8].

Hydrometallurgical methods consist of the preparation of a solution, followed by the precipitation of the metal.
The most used precipitation method is cementation, which is the precipitation of a metal from a solution by adding a less noble metal. In case of copper, scrap iron, for example detinned and shredded cans, is added to the solution, in order to obtain the following equation:

$$Fe + CuSO4 = Cu + FeSO4 \qquad (1)$$
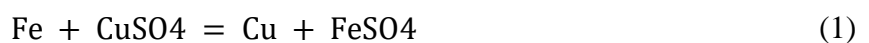
Then, separation, washing and pulverizing are done in order to eliminate impurities and to obtain the desired powder [1].

After their production, metal powders are blended with other materials if an alloy is the final goal or mixed with some additives like solid lubricant.

1.2.2. Compaction of powders

The next step is the compaction of powders: it is usually performed by uniaxial pressing in a closed die and with pressure depending on the material.
The compacting press can be mechanical or hydraulic [7].
Usually, for pure copper parts, the pressure is around 205 to 250 MPa, but the value depends on the part geometry and also on the particle shape and size distribution [1].

The green density achieved after compaction should be sufficient to provide suitable green strength for the handling of parts, but not excessive in order to allow the expulsion of gases and water vapors produced due to the internal reduction of oxide during sintering. If gases remain trapped inside the parts, they could generate blistering and internal porosity that could significantly decrease the final strength by acting as preferential sites for crack nucleation and propagation.
In some cases, like frictional applications, a certain amount of porosity is desired because the liquid lubricant needs free spaces to go [7].

When the load is removed and the part is ejected from the die, a phenomenon called "springback" occurs: it is the elastic recovery that occurs in a plastically deformed part when it is released from tooling [1]. This expansion produces voids that reduce green strength, so it needs to be controlled, maintaining a compressive force on the part during the ejection from the die itself.
This springback mechanism depends on powder characteristic and on the process, in particular it increases linearly with the compacting pressure.

1.2.3. Sintering

Sintering must be performed at elevated temperature and in a protective/reducing atmosphere to avoid oxidation of susceptible metallic materials. It is a kinetic process that leads to the reduction of porosity and the densification of the material.
Sintering is a three-stage process, as can be seen in Fig. 3: at the beginning neck growth at the contact regions between particles occurs and material diffusion by surface transport leads to necking. In the second phase, grain growth starts and most of the densification takes place due to volume diffusion mechanisms, decreasing the porosity, which also changes shape from spheroidal to cylindrical. Finally, in the third stage, densification proceeds at a slower rate until residual porosity is minimized [9].

The driving force of sintering process is the reduction of free surface area and the elimination of solid/gas interface with the creation of grain boundaries.
Material transport during sintering occurs due to some mechanisms like diffusional flow, evaporation/condensation, viscous flow, plastic flow.
The most important mechanism is diffusion, which occurs though lattice volume, along a free surface or along a grain boundary and it is governed by the Fick's law [10]:

$$D = D_0 e^{-\frac{Q}{RT}} \tag{2}$$

In the equation, D is the diffusion coefficient, D_0 is a material constant, Q is the activation energy for the diffusion type (it can be in the volume, along the surface or along the grain boundary), R is the gas constant and T is the absolute temperature at which sintering process is performed. Generally, diffusion in metal is faster along grain boundaries because they are characterized by a low-order structure and a very high atomic mobility [10].

There are different sintering processes: solid-state sintering, liquid-phase sintering and pressure assisted sintering [10].

Solid-state sintering is also defined as *pressureless sintering*. The material transport is governed by surface energy and capillary forces, because density of compacted powders is increased by the filling of material in the necks at the points of contact between the particles [10].

If heat and pressure are applied simultaneously, the process is called hot-pressing or pressure-sintering and it is usually performed in case of powders which are difficult to sinter because the presence of stress allows lower temperatures [10].

Liquid-phase sintering is a process in which the mixed powders are heated above the melting temperature of the lower-melting component. The advantage of this production process includes an increased diffusion rate (thus shorter processing time), improved homogeneity of the final microstructure and reduced costs [10].
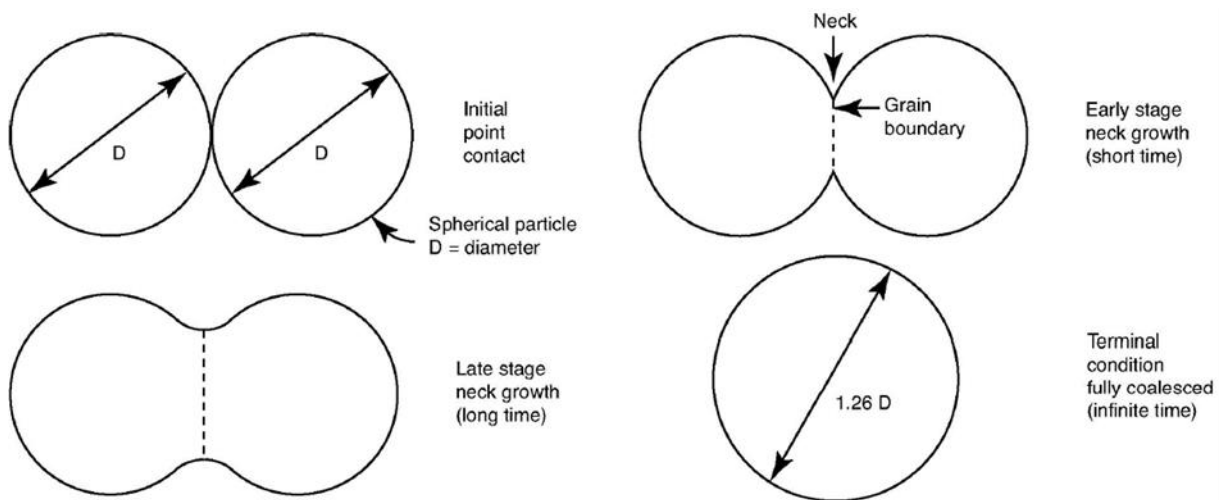
Figure 4 - Schematic representation of the sintering process, according to the two-sphere sintering model. From [9].

The main factors on which densification process depends are [1]:

- Sintering temperature: higher T promotes a rapid shrinkage and the typical range for copper is 840-900°C (the melting temperature is 1085°C).
- Sintering time: shrinkage rate decreases if the dwelling time increases, a typical range of time for copper is 12-45 minutes.
- Powder particle size: finer particles have a larger specific surface that allows a faster densification of compacts and a higher value of final density.
- Green density: higher compaction provides a higher number of contact points between particles that eases necking and diffusion.

Sintering will be further discussed in relation with binder jetting process due to the fact that it is a fundamental step of this additive manufacturing process.

1.2.4. Secondary operations

After sintering, several secondary operations can be performed in order to complete the part or improve their properties. Examples are coining and sizing through high pressure to improve the strength of the part achieving a further densification.

Other processes including machining, grinding and plating can be performed in order to obtain better dimensional accuracy, aesthetical appearance, surface finish and higher corrosion and wear resistance.

Heat treatments can improve hardness and strength of the product [7].

1.3. Additive manufacturing

Additive Manufacturing (AM), also known as Rapid Prototyping [11], is defined by the American Society of Testing and Materials (ASTM) as "the process of joining materials to make objects from 3D model data, usually layer upon layer, as opposed to subtractive manufacturing methodologies" [12].

AM techniques are becoming established approaches to realize three-dimensional objects from computer-aided design (CAD) models by adding materials layer-by-layer.

They are becoming very successful since there is the possibility to create complex shapes that are difficult to create with traditional subtractive techniques in a lower production time and with a reduced cost, in particular in biomedical sector, in particular in tissue engineering, in automotive and aerospace, where extremely good performances and properties are required [13]

AM techniques are very versatile and exploit a huge variety of materials: metals, polymers, ceramics but also organic and composite materials.

Focusing on metal powders, currently there are 29 materials which can be used for additive manufacturing processes [14].

Unfortunately, parts produced with this technology have often lower mechanical properties, so they are limited to non-structural applications, and they are not yet widespread in the industry.

The first 3D printer was commercialized in 1987 and it was based on a stereolithography process, in which thin layers of a liquid thermosetting polymer are solidified with a UV laser beam, but the first studies date back to the early 1900s when J.E. Blanther's method "cut and stack" with wax plates was invented.

In 1990 Professor David Bourell used for the first time a 3D printer to create copper-based components [15].

According to ISO/ASTM Standards [12], AM techniques can be divided into seven categories, listed in the Table 1.

Table 1 - Additive Manufacturing process categories. Adapted from standards [12].

Process categories	Technology	Materials
Vat photopolymerization	Stereolithography, Digital Light Processing	Photopolymers, ceramics
Material extrusion	Fused Deposition Modeling	Polymers
Material jetting	Polyject, Ink-jetting, Thermojet	Photopolymers, waxes, metals
Powder bed fusion	Selective Laser Sintering, Selective Laser Melting, Electron Beam Melting	Metals, polymers, ceramics
Direct energy deposition	Direct Metal Deposition, Laser Deposition, Laser Consolidation, Electron Beam Direct Melting	Metals: powders and wires
Sheet lamination	Laminated Object Manufacture	Metals, ceramics, hybrids
Binder jetting	S-Print (Sand), M-Print (Metal)	Metals, polymers, ceramics

1.3.1. Vat photopolymerization

Vat photopolymerization is an additive manufacturing process in which liquid photopolymer in a vat is selectively cured by light-activated polymerization [12].

The most known technique of this class is Stereolithography (SLA) which was developed in 1986 by Charles Hull, and it exploits a laser beam to induce polymerization, as it is represented in Fig. 4 [11].

This technique usually employs polymers, but the polymer can be charged with nanopowders of metallic materials. However, copper is a challenging material, since it is characterized by high reflectance, which causes a dissipation of the energy of the laser instead of absorbing it for the polymerization reaction.
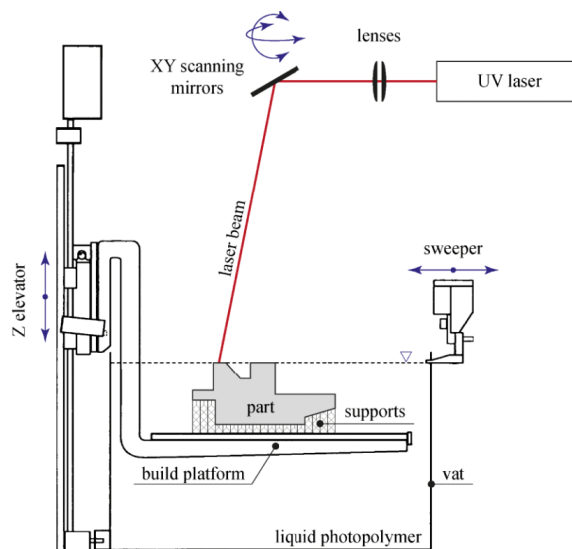
Figure 5 – Schematic representation of Stereolithography process. From [11].

1.3.2. Material extrusion

Fused Deposition Modeling (FDM) is a 3D printing process which can be classified under the category of material extrusion. It was invented by Scott Crump and patented in 1989.

This process uses a continuous filament of a thermoplastic material, which is deposited through a moving, heated extruder head.

The heater melts the filament, transforming it into thin beads that are deposited onto the substate [11].
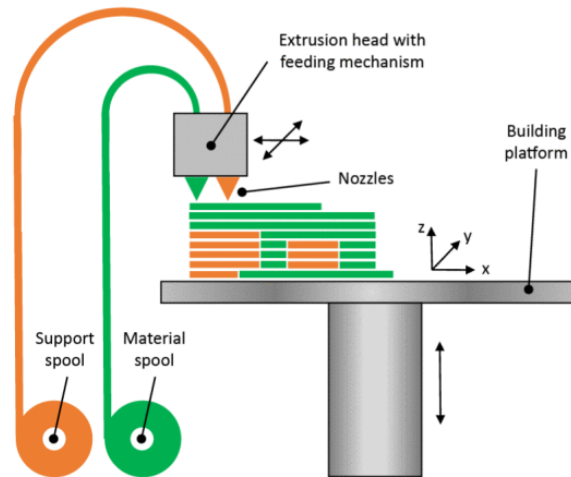
Figure 6 - Scheme of the FDM process. From [11].

This technique is not employed for pure metals as it would be troublesome to product a suitable filament at high temperatures, but there are studies involving copper powder mixed with ABS [16]. In this application, the suitable binder, mixing method and parameters as melting temperature, pressure and cooling time need to be selected properly to achieve satisfying results.

1.3.3. Material jetting

Material jetting, developed in 1984, consists in the selective deposition by a movable inkjet print head of a polymer or mixed materials, which are cured through the application of energy (UV light or heat) in order to obtain the desired geometry. Typically, the substances used in material jetting are viscous materials able to form drops [11].
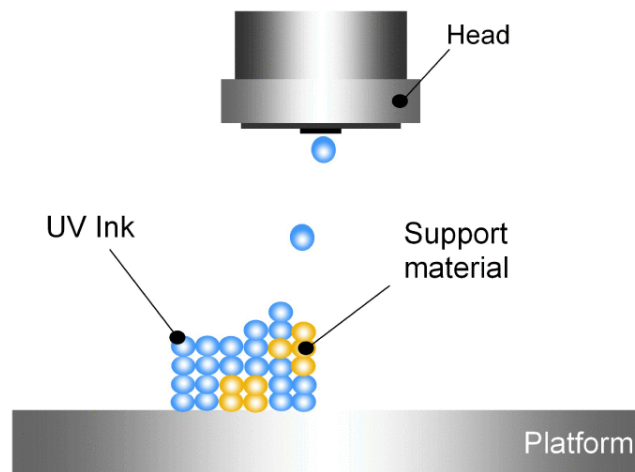
Figure 7 - Scheme of the material jetting process. From [11].

There are some examples of copper printed with material jetting, specifically by inkjet.

Li et al. [17] printed successfully an ink obtained with the dissolution of copper sulfate and sodium citrate powders in distilled water on a paper substrate to create conductive lines with a conductivity of $1.8 \cdot 10^6$ S m^{-1}, which is about 1/30 of the bulk metal.

Öhlund et al. [18] performed inkjet fabrication of highly conductive copper patterns using intense pulsed light processing (PIL) of a water-based CuO dispersion. To improve the process, the papers were treated with a porous $CaCO_3$ precoating beneath the absorption layer, which increased the range of exposure energy and decreased risk of delamination.

Jun et al. [19] prepared a copper nanoparticle ink mixing copper nanoparticles and copper complex, with an average particle size of 100 nm. They printed the copper ink on Si/SiO_2 substrates treated with different methods and conditions, obtaining stable patterns with higher conductivity compared to the untreated substate and to the ink obtained only with copper nanoparticles.

Another research [20] focused on inkjet printing of electrode on a flexible glass epoxy composite substrate using copper nanoparticle ink with a drop on demand piezoelectric dispenser. They obtained an electrode with good quality, less cracks and with a suitable value of resistivity for the desired industrial application.

1.3.4. Powder bed fusion

Powder Bed Fusion (PBF) approaches exploit the selective fusing of materials in a granular bed and are usually performed in an inert atmosphere to avoid oxygen contamination [12].

Selective Laser Sintering (SLS) uses a laser as power source to sinter the powder. A disadvantage is the presence of porosity.

Laser-based Powder Bed Fusion (L-PBF), also known as Selective Laser Melting (SLM), features a laser that, differently from SLS, melts completely the metal, therefore the produced parts exhibit mechanical properties closer to the ones of bulk materials [11].

Electron Beam Melting (EBM) is similar to SLM, but the energy source is a high-power electron beam (around 4 kW) [21].
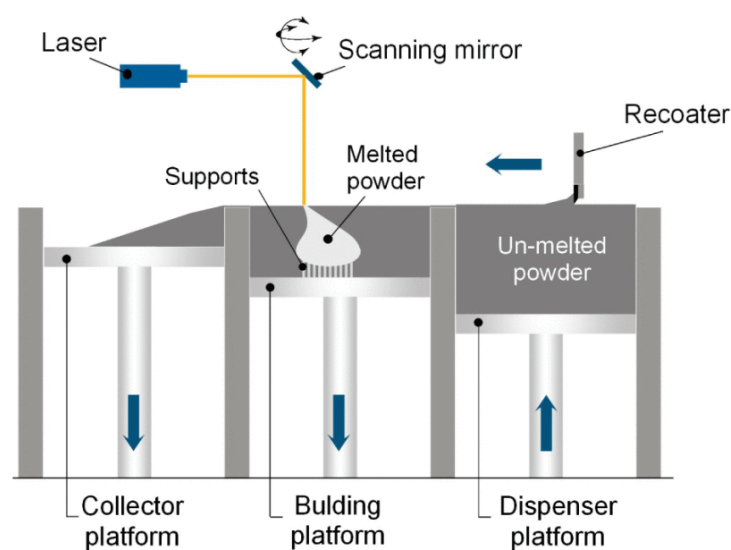
Figure 8 - Schematic representation of a SLM machine. From [11].
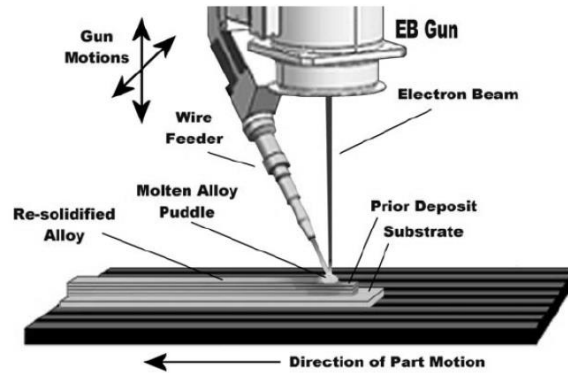
Figure 9 - Schematic representation of EBM process.
From [21].

Jadhav et al. [22] studied the printability of copper-based materials with L-PBF. A big issue in copper and copper alloys is their high optical reflectivity in the infrared region (the infrared fiber laser has a wavelength of 1080 nm) and their high thermal conductivity, which produce parts with unmolten powder particles and defects caused by lack of fusion, resulting in relative density lower than 90%.

They found out that the only way to produce copper parts with full density was the keyhole mode, which occurs when the power density of the laser beam is sufficient to cause evaporation of the metal and formation of plasma [23]. This regime allows the laser beam to reach a deeper depth compared to common situation and allows a non-linear increase in the effective laser absorption caused by multiple internal reflections inside the keyhole and subsequent absorption. In this case, 200 W was not enough to melt copper powder particles, but 300 W was sufficient to generate a keyhole mode melt pool. With these parameters, parts with near full density and good electrical, thermal and mechanical properties can be produced.

Tiberto et al. [24] investigated the impact of alloying elements on the processability of copper alloys with SLM. Under standard conditions (20 µm layers and 10-45 µm powder size), the porosity decreased from 25% of pure Cu to 5.5% of CuNi3Si. High energy densities are required to reduce porosity in the final parts. The oxygen content has a huge impact on the results, since it is detrimental for the processability of the material.

EBM of copper was researched by Guschlbauer et al. [25]. They obtained specimens with a density of 99.5% and an electrical conductivity of 58 MS/m, approximately corresponding to 100 IACS (International Annealed Copper Standard).

1.3.5. Direct energy deposition

In Direct Energy Deposition (DED) technology, a high-power source (a laser, an electron beam, an electric arc or plasma) is used to melt metal powder deposited in a sealed chamber containing inert gas.
The melt pool is then directed around a toolpath where it freezes into a solid metal.
This technology allows high deposition rates but relatively low resolution [26].
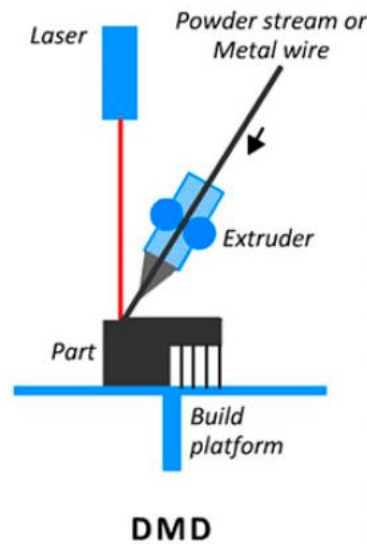
Figure 10 - Schematic illustration of DED process. From [26].

Yadav et al. [27] investigated the process of Laser Directed Energy Deposition (LDED) with pure copper. They fabricated samples with a relative density around 99.9% by increasing the laser powder. After optical analysis they found that the microstructure was mainly dominated by equiaxed grains, thanks to a lower temperature gradient across layers due to the higher thermal conductivity of copper. However, a mix of fine equiaxed grains and cellular grains is present at the bottom layers, caused by the rapid solidification due to higher temperature difference between the substrate and the deposited material.

1.3.6. Sheet lamination

In Laminated Object Manufacturing (LOM), layers of adhesive-coated laminates (plastic or metal) are glued together and cut in order to obtain the desired shape [12].

Some advantages of this technique are the low cost, the easiness and the possibility to obtain large parts but post processing can be necessary to obtain the desired surface finishing [28].
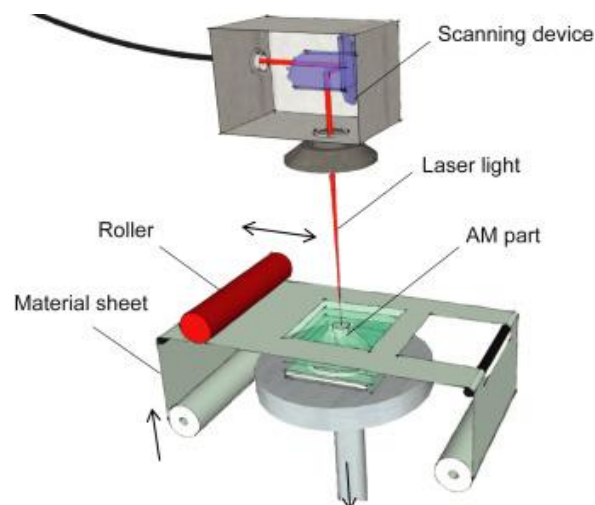
Figure 11 - Schematic representation of LOM process. From [28].

1.4. Binder Jetting of copper

Binder Jetting was formerly known as three-dimensional printing (3DP) and was developed at Massachusetts Institute of Technology in 1993 by Emanuel Sachs, who used a gypsum-type powder with a glycerin/water binder deposited via thermal bubble inkjet printheads [29]. Then, ExOne launched in 1998 the first commercial 3D printer for metals, the RTS-300.

BJ process is composed of four steps: *printing*, *curing*, *depowdering* and *sintering* [30].

First of all, the 3D CAD files are sliced by a software to 2D files with a chosen layer thickness. After that, the printing process can start: the powder is deposited on the work plane from a hopper and then spread with a roller characterized by a given rotational and translational speed. Then, an inkjet print head moves along the X and Y directions, depositing selectively droplets of a liquid binding material, the *"binder"*, which interacts by capillarity with powder particles, forming a primitive shape. After the deposition of the binder, an electrical heater passes over the powder bed to dry the layer and maintain a uniform temperature across the thickness.
The process is done one layer at a time, so the piston lowers along the Z direction in order to obtain stacked layers that are attached by the binder. This infiltrates into the powder through the voids between the particles and sticks together the particles within a layer and to the layer beneath [30]. The part formed with this process is called *"green"* [31].
In the following figures, the scheme of the BJ process is shown.
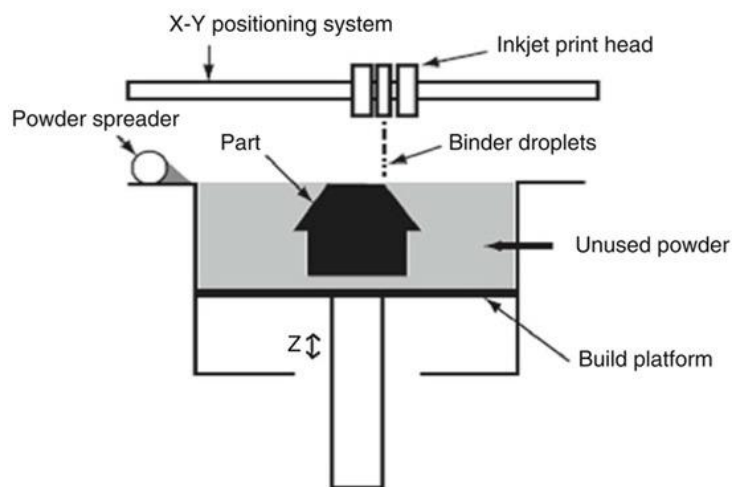
Figure 12 - Schematic illustration of the binder jetting printer components. From [30].
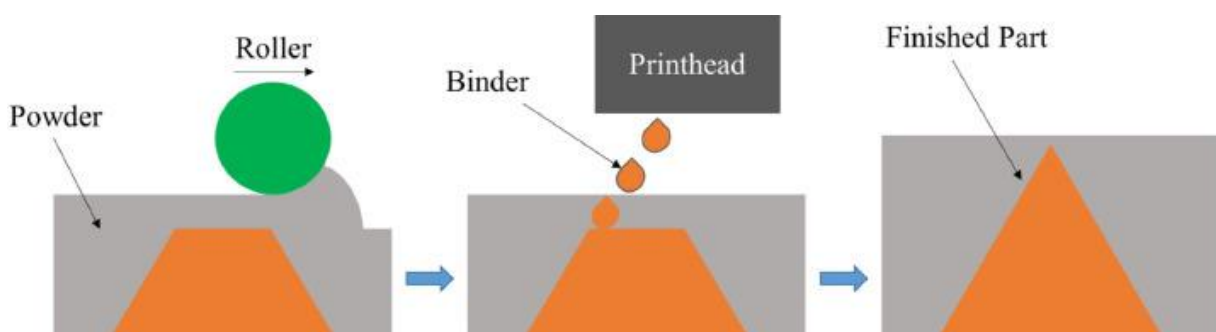
Figure 13 - Schematic diagram of the binder jetting process. From [36].

At the end of the printing process, the green part is heated at moderate temperature to cure the polymeric binder, in order to obtain an object with a sufficient strength for cleaning and handling [32].

After that, excess powder is removed by a soft brush or pressurized air in a process called *"depowdering"* or *"de-caking"* and can be reused in some cases [33] [30].

Then, a debinding process, either thermal or chemical, is performed to eliminate the binder from the part [12].

The final step is the sintering process with the aim of obtaining the desired density and strength; during sintering particles are fused together through atomic diffusion, and dimensional shrinkage occurs, affecting the dimensional accuracy and part quality. Pores are features that promote crack propagation due to stress concentration, so the reduction of porosity is normally related to an improvement of the mechanical properties [30].
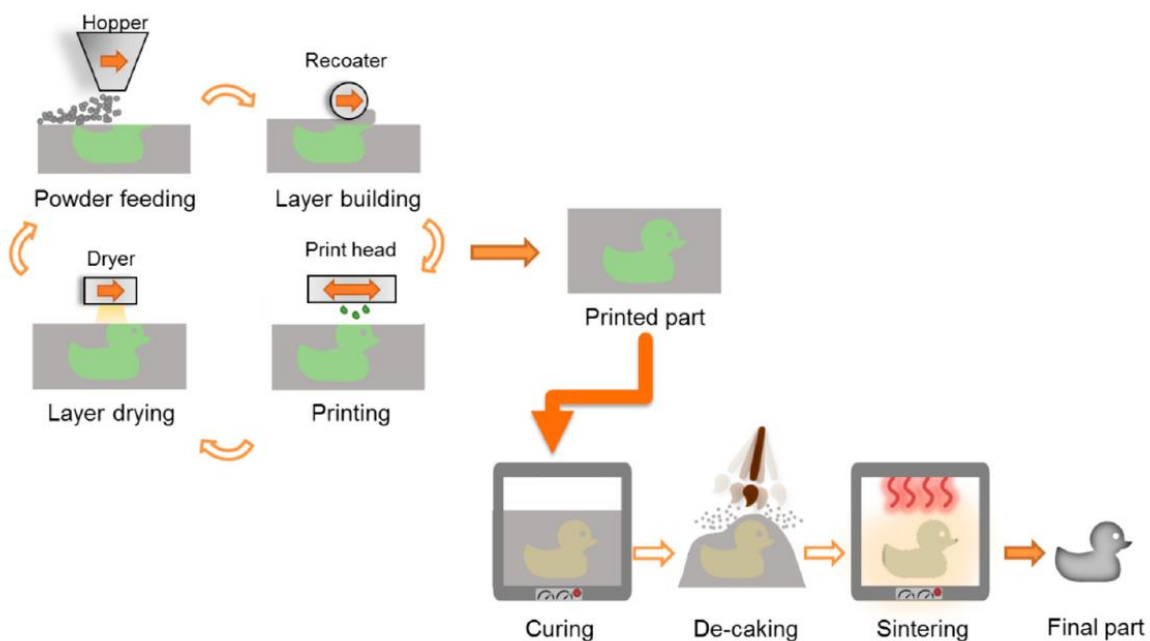
Figure 14 - General scheme of the binder jetting fabrication process. From [33].

Binder jetting is one of the most interesting techniques because it is versatile and suitable for a wide range of materials, including metals, polymers and ceramics [34].

Due to the fact that lasers are not involved, materials with high reflectivity and high thermal conductivity can be printed, as in the case copper. For the same reason, as BJ is not fusion-based, residual stresses are almost absent as opposed to high energy beam-based additive manufacturing techniques [35].

Another advantage of binder jetting is the fact that it is relatively cheap since it does not require vacuum, high temperature or power. Unbounded powders can be reused and recycled, thus reducing costs and material consumption.

Furthermore, the use of a powder bed eliminates the need for support structures in case of printing of overhanging features [34].

In addition, this technology is known for high volumetric output because several nozzles can be employed simultaneously and reduced time for printing of complex geometries.

Even though there are many advantages in performing this technology, like the creation of complex structures and the ease of the process, the final parts can be characterized by low density and therefore poor mechanical properties compared to traditionally manufactured components.

Copper is a challenging material to process with energy-based additive manufacturing techniques because it is characterized by high thermal conductivity and high optical reflectivity, thus binder jetting may be an interesting technique to manufacture copper parts [36].

1.4.1. Powders

Powders for binder jetting additive manufacturing should be characterized by specific properties. The most important features studied in binder jetting are [29]:
- shape/morphology,
- mean size (d_{50}) and particle size distribution (PSD),
- flowability and spreadability,
- packing density,
- bulk and surface composition.

The major challenge in BJ is the elimination of porosity, in particular in applications where good electrical properties are required. Frequently, hot isostatic pressing is performed to improve the density but it is not desirable because it requires time and it is expensive, so it is convenient to improve densification by other means, as PSD [37].

PSD is a key parameter in AM since it affects flowability, packing behavior and deposition of the powder and determines process parameters like layer thickness and binder saturation [29].

Previous studies showed how the use of fine particles, with a diameter lower than 5 μm, is beneficial to BJ because the surface of printed parts is smoother, the dimensional accuracy is improved and the sintering process is promoted, since one of the driving forces for densification is the specific surface area [38].
Unfortunately, fine particles tend to agglomerate due to strong particles interactions (van der Waals, electrostatic forces and humidity-induced capillarity), reducing spreadability and flowability, causing the creation of voids that can slow the penetration of the binder, resulting in a lower printing resolution [33].
Large particles (dimension higher than 50 μm) are characterized by better spreadability and packing but the total surface area is low, leading to reduced densification, thus high porosity and low density of sintered parts [30].
For all these reasons, mixing powder with different size is favorable to increase powder packing and green density [32].
In bimodal powder mixing, both small and large particles are present, with small particles fitting in the interstitial voids between the large ones [39].
Bimodal powder mixtures have many advantages like increased green density and strength, which lead to better mechanical properties, reduced shrinkage after sintering, and layer density increased by 15%, preventing balling phenomenon and achieving higher radiative flux.

Miyanaji et al. [38] studied binder jetting additive manufacturing of fine copper powders with average particle size of 5 μm and compared the results to previous literature on BJ of coarse copper powder, with sizes of 20 μm and above.

They concluded that fine powder improved the sintered density by 9% with respect to the coarse copper powder and also the ultimate tensile strength of the parts increased by 119 %, 55 % and 24 % compared to those printed with copper powder with d_{50} of 25 μm, 17 μm and bimodal powder (30 + 5 μm) respectively. Additionally, fine copper powders resulted in parts with smaller grain size and greater mechanical properties due to the higher density of grain boundaries, which increased resistance to dislocation movements under tensile stress.

Another important powder parameter is the morphology because it strongly influences the powder packability and flow behavior.

Spherical particles feature low internal friction, good flowability and better sinterability since their packing is more efficient [32] [34].

In powder metallurgy, usually water atomized particles are used, but they tend to have a more irregular shape, which is responsible for scarce flowability due to higher interparticle friction and poor self-compacting capability [33].

Consequently, gas atomized powders are preferred in BJ [30].
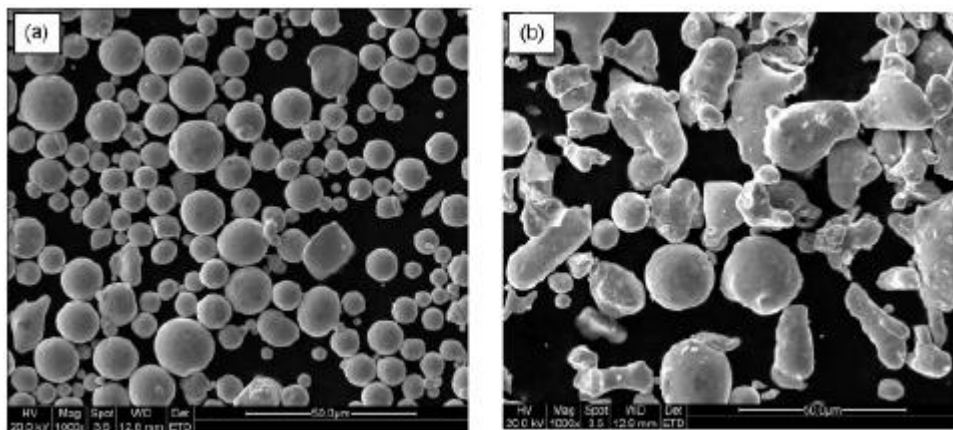
Figure 15 - SEM images of characteristic morphologies of 316L SS powder; (a) gas atomized powder; (b) water atomized powder. From [30].

Powder morphology and PSD affect the pore size distribution, which determines the binder penetration. If the powder bed is distributed in a heterogeneous way, for example in case of irregular particles produced by water atomization, the binder needs more time to penetrate completely and will leave macro-voids empty since they feature a low capillary pressure. In case of homogeneous powder bed, like those obtained by gas atomized particles, the binder infiltration is favored [29].
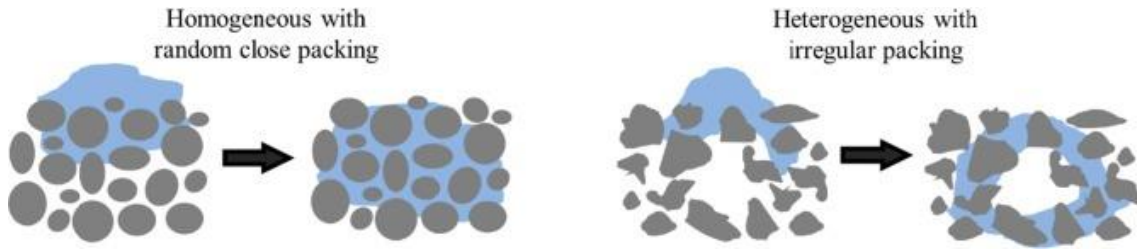
Figure 16 - Schematic illustrating binder penetration within (left) homogeneously and (right) homogeneously distributed powder bed. From [29].

Powder packing density is another important parameter which represent the relative density of each deposited layer and determine the arrangement and the contact point of the particles. It is a function of powder size distribution; in fact, a broad PSD provides higher packing density [29].

Powder flow is the ability of a powder to move over itself when being transferred through a process. High flowability leads to better printing resolution, dimensional accuracy and green density. Powder shape and morphology influence flowability: regular and spherical particles provide a better flowability. Actually, this parameter depends also on surface roughness and composition of particles and density of the bulk material [29].

1.4.2. Binder

The binder is a temporary glue to join powder particles into the desired shape and holding particles in that shape until initial state of sintering [30].
The selection of the binder material is very important because it determines the mechanical properties of the green part [40].
The criteria for the selection of a binder are mainly five [41]:

- Good interaction with powder, in particular wettability and capillarity.
- Binder residue in post processing, in fact all cured binder should evaporate during debinding process because the residues will turn form carbides and oxides or will diffuse due to high sintering temperature and lead to carburizing.
- Low viscosity, because the binder needs to not solidify in order to allow the formation of individual droplet beads and their break off from nozzles.
- Long shelf life, so the binder must have adequate chemical stability.
- Acceptable environmental risk.

In inkjet printing, the Ohnesorge number (Oh) can be calculated to determine if a binder is appropriate for the application [40]:

$$Oh = \frac{\sqrt{We}}{Re} = \frac{\mu}{\sqrt{\rho \gamma D}} \tag{3}$$

The Ohnesorge number is a dimensionless function of binder viscosity (μ), density (ρ), surface tension (γ) and nozzle diameter (D) and can be expressed with Weber number (We) and Reynolds number (Re). If the inverse of the Ohnesorge number of a binder has a value between 1 and 10, it can be successfully employed in commercial BJ printers [42] .
If 1/Oh is less than 1, viscous forces are predominant and the ejection pression is too high; if this value is greater than 10, the nozzle ejects a continuous column and this could lead to the formation

of satellite drops behind the main drop.

The formed drop needs to have enough energy for ejection, so the minimum Weber number should be at least 4 to overcome the barrier given by the effect of fluid/air surface tension at the printhead of the nozzle. An upper limit also exists: Weber number should be lower than 50 to avoid splashing phenomenon of the binder, which may lead to higher surface roughness of the part [29].
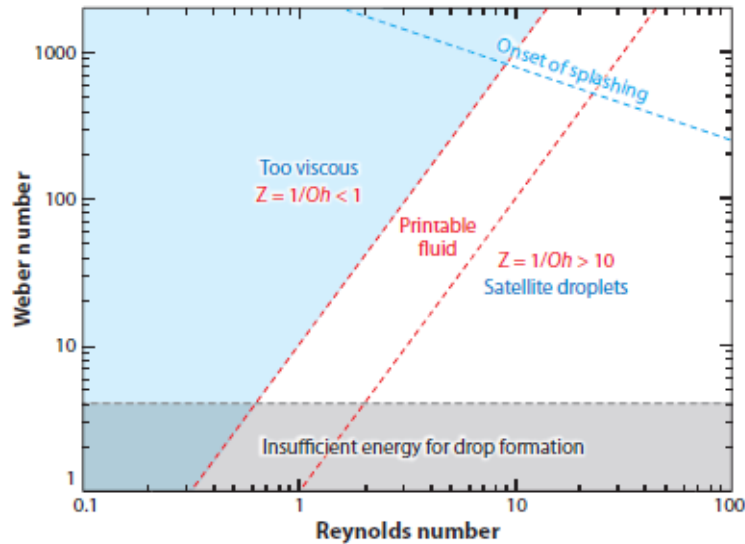
Figure 17 - Range in which the printing process is stable plotted in a coordinate system defined by Reynolds and Weber numbers. From [42].

Typically, organic liquid binders are used but they can adversely affect the final performance. First of all, the debinding operation requires a refined sintering profile and slow heating ramp to facilitate pyrolysis and degassing and this could lead to structural defect. Additionally, structural integrity of green part can be altered, especially if the onset sintering temperature is higher than the binder burn-out temperature and also pyrolysis of binder could leave residual carbon content which affects purity and, therefore, mechanical, thermal and electrical properties of the final part [40].

To overcome these setbacks, innovative binder materials have been investigated for the production of binder jetted copper parts.

Miyanaji et al. [38] investigated the effect of binder type on part quality, employing two types of standard ExOne polymeric binders, the aqueous-based and the solvent-based. The use of solvent-based binder leads to a higher sintered density by 6% compared to the aqueous-based one, because the last one contains more oxygen which reacts with hydrogen, forming water vapor molecules, that are difficult to be removed from copper microstructure, thus hindering densification. Moreover, the parts printed with solvent-based binder showed slightly more shrinkage in lateral directions (X and Y directions), due to larger densification of specimens. The green density is not affected by the binder type.

Bai and Williams [43] studied the possibility of using two different nanoparticle binders in BJ of pure copper: a colloidal organic binder, prepared by suspending nanoparticles in an already existing solvent-based organic binder, and an inorganic nanosuspension in non-adhesive dispersion medium. The nanoparticle binder produces green parts with higher density but there were no substantial

differences in sintered parts density with respect to parts printed with regular organic binders due to a reduced sintering densification. Also, the nanoparticles improved the tensile strength of sintered parts as a result of reduced grain size, because the grain boundary mobility is constrained by the presence of nanoparticles.

The nanoparticle suspension is able to produce stronger green parts compared to the commonly used organic binders because an early sintering is performed during printing, using a higher powder bed temperature (250-260 °C) and an additional post-print curing allows further nanoparticle sintering. The actual sintering is done at lower temperatures compared to the usual processes because copper nanoparticles can form necking in the range between 150 and 300 °C. The exploitation of nanosuspension guarantees an improved purity of printed parts, ideal for conductive applications, but it is limited by the complexity of dispersing particles and by the possible ink sedimentation and printhead nozzle clogging during printing.
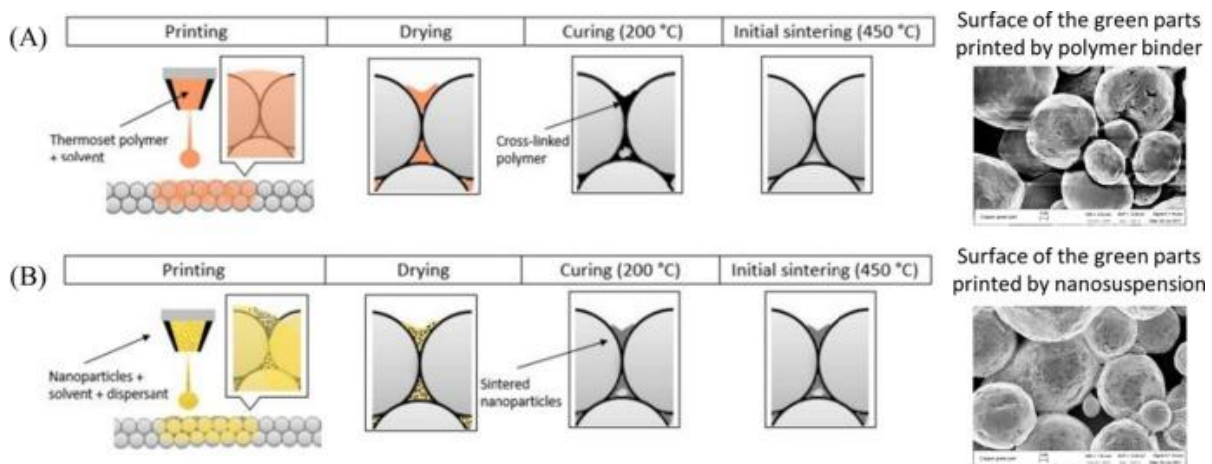
Figure 18 - Schematic showing the use of (A) a thermoset polymer or (B) a nanoparticles suspension as binder. From [29] and [40].

The same authors of the previous article examined a metal-organic-decomposition (MOD) ink as a precursor [40]. MOD ink contains an organometallic compound formed by ligands and metal salts. Complexing agents can control the precipitated particle size and improve solubility of metal-organic compounds in solvents. Since the MOD ink is particle-free, concerns like ink sedimentation, printhead nozzle clogging and particle oxidation are reduced. Unfortunately, even if the sintered copper parts printed by copper MOD ink are characterized by a dense core section with less porosity than polymer binder parts, a formation of a porous outer shell composed of large pores around the dense core leads to an overall lower sintered density compared to the traditional parts fabricated with polymeric binders. This dense core is produced by the powder loss caused by the weak powder bonding at surface in MOD ink printed parts.

There are two different mechanisms employed in BJ processes: continuous-jet (CJ) and drop-on-demand (DOD) [30].

In CJ systems, a pressurized steam of binder is ejected through small nozzles to form liquid jets. Then nozzle is held at a potential relative to ground and each drop is provided a small charge, then, individual drops in the stream are steered by an applied potential to deflector plates. This method produces a continuous stream of liquid drops, even when it is not required, hence unwanted drops

are deflected by the electric field to a gutter and unused ink can be recycled. CJ system is more advantageous for high-speed coverage of large areas and it is not largely used [42].

In DOD technology, drops are generated only when they are needed by the propagation of a pressure pulse in the fluid. The pressure pulse can be generated with two methods. In thermal DOD printing a small thin-film heater in the fluid chamber heats the fluid above its boiling temperature to produce a small vapor bubble, which collapses after the removal of the current, generating the pressure pulse. In piezoelectric DOD printing, a piezoelectric transducer generates mechanically a pressure wave on the binder reservoir [42].

DOD systems are employed for the deposition of small and controlled amount of binder, in particular piezoelectric printheads are more reliable than thermal ones [30].
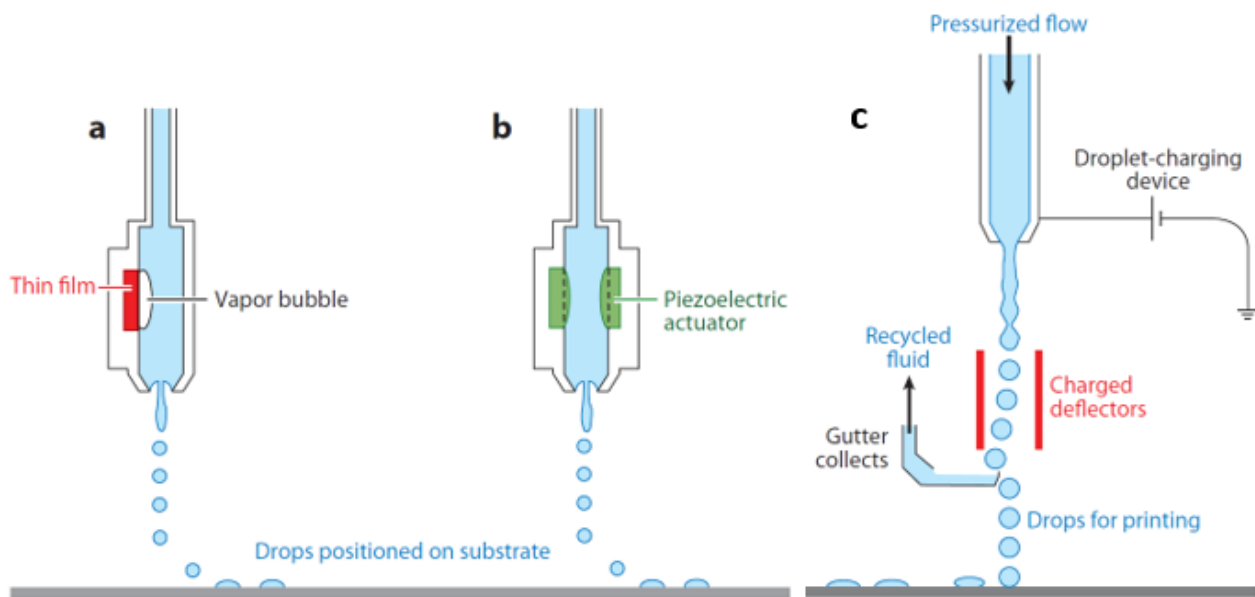
Figure 19 - Schematic diagram showing the principles of inkjet printing system. In DOD, the pressure pulse is generated by (a) a vapor pocket or bubble generated by a thin-film heater (thermal inkjet) or (b) a mechanical actuation, like from a piezoelectric transducer (piezoelectric inkjet). (c) represents a CJ printer. Adapted from [42].

1.4.3. Binder-powder interaction

Binder-powder interaction needs to be studied and understood in order to select the suitable parameter, since it can significantly influence the geometry accuracy, the green part strength and the final surface roughness [29].

After a droplet with the size of few micrometers is jetted through the printhead, the binder wets the surface and spreads in a time range less than 100 µs, assisted by the kinetic energy of the droplet. As soon as the binder is in contact with powder, the pores act as capillary tube and absorb the liquid, forming an initial nucleus with the total pore space filled with binder (100% saturation ratio). This nucleus is surrounded by dry loose powder with zero saturation, so the binder is drained from saturated regions to unsaturated ones and the initial nucleus grows until equilibrium is reached. The saturation ratio of the nucleus at this state is defined *equilibrium binder saturation ratio* [44]. In the following figure, the process of formation of a primitive is represented.
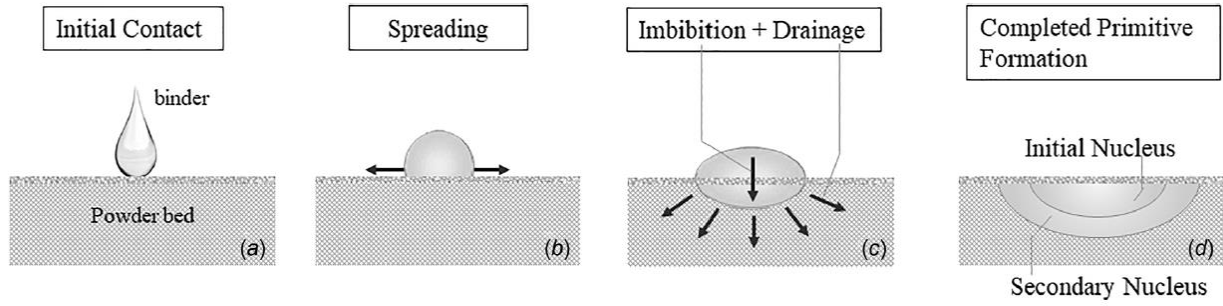
Figure 20 - Schematic of binder-powder interaction and primitive formation in binder jetting. From [44].

Equilibrium binder saturation ratio can be calculated as the ratio of binder drop volume (V_{binder}) to the pore volume of binder-powder granules [44]:

$$S_e = \frac{V_{binder}}{V_{granule}\,(1 - \varphi_{powder})}$$

(4)

In the equation, φ is the powder packing density and $V_{granule}$ is the volume of a binder-powder granule.

The main driving force behind binder penetration is capillary pressure. A fluid in a small capillary tube tends to rise to wet the walls of the tube, driven by capillary pressure (P_{cap}), which depends on interfacial surface tension (γ_{LV}), dynamic contact angle (θ_d) and capillary radius (r) [44]:

$$P_{cap} = \frac{2\gamma_{LV}\cos\theta_d}{r}$$

(5)

Therefore, liquid penetration into the powder pores depends on surface tension, contact angle and pore radius. Also, the powder packing should be considered, due to the fact that in case of irregular packing there are large macro voids which do not contribute to effective surface area and they do not participate in liquid flow, leading to an overestimation of the optimal binder saturation [45].
It is necessary to make one distinction: the dynamic contact angle (θ_d) is the wetting angle when the binder drop penetrates the capillary pores between two powder particles, on the other hand, the apparent contact angle (θ_a) is the angle between the binder drop and the apparent solid surface of the powder bed [44].
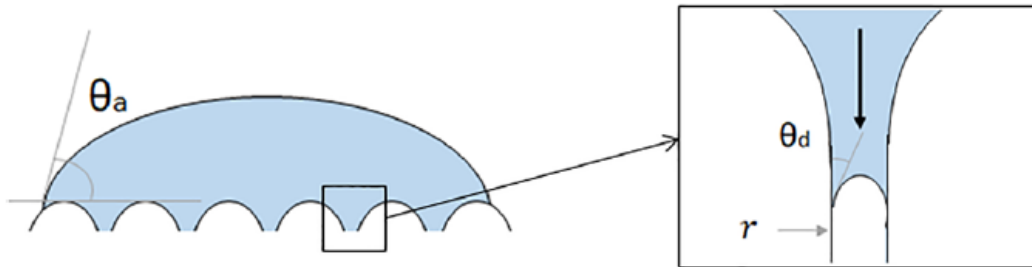
Figure 21 - Apparent contact angle of binder spreading on powder bed (ϑ_a) and dynamic wetting contact angle in the powder capillary pores (ϑ_d). From [44].

When binder droplets impact on the powder bed, different granule formation mechanisms can occur. In case of fine, cohesive powders, tunneling occurs: the binder drop pulls in aggregates from all sides, forming spherical granules with some protuberances due to incomplete penetration. Spreading phenomenon occurs if the powder bed is composed of dense, coarse and free-flowing particles and the binder droplet has low velocity and leads to the formation of flat disks granules. On the other hand, when a high velocity binder drop impacts on a dense powder bed with coarse particles, craters are formed. In addition, high droplet velocity affects binder saturation: when velocity increased from 3 m/s to 9 m/s, binder saturation decreased from 73 to 48% [29]. If the velocity of the droplet is too high, particles can be ejected due to the impact, causing a potential increase of porosity in the part [33].
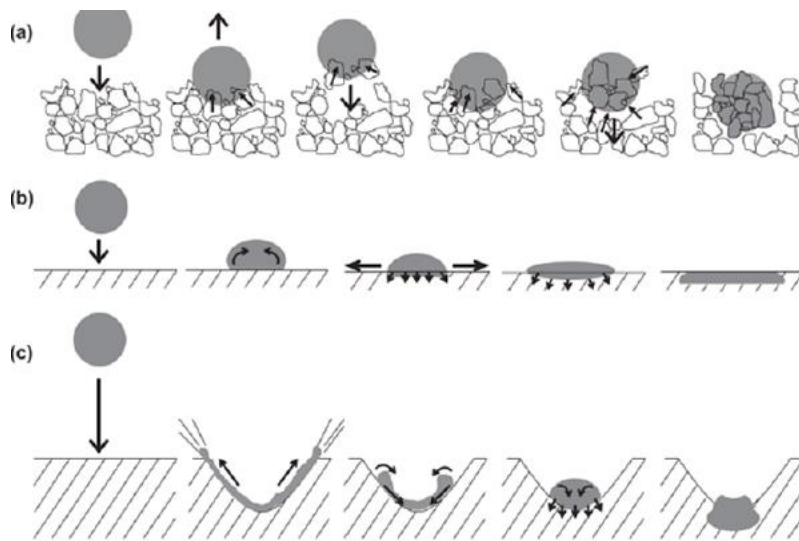
Figure 22 - Schematic of the three granule formation mechanisms:
(a) tunneling; (b) spreading and (c) crater formation. From [29].

It was found that for fine particles (<10 μm), consecutive binder droplets coalesce and form large agglomerates on powder bed surface. This phenomenon is called balling due to the formation of these balls with a liquid core surrounded by powder shell, which can be dried and form hollow granulates, responsible of a reduction of surface energy and generation of defects. To overcome this defect, binder characteristics like surface tension, viscosity and powder distribution and shape need to altered and corrected.

Another frequent printing problem is splashing, in which binder droplets disintegrates into smaller satellite droplets [41].

1.4.4. Process parameters

The quality of the produced parts is significantly influenced by process parameters and properties of building material [46].

In literature many articles that research the best parameters of BJ can be found.
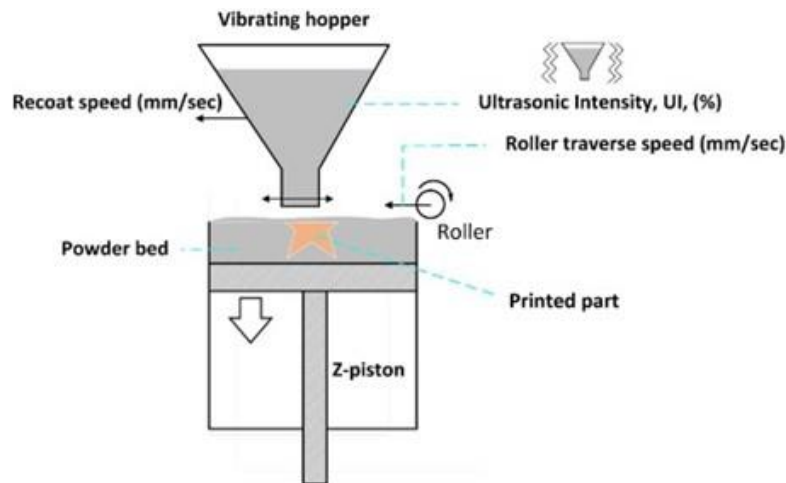
*Figure 23 - Schematic of the powder recoating mechanism in Innovent
ExOne printer and the main printing parameters. From [38].*

1.4.4.1. Layer thickness

Layer thickness is the distance by which the building plate is lowered after printing a layer and it is a very important parameter because it constrains the resolution of the printed part [30].

If the layer is thinner, the printed part is characterized by good final properties, better surface and part quality and geometrical accuracy but the process time is significantly increased [46] [47].

In case of fine particles, Miyanaji et al. [38] suggest that a lower value of layer thickness if better because it facilitates penetration of droplets, improving binding across layers and reducing inter-layer binding defect and porosities.

If the layer thickness is larger, the process time is reduced but the binder has not sufficient time to penetrate in vertical direction, leading to the formation of defects [30]. Also, increasing layer thickness might lead to a reduced powder bed density.

The minimum layer thickness should be at least thicker than the largest particle and the optimal one is approximately three times the maximum particle size to give a sufficient space for powder arrangement. [32] Usually, the suggested value of layer thickness is 50 μm [46].
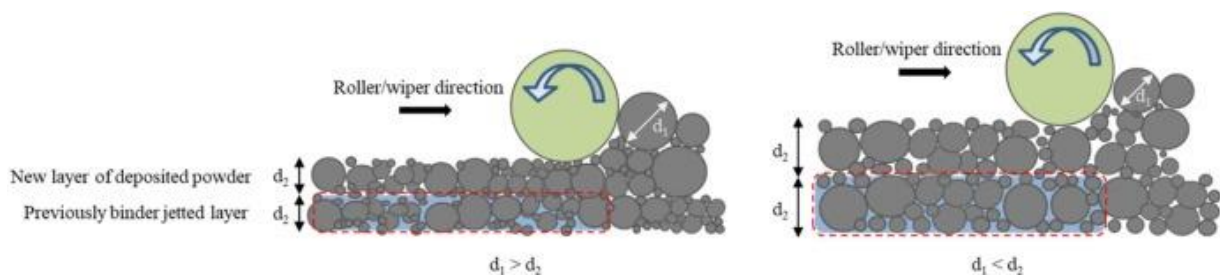
*Figure 24 - Comparison between different powder particle size and different layer thicknesses
affecting powder bed density and dimensional resolution. From [29].*

The reason why the layer thickness influences so much the surface finish of the part is given by the *"stair-stepping"* phenomenon, originally proposed by Onuh and Hon in 1998 for SLA. The BJ machine slices the part into a series of horizontal cross-sections with the height of one layer thickness. If the value of layer thickness is too high, the geometry of the surface is not exactly replicated, resulting in a poor surface quality [46].
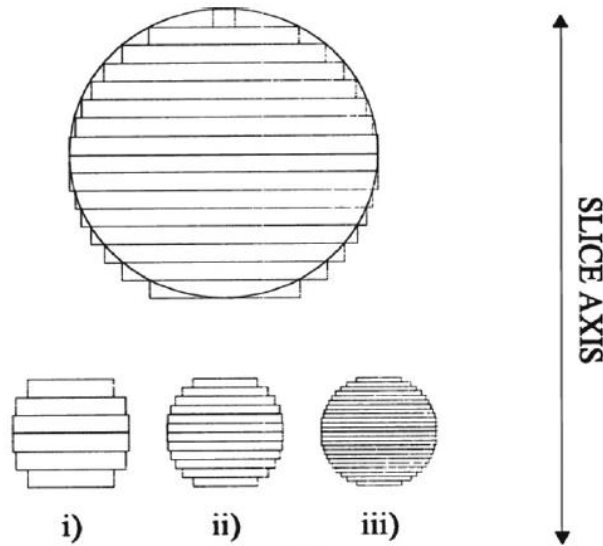
Figure 25 - Illustration of "stair-stepping" phenomenon which affects surface roughness. From [46].

1.4.4.2. Binder saturation

Binder saturation is the percentage of air volume occupied by binder [30].

$$S = \frac{V_{binder}}{V_{air}} = \frac{V_{binder}}{(1 - PR) \cdot V_{solid}} \tag{6}$$

In the equation PR is the packing rate, which is the fraction of volume of powder in a given volume of powder and air, defined as [30]:

$$PR = \frac{V_{powder}}{V_{powder} + V_{air}} \tag{7}$$

Binder saturation depends on the printhead drop-on-demand system capacity and affect surface quality, dimensional and geometric accuracy. It also has a significant influence on green density and strength, so part handling capacity, and mechanical properties of the final sintered part [14].
To evaluate the optimal saturation, Miyanaji and Yang [48] [49] studied the equilibrium saturation, the value at which the liquid binder stops to migrate due to balance between capillary pressure of saturated and unsaturated regions. They predicted well the result compared to the experimental one and confirmed the fact that binder-powder interaction in the powder bed is driven by the capillary pressure over the interfaces of binder and air.

Low values of binder saturation cause inadequate bonding between layers or within a layer, leading to the formation of pores, responsible for the reduction of mechanical properties. Additionally, in case of undersaturation, particles detach from the part and delamination can occur.
In case of too high values of binder saturation, a phenomenon called bleeding may occur: the binder can migrate to outside the defined area and bond an excessive amount of powder, affecting the geometry and the surface of the part. Oversaturation leads also to a lower volume fraction of powder and creates more pores after debinding process; for this reason, the neck formation during

sintering is hindered and the final density is lower [32]. Higher saturation, in addition, consumes more electrical power and time during printing [46].
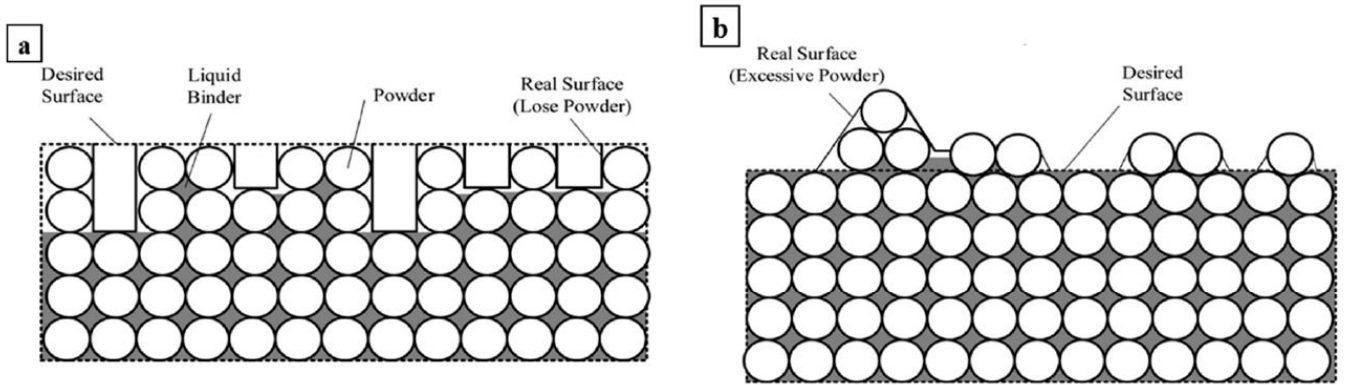
Figure 26 - Schematic of binder saturation effect on surface roughness: (a) low binder saturation leads to lack of binding and powder loss; (b) high binder saturation leads to excessive powder bond. From [30] and [46].

1.4.4.3. Heating power ratio

After printing of each layer, the bed moves under an electrical infrared heater to dry the binder. The heater power ratio is defined as [46]:

$$R_{ph} = \frac{P_c}{P_m} \cdot 100 \tag{8}$$

In the equation, P_c represents the current heater power and P_m is the maximum heater power. This ratio describes the power consumption of the heater and it is expressed as a percentage.
This parameter is essential, since it controls the drying time of liquid binder and consequently deformation, shrinkage, surface characteristics and dimensional accuracy of the green part [29].
If power ratio is too low, the binder will not be dried enough and the part will not be solidified.
On the other hand, a too high power ratio will lead to higher deformation and shrinkage during printing process due to early curing and will consume more electrical power [30] [33].

1.4.4.4. Drying time

Drying time is the time taken by the print bed under the heater to be dried after each layer printing.
During drying, the printhead moves into the cleaning reservoir to remove excessive binder and to prevent blockage [46].
Drying time depends on the binder saturation, binder composition and chemistry, layer thickness, wettability of powder with binder and powder bed characteristics [29].
Excessive drying time results in wasted time, higher electrical power consumption and solidification of the binder, which leads to weak bonds between layers and a consequent fragility, cracking of the powder bed and not sufficient dimensional accuracy of the part.
A too short drying time does not allow the complete cleaning of printhead and cause a blockage of nozzles. In addition, if the drying time is not sufficient to allow a complete penetration of binder into the whole part, leaving several pores. In sintering process, higher porosity means higher shrinkage, in particular in Z and Y directions [33].
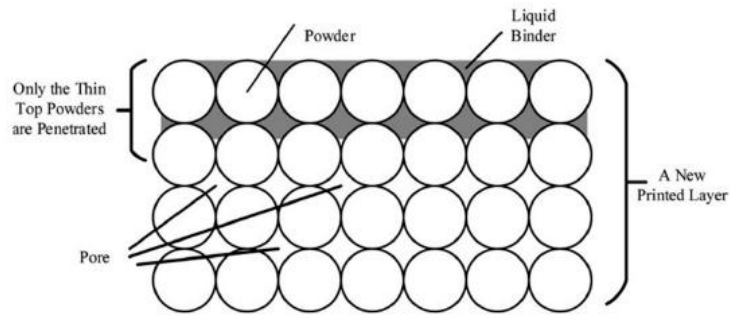
Figure 27 - Schematic showing that short drying times causes inadequate binder penetration. From [30] and [46].

1.4.4.5. Roller motion

In binder jetting, a roller moves over the print bed after the deposition of powder to level and spread uniformly the particles. It is characterized by two directions of motion: rotation and transverse. The first one is the rotational speed of the roller and the second one is the speed at which the roller moves across the bed while rotating.

Usually, a higher spreading speed results in lower powder uniformity and packing density, meanwhile a lower speed increases the printing time [33].

In case of coarse powder particles, roller transverse speed of 5-6 mm/s is recommended to obtain uniform and smooth layers. Actually, a lower speed is better, but the printing time would be too high [29].

Miyanaji et al. [38] analyzed the effect of variation of roller transverse speed on green part density in case of fine powder. They kept the ultrasonic intensity fixed at 75% while changing the roller transverse speed from 5 mm/s to 110 mm/s and noticed how the green density increased from 42.2% to 45.3%, with the exception of 10 mm/s and 80 mm/s. These results suggested that, for fine particles, higher green part density can be obtained with higher roller transverse speed due to the compaction generated by cohesive forces between particles and the shear stress imposed by the higher speed.
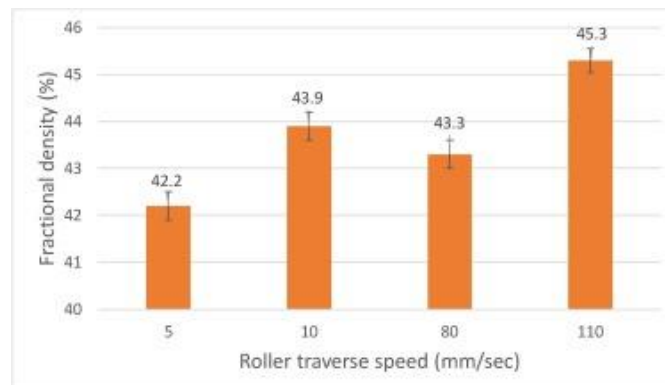
Figure 28 - Effect of the roller transverse speed (mm/s) on green part density (%). From [38].

1.4.4.6. Recoating speed

The recoating speed is a parameter used to specify the rate at which the hopper moves across the powder bed and distributes the powder.

Recoating speed should be coordinated with roller motion in order to produce parts with adequate properties in an acceptable time.

Fine particles tend to agglomerate due to the moisture absorption and consequently clogging of hopper dispensing gate can occur, decreasing the powder dispensability, which is the amount of powder materials dispensed from the hopper. This phenomenon can alter and can interrupt the printing process. To reduce the effect of moisture absorption, the feedstock can be pre-dried in a curing oven before the printing process or the hopper can be kept at a moderate temperature during printing with silicon heating pads attached to the hopper [38].

1.4.4.7. Ultrasonic intensity

The ultrasonic intensity is the intensity with which the ultrasonic vibrator operates to distribute powder.

Miyanaji et al. [38] studied the effect of the variation of ultrasonic intensity on the green part density. They varied this parameter between 25% and 75%, keeping the roller transverse speed constant at 5 mm/s, and observed that higher ultrasonic intensity resulted in a higher amount of deposited powder, which leads to higher green part density. In fact, the green density increased from 41.13% with 25% of ultrasonic intensity to 42.93% with 75% of ultrasonic intensity. The only exception is the case in which the hopper is not heated, since, even if U.I. is high, the green density in significantly lower.
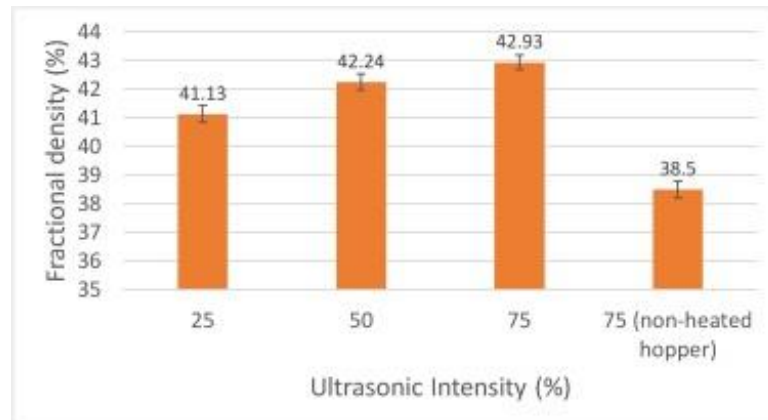
Figure 29 - Effect of ultrasonic intensity (%) on green part density (%). From [38].

1.4.4.8. Printing speed

The printing speed is the forward travel rate of printhead in Y direction.

Miyanaji et al. [50] showed how increasing the printing speed reduced the accuracy of the fabricated parts. This dependency is due to the velocity of the binder droplets jetted from the printhead. The dimensionless Weber number is commonly used in fluid mechanics to describe the interaction between a fluid and a solid and it can be defined in Eq. 9 as the ration between the deforming inertial forces to stabilizing surface tension force.

$$We = \frac{\rho r v^2}{\gamma} \qquad (9)$$

In the equation, ρ is the density of the binder, r is the radius of the droplet, v is the velocity of the droplet and γ is the surface tension of the binder.

Then the Weber number is low, the behavior of the binder is dominated by the surface energy, so the droplet suffers a small deformation, while a high value of this number means that the velocity is higher, so the liquid can wet a larger area. Despite this advantage, splashing might occur if the velocity of the droplets exceeds a certain threshold, which depends on the properties of the fluid and the powder bed. Splashing phenomenon occurs due to the oblique impact of the droplet because, as shown in the figure, the overall velocity of the droplet can be decomposed into horizontal and vertical components: the horizontal component of the drop velocity is the printing speed and the vertical one is the droplet release speed. If droplet release speed is maintained constant and printing speed is increased, the horizontal component is more prominent and splashing occurs, causing a loss of dimensional accuracy and also the strength of printed parts because the saturation level is affected due to dimensional change of specimens.
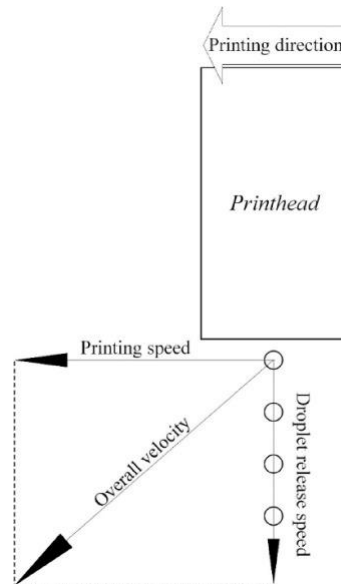
Figure 30 - Schematic graph of a droplet release from the printhead. From [50].

1.4.5. Post-processing

After the printing process, the parts need to go through some treatments to achieve the desired properties.

1.4.5.1. Curing and depowdering

Curing treatment is done immediately after the printing process to increase the binding strength between binder and powder by cross-link and polymerization of the binder [29].

Polymerization of binder can be done with visible light, heat or pressure, but the most common one is thermal curing: specimens are placed in an oven at a certain temperature for a specific time [30]. After the curing, the green parts should possess enough strength and structural integrity to be handled without risk of breaking. Then, depowdering process is done: all the excess and unbounded powder is meticulously removed. Particles can be removed with brushes, pressed air, vibration or

vacuuming. If the binder is not soluble in the fluid, wet depowdering methods may be employed, like ultrasonic, microwave-induced boiling, CO_2 bubble generation and boiling fluid inside the internal channels [29].

1.4.5.2. Debinding

The debinding step in a fundamental step in post-processing of binder jetted parts because binder needs to be completely removed to avoid presence of impurities and changes in chemical composition in the final part; for example, residual carbon could diffuse inside the specimen during sintering and affect the ductility of the sintered part [32].

Different debinding techniques are available: the most common is thermal debinding, in which the binder is burnt off at a specific temperature for a defined time, chosen after thermogravimetric analysis of dried binder, but also catalytic debinding, solvent extraction and wick debinding. The last one is a method which uses capillary forces to absorb a molten phase from the bound part into a wicking material and it allows to reduce environmental impact from decomposition [41].

In most cases, the binder is a polymer, so it contains carbon-carbon, carbon-oxygen and carbon-hydrogen bonds that burn out over the same range of temperature: the majority of binder melt at less than 150 °C and evaporate in the range between 300 and 500 °C.

Debinding is usually performed during the initial stage of sintering in a protective atmosphere [30].

1.4.5.3. Sintering

Sintering was previously discussed in relation of powder metallurgy: this process is necessary to obtain densification of the printed parts and to eliminate porosity because pores are a reason of reduction of mechanical, thermal and electrical properties.

Sintering can be divided into three stages: initial, intermediate and final stage [29].

Initial stage is characterized by the formation of necks between particles and occurs at low temperature. In this stage, non-densifying mechanisms are dominant, which are surface diffusion, volume diffusion and vapor transport, in fact at the end of this step the densification is only 2-3%.

When the temperature is increased, the intermediate stage begins: grain boundary diffusion and lattice diffusion are dominant, so grain grows, pores merge and become tubular due to the transfer of mass from the convex to the concave regions.

In the final stage, densification can be obtained with the closure of isolated pores [32].

Powder size affects significantly the sinterability of the parts. Small particles have higher surface, so more contact points which can favor densification at a lower temperature [33].

Sinterability is influenced by powder size and it is defined as in Eq. 10 [32]:

$$\varphi = \frac{\rho_s - \rho_g}{\rho_{th} - \rho_g} \tag{10}$$

where ρ_s is the sintered density, ρ_g is the density of the green part and ρ_{th} is the theoretical density.

The typical thermal circle of a metal BJ process consists of two steps: debinding step, previously discussed, and sintering step. The time and temperature of each step should be properly selected.
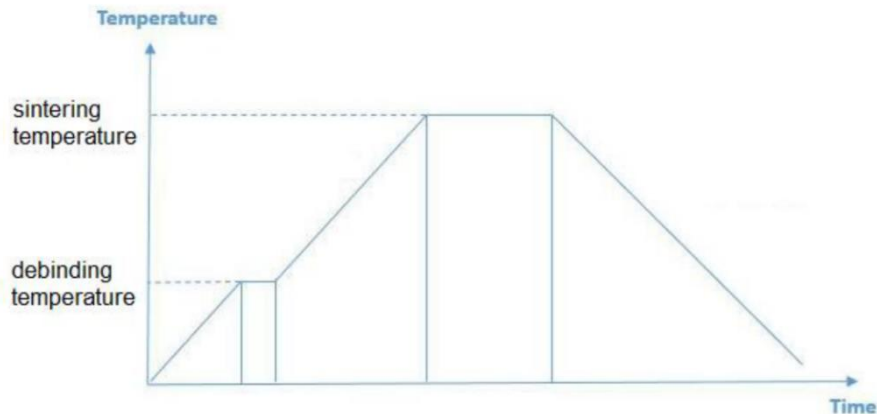
Figure 31 - Generic sintering profile for metal binder jetting process.

Bai and Williams [34] studied the effect of the variation of time, temperature and atmosphere on the density of sintered copper parts. They discovered that higher sintering temperature increased the final sintered density and shrinkage but time has not a strong influence, as a matter of fact the best sintered density is obtained after 4 hours instead of 6 hours. In addition, the copper samples did not melt or lose shape even at temperature close or higher than the melting temperature of copper, probably due to powder impurity or oxidation layers, responsible of the increase of melting point. If the sintering process is performed in a reducing atmosphere, due to the reduction of copper oxide and the removal of water vapor before the closure of pores it is possible to improve the final purity and density by more than 20 per cent compared to a non-reducing atmosphere.

In one of the most recent studies, Miyanaji et al. [38] investigated the influence of different sintering parameters, like sintering peak temperature and heating rate, on BJ parts printed with fine powder particles. They selected three different peak temperatures (900 °C, 950 °C and 1000 °C) and three different heating rates (1 °C/min, 2.5 °C/min and 5 °C/min). The peak temperature was kept for 180 minutes and sintering step was preceded by a debinding step at 450 °C for 60 minutes. The results showed that sintering peak temperature does not influence in significant way the final density, as long as it is at least 900°C due to the fact that at this range of temperature the closure of pores has already occurred completely. In addition, the heating rate of debinding and sintering processes should be low enough to allow complete binder removal and deoxidation process before pore closure.
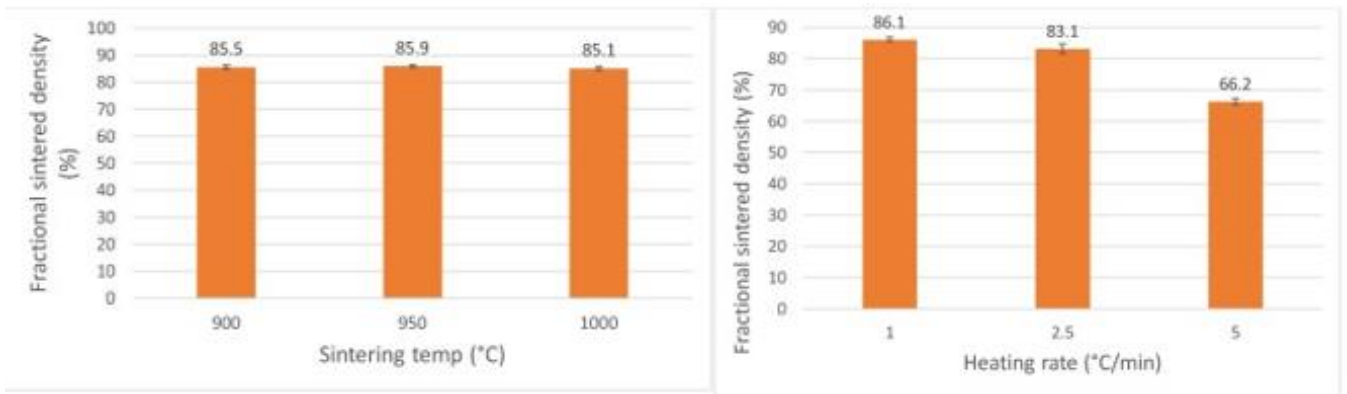
Figure 32 - Effect of sintering parameters on final part sintered density. Sintering temperature (left) does not significantly affect the final density, while heating rate (right) has an influence on sintered density. From [38].

Usually, to achieve full density infiltration is used: the pores of the material are filled with liquid metal or alloy, characterized by a lower melting point with respect to the main material. This technique guarantees a higher value of density but the purity of the final part is drastically affected. For this reason, different processes are studied to obtain high density and superior mechanical properties, like hot isostatic pressing (HIP) [32].

Kumar et al. [36] performed HIP after sintering to copper parts. The specimens were pressed with 206.84 MPa for 2 hours at 1075 °C. With this process, they were able to achieve a final relative density of 97.3% and good mechanical and electrical properties.

2. Materials and methods

2.1. Characterization of copper powder

The characteristics of powder particles have a direct influence of behavior during additive manufacturing processes [51].

The factors that play an important role are [52]:

- Size distribution, which will affect the packing density and resolution of the final part.
- Shape distribution, which will determine the efficiency of the particles packing.
- Density, due to the fact that particles may include closed voids.
- Surface area, because it affects sinterability of the part.
- Chemical composition, because the presence of impurities affects mechanical and thermal properties of the final product.
- Flowability, an important property in binder jetting application because it allows a faster printing process.

In binder jetting, it is important to evaluate the possibility to reuse the unbounded powder after the printing and curing process. For this reason, several analyses were performed on as-received powder and powder cured at 180 °C for 2, 4 and 6 hours in order to compare the properties of the material before and after the curing process.

2.1.1. Granulometric analysis

The material used in this work was gas atomized powder copper (m4p^{TM} pureCu.04, item 70594), provided by m4p material solutions GmbH (Fig. 33). The chemical composition and the particle size distribution provided by the supplier are shown in Table 2 and 3, respectively.
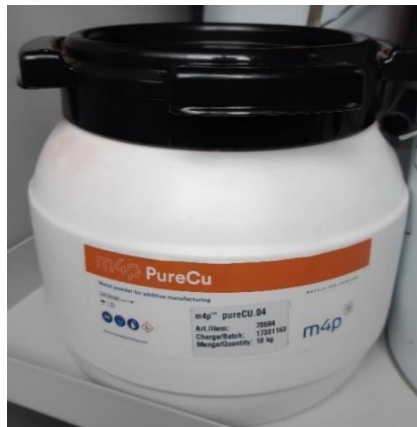
Figure 33 - Gas atomized powder provided by m4p materials solutions GmbH.

Table 2 – Chemical composition of the as-received powder provided by the supplier.

	Cu	O
%wt	>99.95	0.03
%wt min	99.95	-

	D10	D50	D90
Particle size (µm)	5.8	11.3	16.6

A static automated imaging analyzer, the Malvern Panalytical Morphologi 4 (Fig. 34), was used to characterize the as-received and the cured copper powder in terms of particle shape (circularity) and size distribution [53].

The powder sample was put on the sample holder and the instrument captured images of individual particles by scanning the material, illuminated from below with a white light LED.

Figure 34 - Malvern Panalytical Morphologi 4 automated imaging analyzer.

An automated segmentation analysis was performed to calculate the morphological properties of each particle.

CE diameter parameter is the diameter of the circle with the same area of the 2D digital image of the analyzed particle [54].

3D particle → Captured as a 2D image → Converted to a circle of same area → Diameter of circle measured
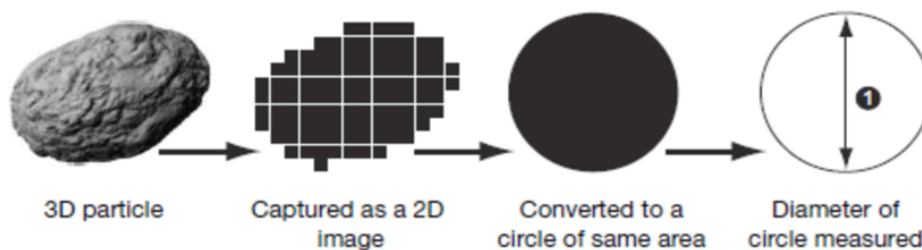
Figure 35 - Determination of CE diameter parameter of a 3D particle. From [54].

Circularity is defined as the degree to which the particles is similar to a circle, taking into consideration the smoothness of the perimeter, so it is a measure of both particle shape and surface roughness and it can be calculated as in Eq. 11 [55].

$$C = \sqrt{\frac{4\pi A}{P^2}} \tag{11}$$

A is the area and P is the perimeter of the particle image. If the value of circularity is 1, the particle is perfectly spherical.

If the particles have a complex geometry, the edges can interfere with particle movement and flow [56].

2.1.2. Rheometric analysis

Rheometric analysis gives information about the flowability and density of powder.

For a powder, the density can be defined in different ways [53].

True density (ρ_s) is the ratio of the mass of the particle excluding inside closed voids, so it is the density of the material composing the particle.

Particle density (ρ_p) is defined as the particle mass divided by the particle volume, including the closed voids.

Bulk density (ρ_b) is applied in case of powder beds: it is the ratio of the mass of the powder bed in a container to the volume of the bed, including the empty voids between particles.

The apparent density (ρ_{ap}) is the density of the powder as poured, while the tapped density (ρ_t) is the density after the application of mechanical tapping on the container.

The porosity (ε) is defined as the fraction of the volume of voids over the total volume of the bed:

$$\varepsilon = 1 - \frac{\rho_b}{\rho_p} \tag{12}$$

Alternatively, Hausner ratio can be used to compare flowability between different particles. It is the ratio of apparent density to tapped density [57]:

$$HR = \frac{\rho_t}{\rho_{ap}} \tag{13}$$

If the Hausner ratio is small, the flowability of the powder should be suitable for binder jetting.

FT4 Powder Rheometer (Fig. 36) is used to perform this analysis on fresh copper powder. First, apparent density is calculated by weighing the powder mass in a calibrated recipient. Then, a precision blade is rotated and moved downwards through the powder to establish a flow pattern and remove macro-porosities. Finally, the material is compacted to remove residual excess air and tapped density is calculated.
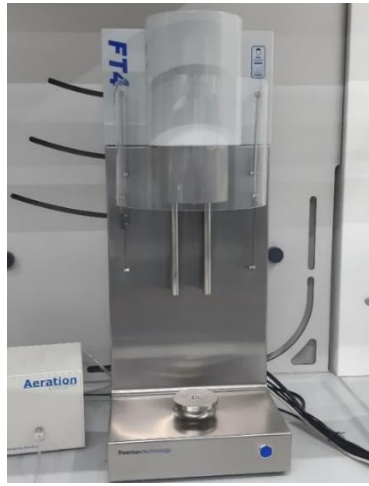
Figure 36 - FT4 Powder Rheometer.

2.1.3. SEM analysis

A Zeiss EVO 50 and a Zeiss Sigma 500 scanning electron microscopes (Fig. 37) were used to characterize the microstructure of as-received powder and cured powder.
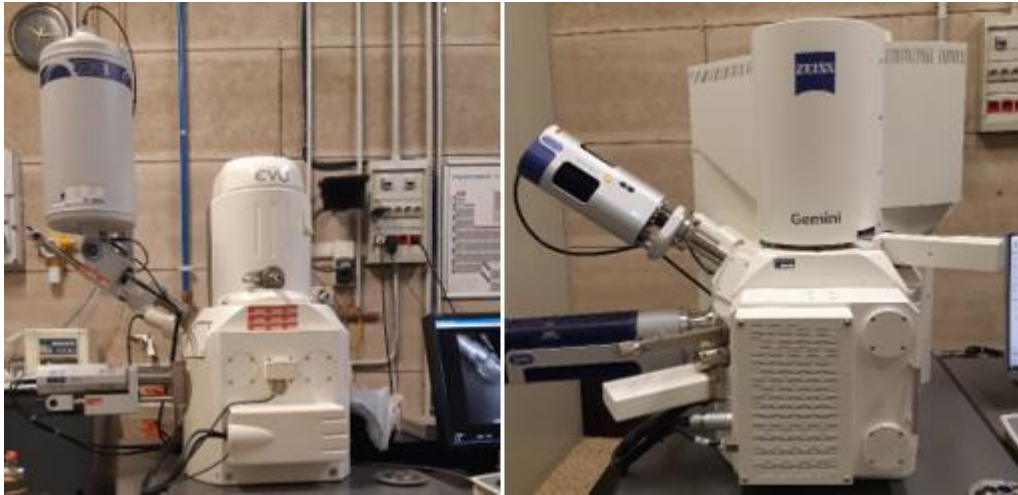
Figure 37 - Zeiss EVO 50 (left) and Zeiss sigma 500 (right) SEM.

Powder particles surface and sections were analyzed. Encapsulated samples were prepared by mixing a small amount of powder with approximately the same amount of thermosetting resin in the form of powder and put in the internal cylinder of a Hitech Europe EP15 pneumatic mounting press (Fig. 38). Then, another extra cup of resin was added. A pressure of 4 bar was applied with the sealing piston and the temperature was increased up to 175 °C to allow the resin to melt and reticulate. Then, the temperature was decreased to 30 °C and the embedded specimen was taken out of the press.

Figure 38 - Hitech Europe EP15 pneumatic mounting press.
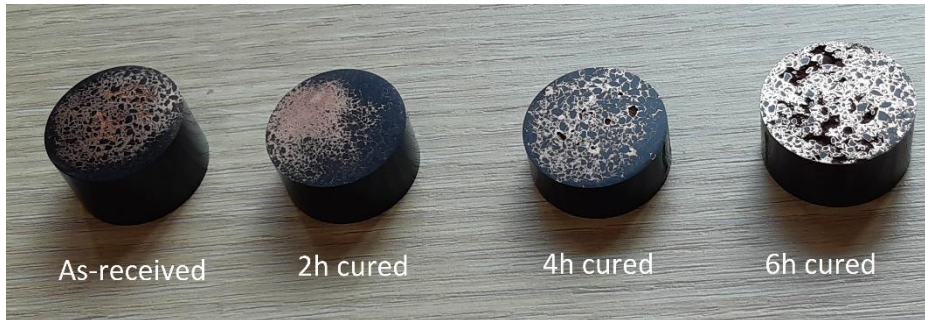
Figure 39 - Resin embedded powder samples for SEM analysis.

Resin embedded powder samples were grinded and polished to expose the cross-sectional surface of powder particles. Grinding was performed with a Hitech Europe MP311T metallographic grinding machine (Fig. 40 (a)), using WS FLEX 18 C Waterproof grinding papers from 600 to 2500 grit. The direction of rotation was changed when moving to the next paper and water was continuously supplied to reduce frictional heating. Polishing was performing with a Hitech Europe MP 22-22 V metallographic polishing machine (Fig. 40 (b)), using polishing cloths and Hitech Europe 154234 diamond pastes with 6 μm and 1 μm particle size. Lastly, the samples were washed after each step with water and soap to remove contaminants and dried with compressed air gun.

Two as-received powder samples were prepared: one was analyzed without other treatments, the other one was chemically etched in order to reveal the microstructure of the powder and grain boundaries. The surface of the sample was immersed for 10 seconds in a solution prepared with 10 g of ferric chloride $FeCl_3$, 50 ml of hydrochloric acid HCl, 10 ml of nitric acid HNO_3 and 100 ml of water.
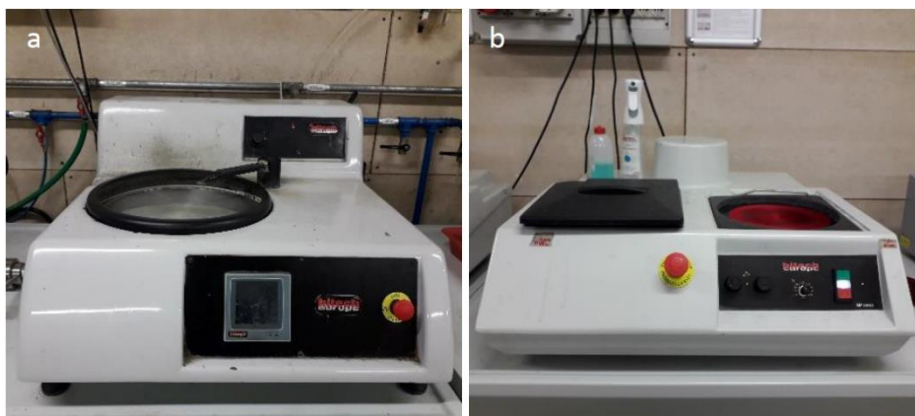
Figure 40 - (a) Hitech Europe MP311T metallographic grinding machine and
(b) Hitech Europe MP 22-22 V metallographic polishing machine.

Figure 41 - Agar auto sputter coater.

The Zeiss EVO 50 scanning electron microscope was employed for qualitative determination of the oxygen presence by EDS analysis in the powder cured for 2, 4 and 6 hours.

Figure 42 - Cured powder samples used in SEM analysis.

2.1.4. XRD analysis

A Rigaku SmartLab X-ray diffractometer (Fig. 43) was used to perform the analysis, employing an X-ray radiation peak Cu Kα_1 with 1.5406 Å wavelength. Patterns were collected from 20° to 100° with 0.02° step size.

In order to detect the presence of copper oxides in the cured powder samples, the diffraction patterns of the three cured specimens were compared with the diffraction pattern of pure copper, cuprous oxide Cu_2O, also called cuprite, characterized by cubic structure, and cupric oxide CuO, known with the name of tenorite and with a monoclinic structure.
As-received powder was also analyzed to detect impurities in the starting material and to compare the diffractogram with the one obtained from cured powder.

Figure 43 - Rigaku SmartLab X-ray diffractometer.

2.2. Production and characterization of green parts

2.2.1. First series of printing processes

Copper binder jetted specimens were fabricated with ExOne Innovent+ printer (Fig. 44), utilizing a water-based binder provided by ExOne. Three different printing processes were done, in order to evaluate the effect of curing in air on the material composition. Four specimens with dimensions 12.5 x 18.75 x 3 mm were fabricated in each process. The process parameters were selected according to previous studies on binder jetting of fine pure copper powder and are listed in Table 4 [38].

Figure 44 - ExOne Innovent+ binder jetting printer.

Figure 45 - Main components of ExOne Innovent+ printer.
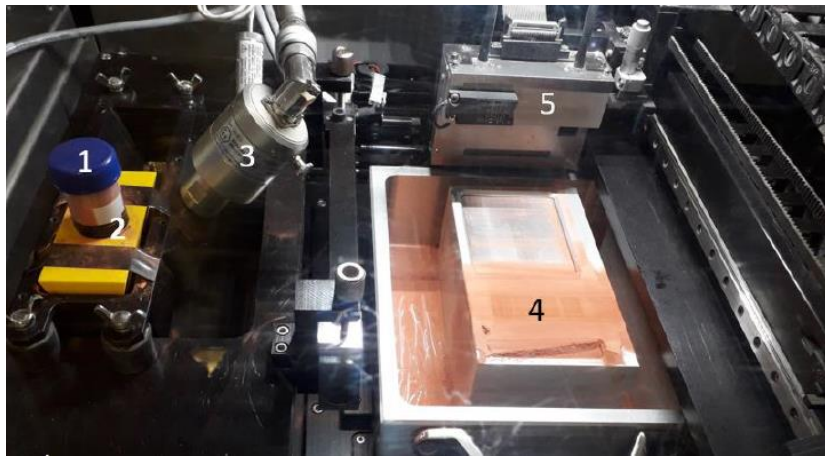
Key
1 hopper
2 sieve
3 overhead heater
4 powder bed
5 printhead

Table 4 - Parameters used to print the first series of specimens.

Binder saturation ratio (%)	90
Layer thickness (µm)	50
Powder bed temperature (°C)	55
Drying time (s)	12
Ultrasonic intensity (%)	75
Recoating speed (mm/s)	25
Roller transverse speed (mm/s)	5
Roller rotational speed (rpm)	700

A binder saturation ratio of 90% was chosen to obtain more resistant green parts and the choice of a small value of layer thickness was allowed by using fine copper powder, with a D90 lower than 10 µm.

The printed parts were cured in air in a Yamato DX412C drying oven (Fig. 46) to polymerize the binder and improve the strength of green parts for handling and depowdering. The curing temperature was set at 180 °C and the time was different for each printing process (2, 4 and 6 hours). After the curing, the excess powder war removed with a brush.

Figure 46 - Yamato DX412C drying oven.

2.2.2. Second series of printing processes

Another series of three printing process was performed with ExOne Innovent+ printer. 15 samples with dimensions 30 x 5 x 5 mm were printed in each process to evaluate the effect of different values of saturation ratio. For this reason, the binder saturation ratio was varied (90, 100 and 110%), while the other parameters were kept constant.

Table 5 - Parameters used to print the second series of specimens.

Binder saturation ratio (%)	Varied (90, 100, 110)
Layer thickness (µm)	50
Powder bed temperature (°C)	50
Drying time (s)	12
Ultrasonic intensity (%)	75
Recoating speed (mm/s)	50
Roller transverse speed (mm/s)	5
Roller rotational speed (rpm)	700
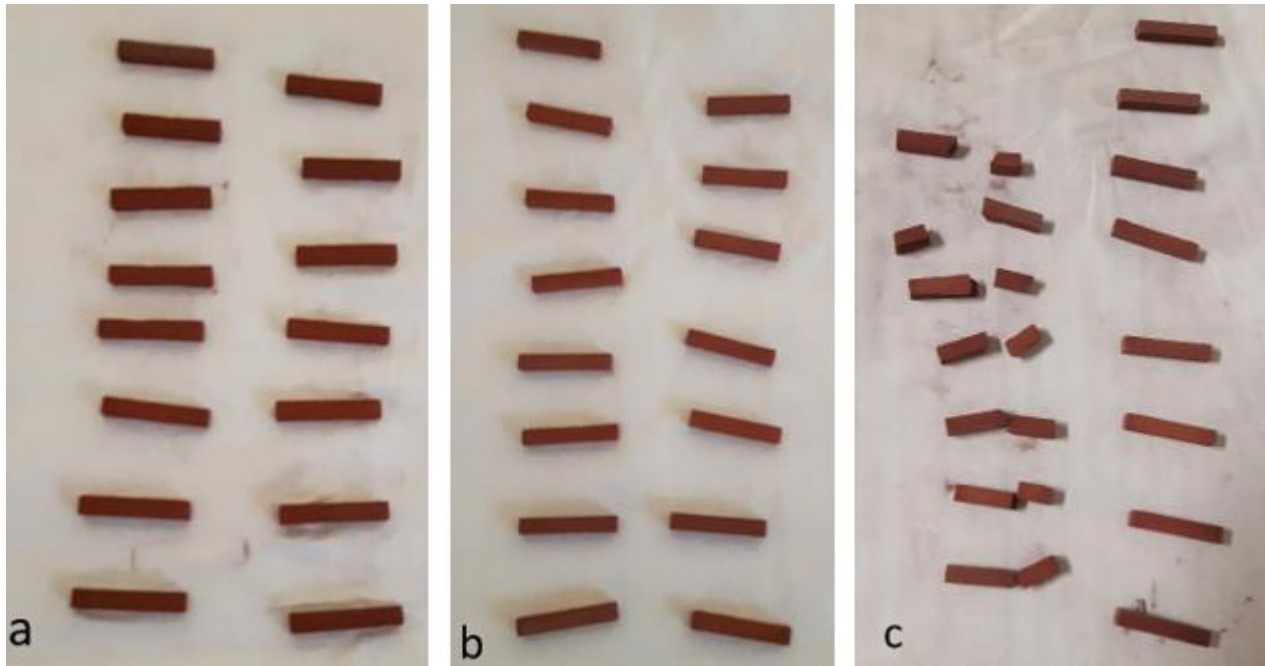
Figure 47 - Second series of specimens: (a) specimens with binder saturation ratio 90%; (b) specimens with binder saturation ratio 100% and (c) specimens with binder saturation ratio 110%.

At the end of the depowdering process, the green specimens were measured and weighed with a Scaltec SBC 22 electronic scale (Fig. 48, left) in order to calculate the relative density and observed with a Nikon Eclipse LV250NL optical microscope (Fig. 48, right).

*Figure 48 - Scaltec SBC 22 electronic scale (left) and Nikon Eclipse
LV250NL optical microscope (right).*

2.3. Production and characterization of brown parts

2.3.1. Debinding

After curing the green parts still contain binder to hold the powder together, which is an impurity and it needs to be removed [30].

A Carbolite tube furnace (Fig. 49) was employed to perform debinding in argon atmosphere up to 470 °C, with a holding time of 4 h, with a 5 °C/min heating rate.

Figure 49 - Carbolite tube furnace.

2.3.2. DSC and TGA analysis

Differential scanning calorimetry (DSC) is a thermoanalytical technique in which the difference in the amount of heat required to increase the temperature of the sample and reference is measured as function of temperature. The sample and a reference crucible are placed on a sample holder and heated in order to detect physical transformations like phase transitions.

Thermogravimetric analysis (TGA) is a method of thermal analysis in which the mass of the sample is measured over time as the temperature changes. It provides information about physical phenomena, such as phase transitions, absorption, adsorption and desorption, and chemical phenomena like thermal decomposition and oxidation or reduction reactions.

A Setaram Labsys device is used to perform the analysis (Fig. 50). During both analyses, the specimen is held in an alumina crucible, connected to a thermocouple used to heat the system. Alumina is employed due to its high thermal stability at high temperatures [58].

Figure 50 - Setaram Labsys device (left) and alumina crucible used to perform the test (right).

Both analyses were performed in an inert atmosphere, with argon in order to avoid oxidation or other chemical reactions with reactive gases and in a range of temperature going from room temperature to 1100 °C with a heating rate of 20 °C/min [1].
Then, the temperature was maintained for 2 minutes and finally the specimen was cooled down to room temperature with rate of 30 °C/min.

2.3.3. Dilatometry analysis

Dilatometry analysis were performed to determine the correct thermal sintering treatment.
A Linseis L75 vertical dilatometer (Fig. 51) was used to study the dilatometric behavior of the specimens.
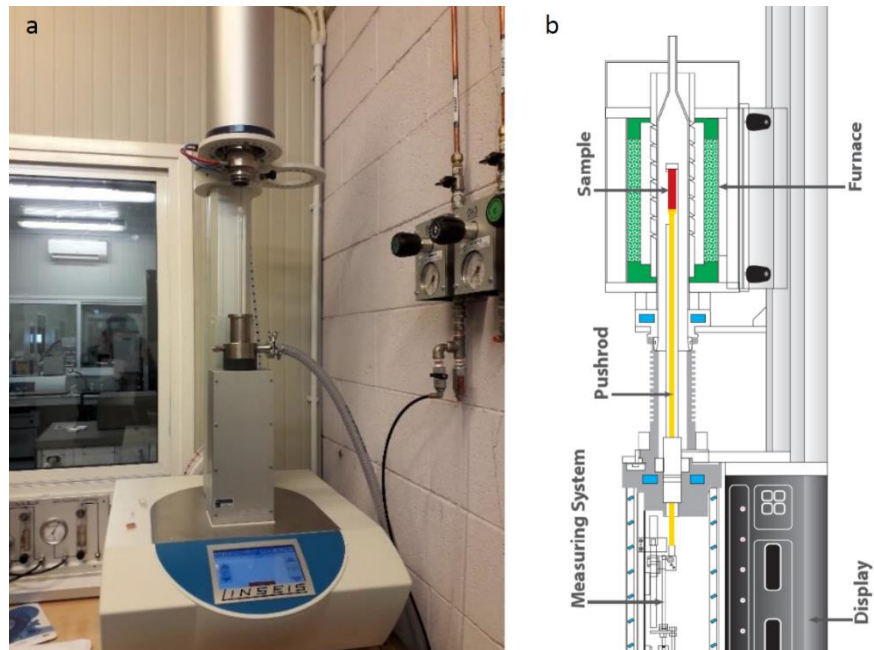
Figure 51 - (a) Picture and (b) schematic of Linseis L75 vertical dilatometer.

Dilatometry analysis consists in the measurement of the variation of the length of the specimen as a function of the change in temperature. The sample was put inside a cylindrical sample holder made of alumina and supported above and below by two alumina disks and everything was put inside a furnace with controlled atmosphere. The real temperature of the sample during the experiment was recorded with a type S thermocouple, made by platinum and rhodium. The other end of the push rod was attached to the linear variable differential transformer (LVDT), consisting of a movable core, one primary coil and two secondary coils put in series with reversed polarity. When the core is in the center position, the induced voltage in the secondary coils have the same amplitude, while when the core moves, the coupling between primary and secondary coils changes. For this reason, when the length of the sample varies, the amplitude of the output voltage changes [59].
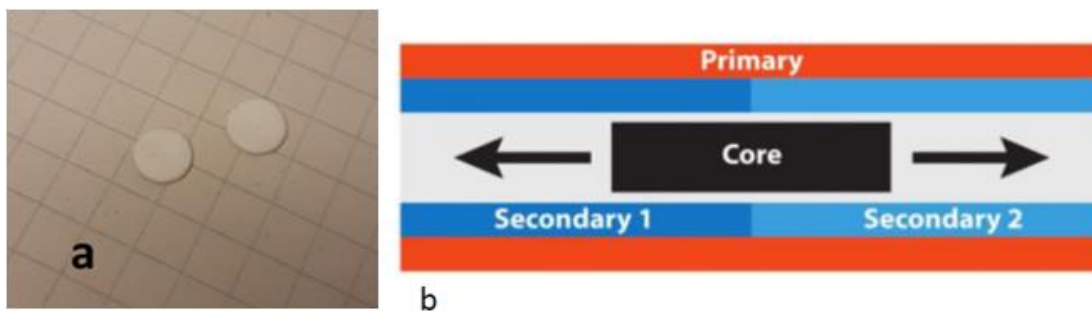
Figure 52 - (a) Alumina disks used to hold the sample and (b) schematic of a LVDT. From [59].

From the dilatometric curves, it is possible to identify the thermal events occurring during the experiment and to evaluate the final shrinkage of the part, therefore determining the best sintering treatment in order to obtain the most suitable values of density and final properties.
The dilatometric curves were plotted with the deformation as a function of temperature. The percentage elongation, which corresponds to linear shrinkage, is calculated as following:

$$\varepsilon = \frac{\Delta L}{L_0} \cdot 100 = \frac{L - L_0}{L_0} \cdot 100 \tag{14}$$

L_0 is the initial length of the specimen and L is the length at a given time or temperature. The total dilatometric curve was corrected by subtracting the contribution of two alumina disks used to keep the specimen fixed.

The linear coefficient of thermal expansion (CTE) can be calculated as following:

$$\alpha = \frac{1}{L_1} \frac{\Delta L_2 - \Delta L_1}{T_2 - T_1} = \frac{1}{L_0 + \Delta L_1} \frac{\Delta L_2 - \Delta L_1}{T_2 - T_1} \tag{15}$$

CTE was calculated using the data from the dilatometric curves in the range of 50-200 °C, in the range where no particular thermal event is expected to occur, with a temperature step of 10 °C.

Different dilatometry analyses were performed:

- The specimen dubbed DIL1 was heated in inert atmosphere, with argon as inert gas, from room temperature to 1050 °C, then cooled.
- The specimen called DIL2 was heated in vacuum (approximately 10^{-2} mbar) from room temperature to 1050 °C, then cooled.
- The specimen labeled DIL3 was heated in vacuum from room temperature to 900 °C, the temperature was maintained for 1 hour and then cooled.
- The specimen named DIL4 was heated in vacuum from room temperature to 900 °C, the temperature was maintained for 3 hours and then cooled.
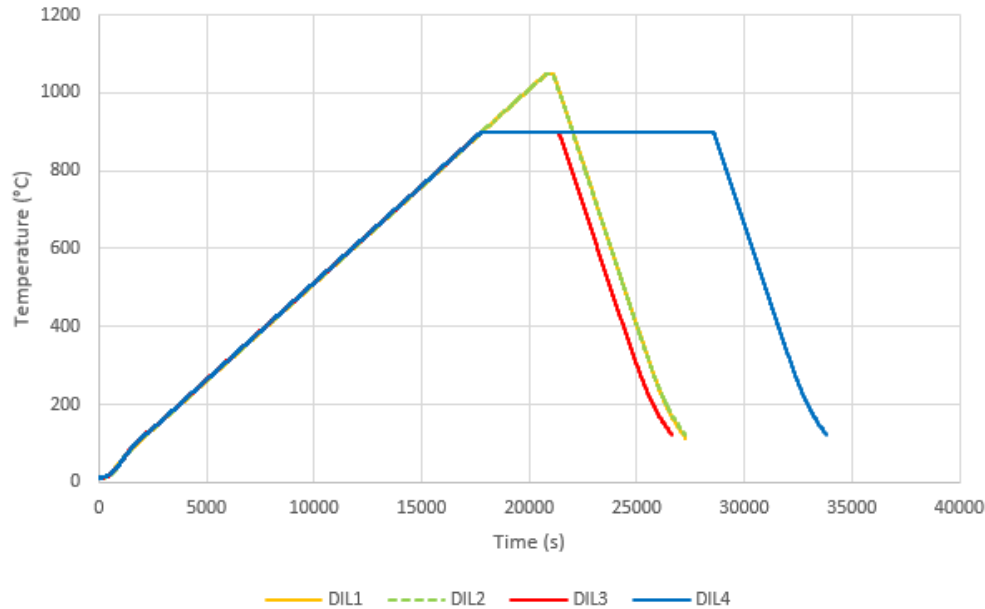
Figure 53 - Temperature profiles used in dilatometry experiments.

The peak temperatures were selected considering the fact that 1050 °C is very close to melting temperature of copper, which is 1085 °C [1], and 900 °C is about 80% the melting temperature of copper and it is a common temperature used for sintering of this material [38]. The heating rate was 3 °C/min, selected to avoid a too fast heating of the specimen, while the cooling rate was 10 °C/min.

2.3.4. Density evaluation of dilatometry samples

After the dilatometry analysis, all the specimens were weighted according to Archimedes' principle using a Mettler Toledo scale (Fig. 54) to evaluate their density. They were firstly weighted in air, then immersed in ethanol to determine their apparent mass. Lastly, the density was calculated using the following equation:

$$\rho = \frac{w_{air} \cdot \rho_{eth}}{w_{air} - w_{eth}}$$

(16)

In the equation, w_{air} is the mass of the specimen in air, w_{eth} is the apparent mass of the sample when it is immersed in ethanol and ρ_{eth} is the density of ethanol at 21 °C or 22 °C, respectively 0.7886 and 0.7875 g/cm^3 [60].

Three measurements were done for each specimen and relative density was calculated, knowing that the density of bulk copper is 8.92 g/cm^3.

Figure 54 - Mettler Toledo scale.

Brown parts could be weighted with immersion method due to the fact that the porosity is very low compared to the value of green parts and the fact that water-based binder has evaporated, so it cannot dissolve in the liquid used for the measurement and the ethanol cannot be absorbed inside the pores.

2.3.5. Optical analysis of dilatometry samples

After the evaluation of density of brown parts, the specimens were embedded in thermosetting resin, polished with Hitech Europe metallographic machines with grinding papers from 600 to 2500 grit, then with diamond pastes with 6 μm and 1 μm particle size.

After that, the specimens were observed with SEM and optical microscope in order to evaluate the microstructure and analyzed with EDS to detect impurities and oxygen quantity.

Figure 55 - Resin embedded brown specimen for SEM analysis.

2.4. Production and characterization of sintered parts

2.4.1. Thermal treatment in hydrogen atmosphere

After printing and curing, some of the binder jetted samples belonging to the second series of printing processes were sintered in an industrial furnace with controlled atmosphere provided by FILMS S.p.A. – OMCD Group in Anzola d'Ossola (VB).
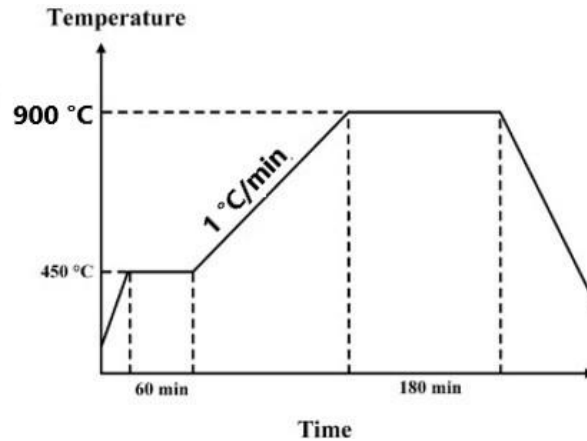
Figure 56 - Sintered profile of the thermal treatment. Adapted from [38].

The thermal cycle was performed in a reducing 50:50 H_2/N_2 atmosphere to promote reduction of copper oxide and improve the final density. Firstly, the temperature of the furnace was raised up to 450 °C and maintained for 60 minutes to burn off the binder. Then, after the debinding step, the temperature was increased at 1 °C/min up to 900 °C and maintained for 3 hours. This cycle was chosen based on the previous studies on binder jetting of copper [38] [34] [36].
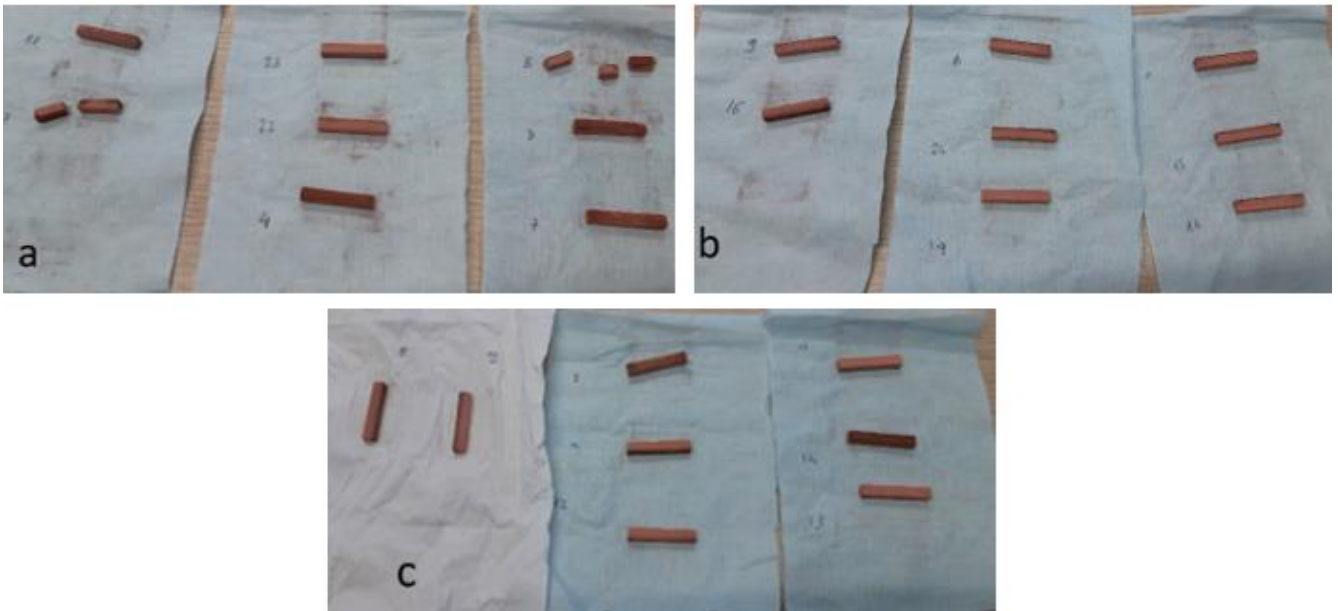
Figure 57 - Sintered specimens: (a) specimens with binder saturation ratio 90%; (b) specimens with binder saturation ratio 100% and (c) specimens with binder saturation ratio 110%.

After the thermal treatment, the specimens were measured to calculate the difference between the green parts and the final volumes, so the shrinkage, and they were weighted with Scaltec SBC 22 electronic scale to calculate the relative density.

Then, they were observed with optical microscope to evaluate their microstructure and some of them were embedded in thermosetting resin and polished only with grinding papers due to the fact that they were not fully sintered. Finally, they were analyzed with SEM and EDS to detect possible residual oxide.

Figure 58 - Resin embedded sintered specimens.

2.4.2. Thermal treatment in inert atmosphere

A different thermal treatment was performed to avoid the use of hydrogen atmosphere, expensive and risky.

The brown parts were sintered in Lenton furnace with controlled atmosphere (Fig. 59).

The thermal cycle consisted only of the sintering step, since the water-based binder was already removed with debinding process and it was performed in argon. The parts were treated with a heating rate of 5 °C/min up to 1000 °C, then the temperature was maintained for 3 hours.

The specimens were put inside a refractory alumina tube closed by glass fiber stoppers (Fig. 60) to create a small, closed chamber to avoid pumping of an excessive volume of gas.

Figure 59 - Lenton furnace in which thermal treatments were performed.
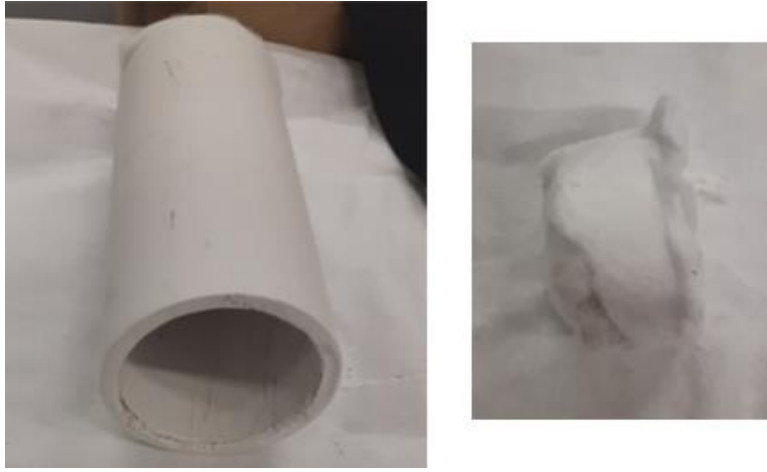
Figure 60 - Alumina tube (left) and glass fiber stopper (right).

The first specimen was simply placed inside the tube, while with the second sample, labelled G1, a piece of graphite was added to create a reducing atmosphere. The last part, denominated G2, was put inside a graphite crucible and covered with a piece of graphite (Fig. 61) to improve reduction of copper oxide.
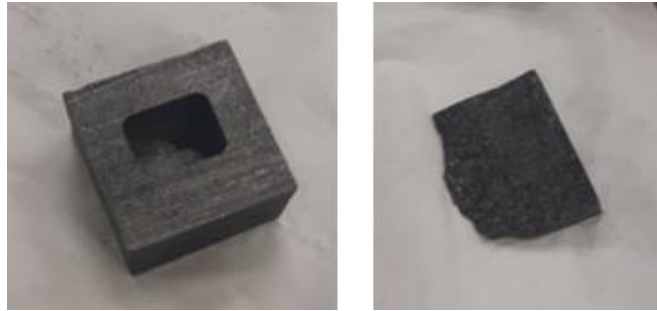
Figure 61 - Graphite crucible (left) and piece of graphite (right) used to close the crucible.

Another specimen, identified with G3, was treated with the same parameters (1000 °C, heating rate of 5 °C/min, holding time of 3 hours) in air instead of inert atmosphere, to boost production of CO and to promote reduction of copper oxide. This part was placed inside a graphite crucible and covered with a piece of graphite too.

After the thermal treatment, the specimens were embedded in thermosetting resin and polished with grinding paper from 600 to 2500 grit, then with diamond pastes with 6 μm and 1 μm particle size.

Figure 62 - Resin embedded sintered specimens for SEM analysis.

The embedded specimen were observed with optical microscope and with SEM to analyze their microstructure.

3. Results and discussions

3.1. Characterization of copper powder

3.1.1. Granulometric analysis

Figure 63 shows the normalized frequency and cumulative size distribution curves of the as-received copper powder and the powder size characteristics are listed in the Table 6.

The sample of powder has a broad size distribution, with a range from 0.39 µm to 42.98 µm, with peaks at 0.4 µm and around 2 µm.

In the Figure 64, the relative frequency curve of circularity is shown. It demonstrates how the majority of particles has a circularity value close to 1, as expected for a gas atomized powder.
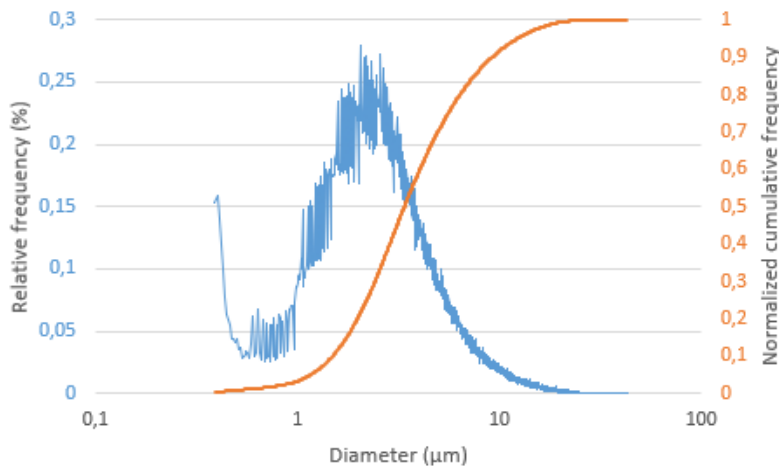
Figure 63 - Normalized frequency and cumulative size distribution curves of the as-received powder.

Table 6 - Powder particles size characteristics.

	D10	D50	D90
Particle size (µm)	1.5	3.39	9.25
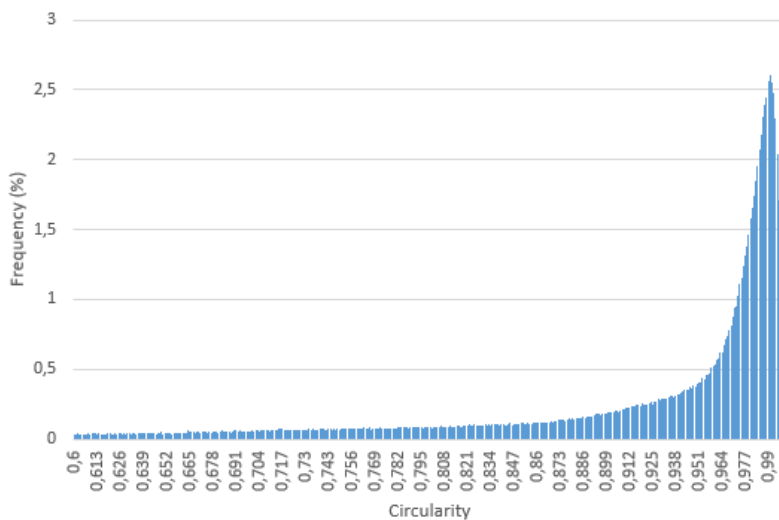
Figure 64 - Relative frequency curve of circularity of the as-received powder.

3.1.2. Rheometric analysis

Three different measurements were done: in the following tables it is possible to find the values of apparent density and tapped density. Then, the relative density is calculated, dividing the obtained values by the bulk density of copper (8.96 g/cm^3).

Table 7 - Measured values of apparent and relative density of the as-received powder.

	1	2	3	Average	Standard deviation
Apparent density (g/cm^3)	4.59	4.61	4.59	4.60	0.01
Relative density (%)	51.25	51.48	51.22	51.32	0.00

Table 8 - Measured values of tapped and relative density of the as-received powder.

	1	2	3	Average	Standard deviation
Tapped density (g/cm^3)	5.1	5.23	5.41	5.25	0.13
Relative density (%)	56.92	58.37	60.38	58.56	0.01

With these data, Hausner ratio was calculated:

Table 9 - Computed values of Hausner ratio.

1	2	3	Average	Standard deviation
1.11	1.13	1.18	1.14	0.03

After granulometric and rheometric analysis, it can be seen that the flowability of the powder is very good, since the particles are almost perfectly spherical and Hausner ratio has values very close to 1 [57]. The good flowability is confirmed experimentally during the printing process.

3.1.3. SEM analysis

The Figure 65 shows how the as-received powder particles are spherical and they are characterized by different sizes, coherently with the results mentioned above.
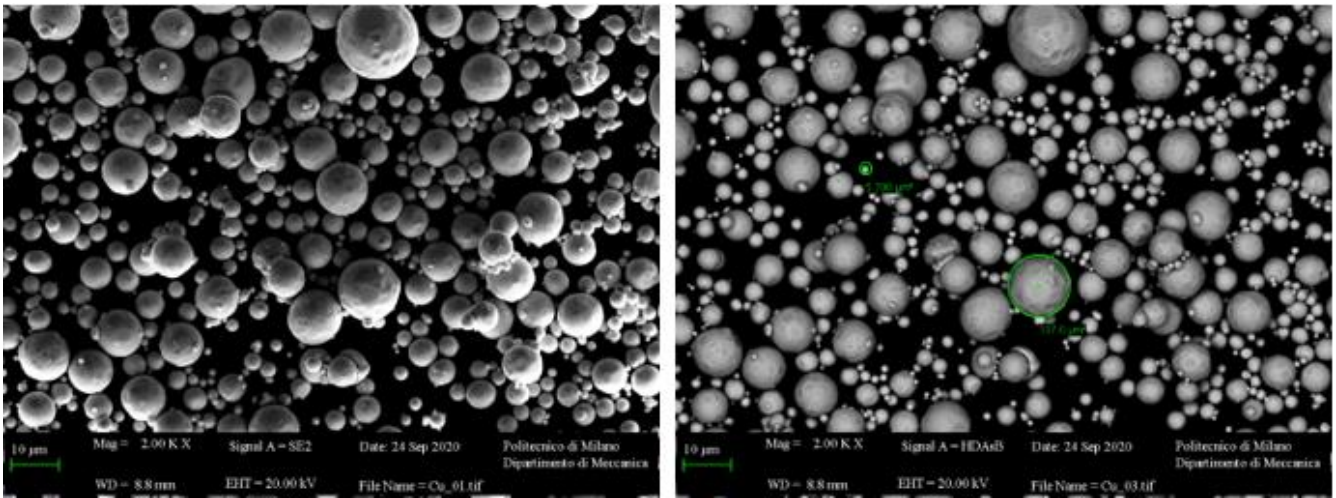
Figure 65 - SEM micrographs of as-received powder.

In Figure 66, the SEM micrographs of the cross-section of the as-received powder particles are shown. The dark lines highlight the grain boundaries, which were revealed by chemical etching, and larger particles may contain several grains with size up to 10 μm, while small particles are made up of one or few grain.
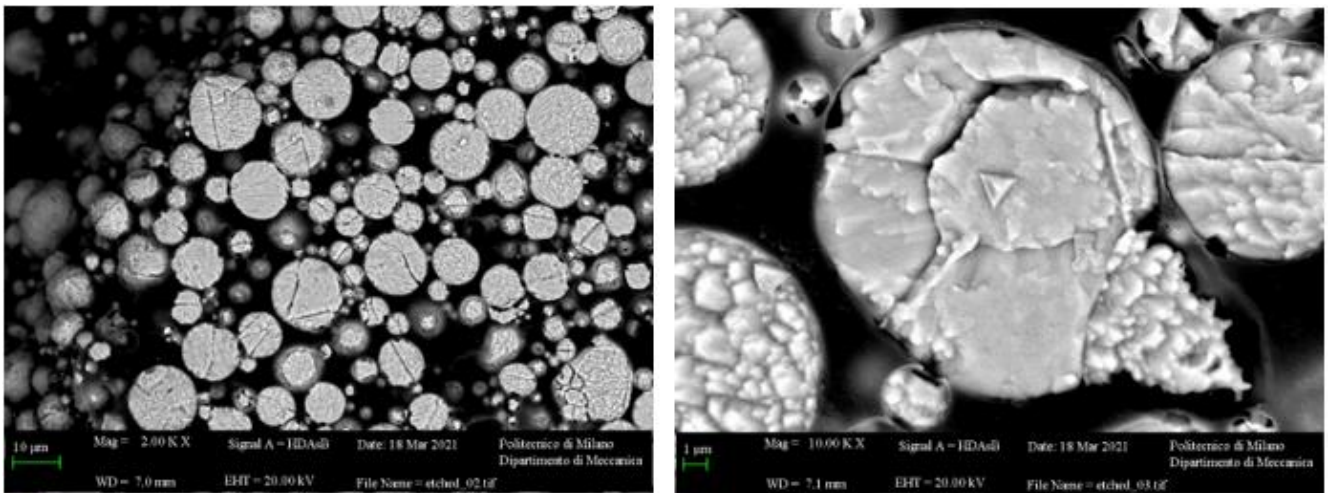
Figure 66 - SEM micrographs of the cross-section of the as-received powder.

Figure 67 shows the SEM micrographs of powder samples cured at 180 °C for 2, 4 and 6 hours, obtained using secondary electrons. The number are an index of the points where the EDS microanalysis was performed. In Table 10 the results of EDS analysis are reported. The tag "map" indicated the average chemical composition of a large area of the powder samples.
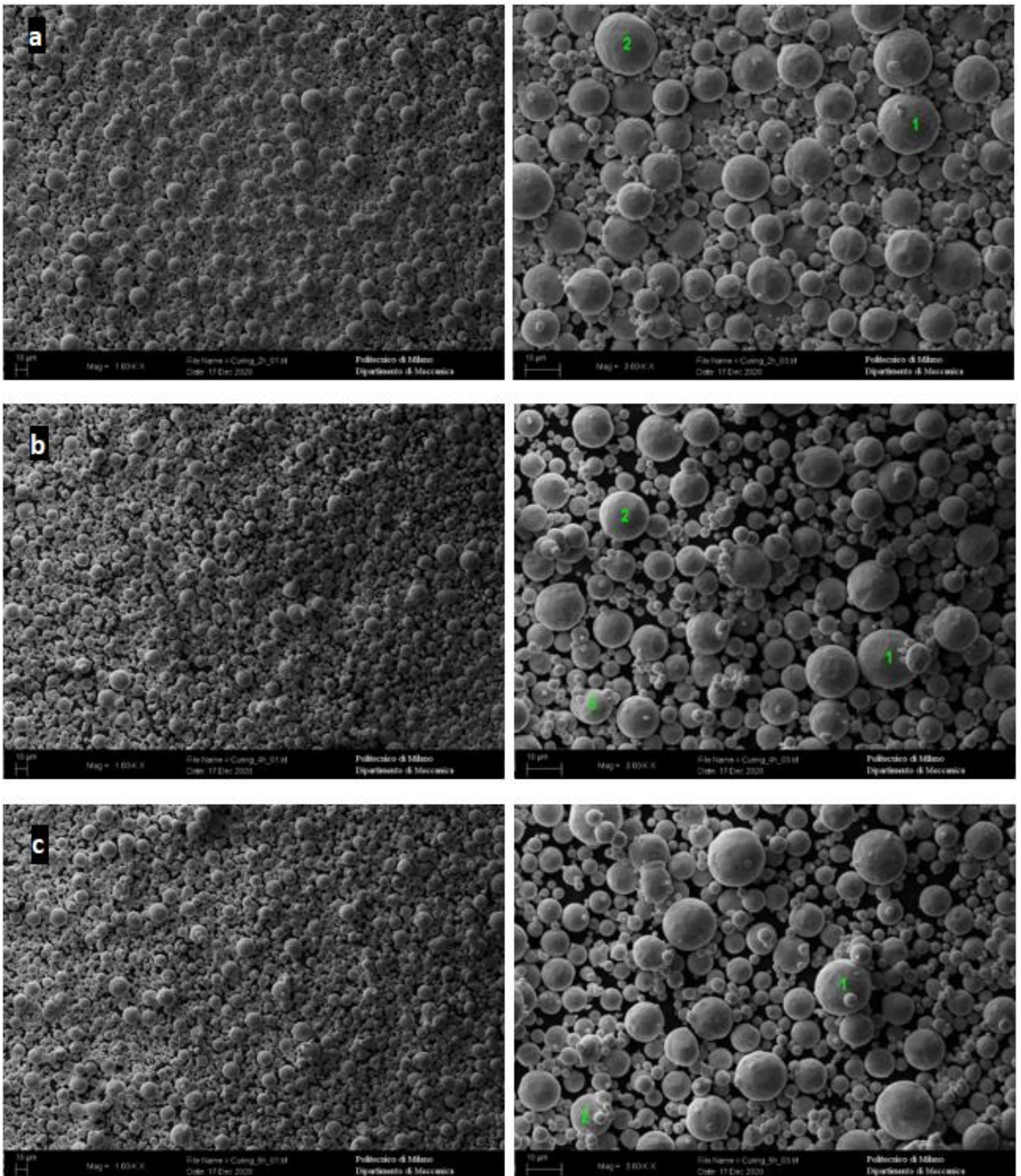
Figure 67 - SEM micrographs of copper powders cured at 180 °C for (a) 2 hours, (b) 4 hours and (c) 6 hours.

51

Table 10 - Results of EDS analysis performed on cured powder specimens.

Curing time (h)	Analyzed region	Cu (wt%)	O (wt%)
2	1	97.75	2.25
2	2	97.66	2.34
4	1	97.89	2.11
4	2	100	0
4	3	95.56	4.44
4	map	97.22	2.78
6	1	96.86	3.14
6	2	96.08	3.92
6	map	97.99	2.01

Table 11 - Maximum and minimum values of copper and oxygen

	Cu (wt%)	O (wt%)
Max.	100	4.44
Min.	95.56	2.01

EDS analysis shows that the oxidation of copper powder occurred during the curing treatment.

However, there are no significant differences in oxygen content between specimens undergoing different curing times. Therefore, it is possible to perform curing for 6 hours without an excessive oxygen formation (around 2-3%), in order to obtain better mechanical properties in the green bodies. For this reason, the parts obtained with second binder jetting printing process were cured at 180 °C for 6 hours.

In addition, smaller particles contain more oxygen. Indeed, the small particles marked with number 3 in Figure 67 (b) and number 2 in Figure 67 (c) have about 4 wt% oxygen content, while bigger particles are characterized by an oxygen content lower than 3 wt%. This is due to the formation of a superficial oxide layer with limited thickness and to the fact that smaller particles have higher surface-to-volume ratio, so they are more reactive [38].

The cross section of as-received and cured powders were observed to detect the presence of the previously mentioned oxide layer. The results of EDS analysis are reported in the table.
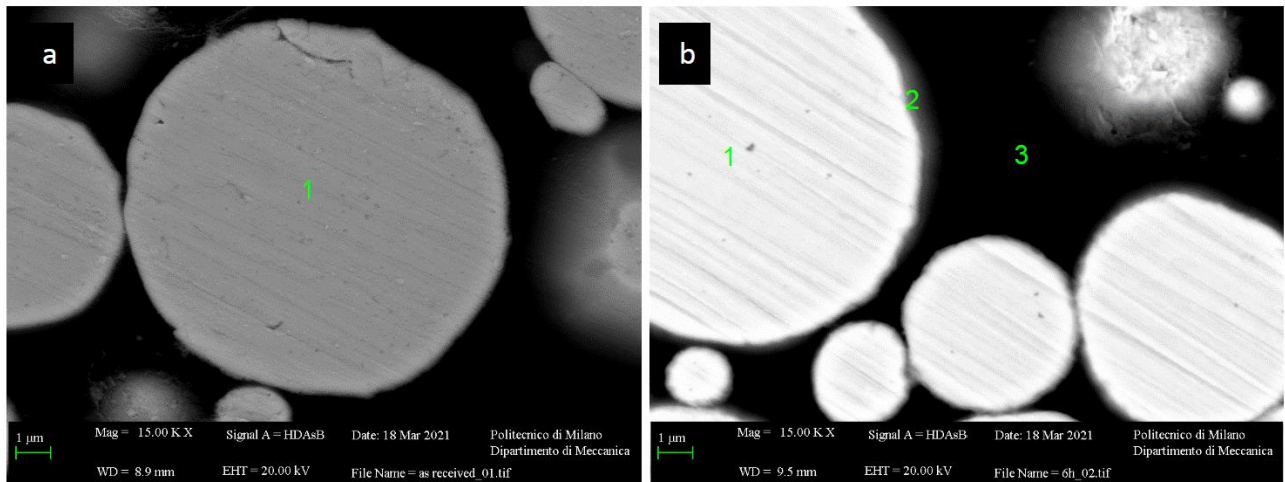
Figure 68 - SEM micrographs of the cross-section of as received powders.

Table 12 - Results of EDS analysis performed on as-received and cured powder specimens.

Curing time (h)	Analyzed region	Cu (wt%)	O (wt%)	C (wt%)
-	1	80.95	0.2	18.35
6	1	79.6	0.4	19.9
6	2	25.7	6.8	67.6
6	3	44.5	3.8	51.7

EDS analysis showed that the fresh powder does not contain oxygen internally, suggesting that oxidation occurs during the curing treatment.

Three different areas of the 6 hours cured sample were analyzed. The region in the particle core identified with number 1 is mainly made of copper. The region tagged with number 3 is the resin, where carbon content is obviously prevailing. The point labelled with number 2 has a significant higher oxygen content compared to both the particle core and the resin, meaning that this point may be inside the thin oxide layer formed during the curing treatment. Unfortunately, precise measurement cannot be performed since the layer is very thin with respect to the resolution of the EDS detector.

3.1.4. XRD analysis

Figure 69 shows the XRD patterns of powder specimens cured at 180 °C for 2, 4 and 6 hours compared to the fresh one. Figure 70 shows a magnification of the detail of XRD patterns in the interval between 35° and 40°, showing the peaks which are not clearly visible in the full diffractogram. The patterns of cured specimens are shifted upwards to distinguish evidently them.
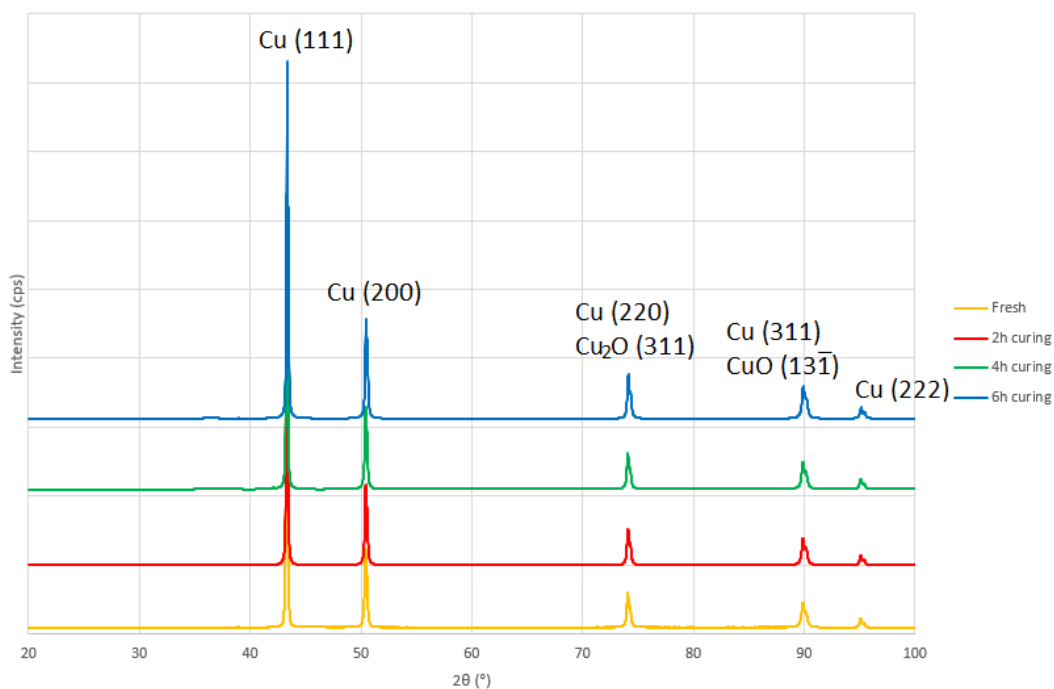
Figure 69 - XRD patterns of fresh and cured powders.
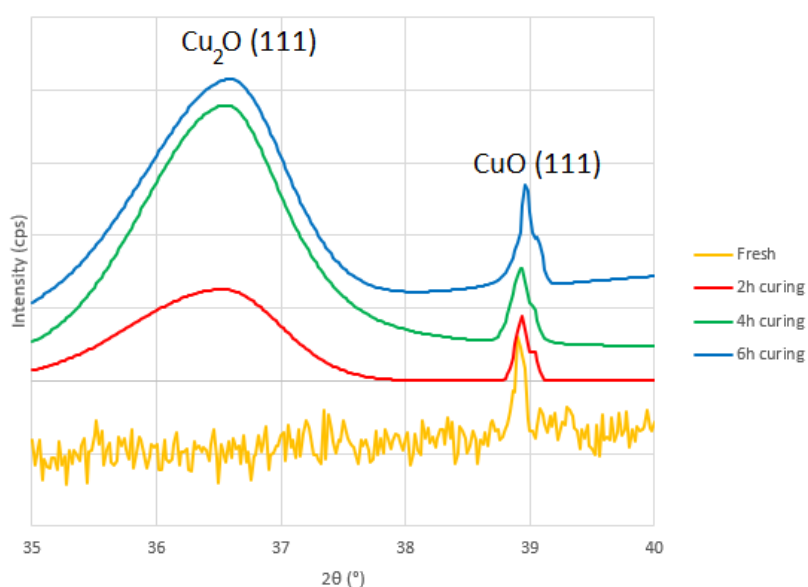
*Figure 70 - Detail of the XRD patterns in the 2θ interval between 35°
and 40° of fresh and cured copper powders.*

High intensity diffraction peaks can be observed at 43.3°, 50.4°, 74.1°, 89.9° and 95.1° and they correspond respectively to (111), (200), (220), (311) and (222) planes of the face centered cubic structure of pure copper. Two very weak peaks of cuprite Cu_2O and tenorite CuO can be seen at 36.5° and 38.9° respectively. As-received copper powder has a small peak corresponding to tenorite, meaning that this of oxide has formed due to exposition to air or during the powder production process.

In Figure 71 the diffractograms found in literature of pure copper [61], cuprite [62] and tenorite [63] are shown, in order to compare them with the obtained ones from the analysis.
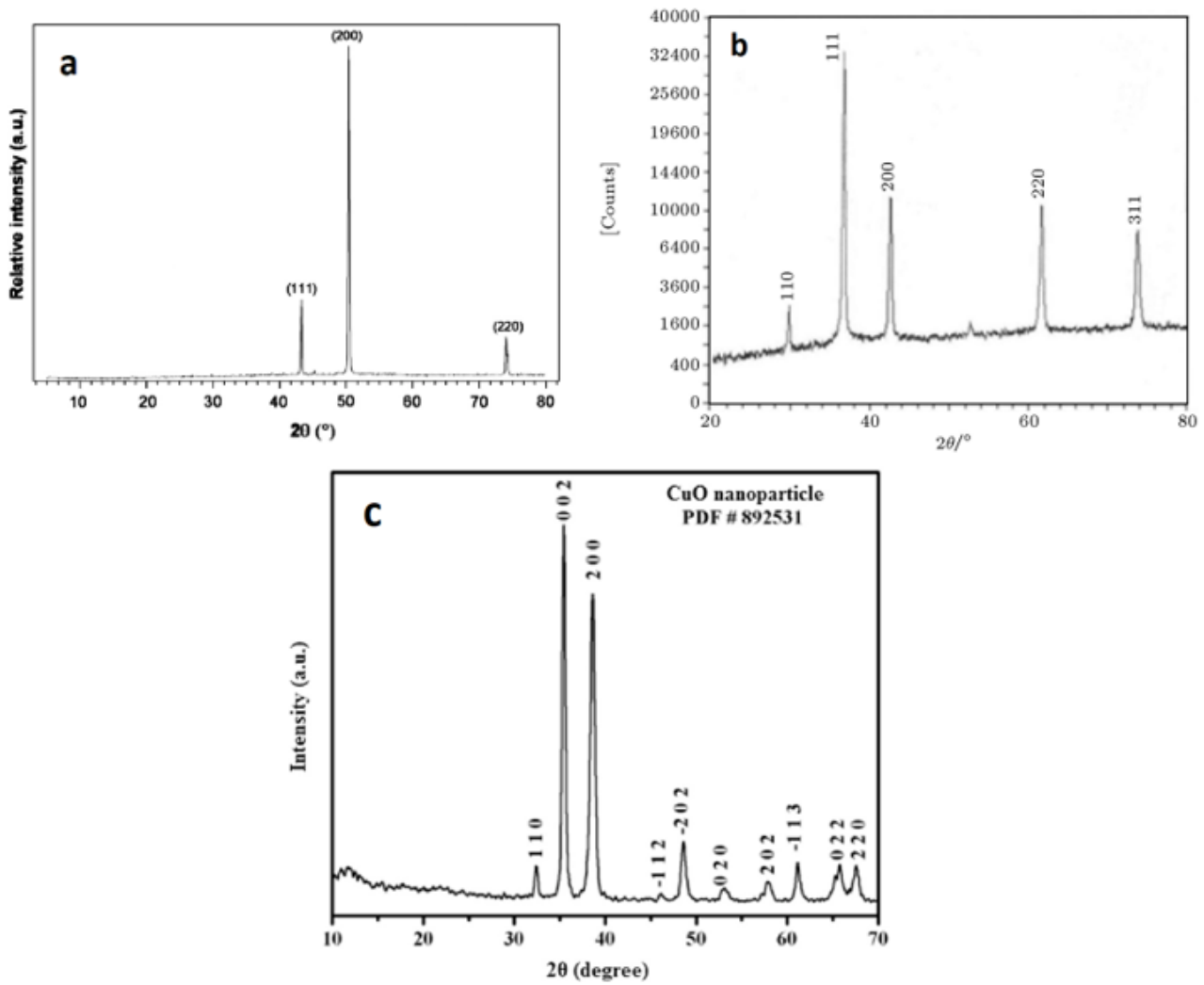
Figure 71 - XRD patterns of (a) pure Cu (from [61]), (b) Cu2O (from [62]), and (c) CuO (from [63]).

From studies found in literature [64] it is well-known that thermal oxidation of copper in air starts at 180 °C. At room temperature a spontaneous formation of a superficial layer of oxide occurs, but it is very limited because it acts as a barrier for further oxidation by limiting the diffusion of oxygen. However, at 150 °C thermal energy is enough to overcome the barrier and oxidation of copper starts, with the formation of cuprite Cu2O, following the reaction [65]:

$$2Cu + \frac{1}{2}O_2 \rightarrow Cu_2O \tag{17}$$

The formation of tenorite CuO is found only after 320 °C due to Gibb's free energy change:

$$\Delta G = \Delta H - T\Delta S \tag{18}$$

A reaction is spontaneous only if ΔG is negative. In the case of tenorite, the Gibb's free energy assumes negative values right after 320 °C, while in case of cuprite it is negative even at lower temperature.

If a temperature higher than 320 °C is maintained for long times, Cu2O transforms completely into CuO, according to the following reaction [65]:

$$2Cu_2O + O_2 \rightarrow 4CuO \tag{19}$$
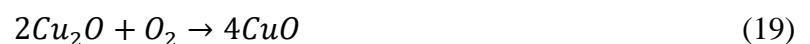
The overall phase sequence occurring in air is the following, displayed also in the Figure 72:

$$Cu \rightarrow Cu + Cu_2O \rightarrow Cu_2O \rightarrow Cu_2O + CuO \rightarrow CuO \qquad (20)$$
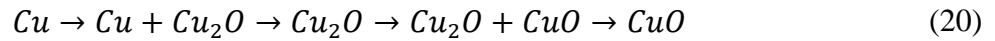
Pure Cu_2O phase is present only for a small window of temperature between 250 °C and 320 °C. For this reason, in the powder cured at 180 °C, the most present oxide phase is given by cuprite. The small presence of CuO in all samples, included the as-received powder, suggests that this oxide forms during the gas atomization process rather than during curing. This model is reliable due to the fact that only a superficial layer of the oxide has formed on powder particles [64].
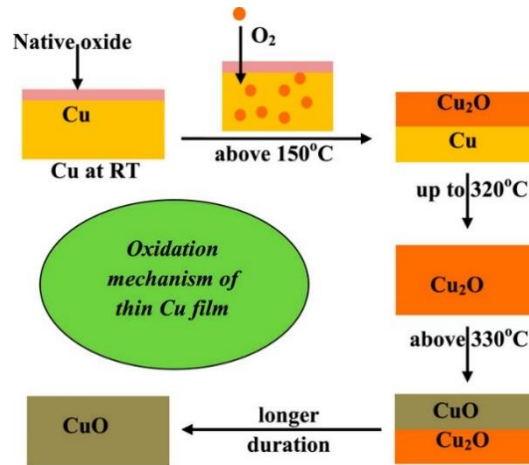
Figure 72 - Oxide growth schematics of Cu during thermal oxidation in air. From [64].

Using the Debye-Scherrer formula the average crystalline size of the oxide grains can be calculated [64]:

$$D = \frac{0.91\lambda}{\beta \cos \theta} \qquad (21)$$

where λ is the wavelength of X-ray (for Cu Kα_1 is 1.5406 Å), β is full width maximum peak, θ is the diffraction angle and D is particle diameter size. The average grain sized of (111) plane for Cu, Cu_2O and CuO are found to be 41 nm, 24 nm and 16 nm respectively, indicating a gradual decrease in crystallite grain size. The curing treatment induce the formation of cuprite alone and tenorite grains growth is not observed.

However, the peaks corresponding to copper oxides have a very low intensity in all cases, meaning that only a thin layer of oxide has formed. These results agree with the ones obtained with EDS microanalysis.

3.2. Production and characterization of green parts

3.2.1. First series of printing processes

The specimens cured for 2 hours appears to be less mechanically resistant, as confirmed by the fact that they were broken during depowdering process.

After the analysis of the powder cured for different times and the observation of the produced specimens, it was clear that a 6 hours curing was the best treatment to obtain stronger green parts, without having large amount of oxidation of copper.

3.2.2. Second series of printing processes

3.2.2.1. Green density and microstructure

In the Table 13 the volume, weight and density of green parts are reported.

Table 13 - Computed values of volume and density of green parts.

Specimen	Average volume (mm^3)	Average density (kg/m^3)	Average relative density (%)
BS90	763.37	4136.92	46.17
BS100	763.83	4466.69	49.85
BS110	774.48	4655.58	51.96

The calculated values are comparable to those reported by Miyanaji et al. [38] for similar powder characteristics and printing parameters. The green parts printed with 110% binder saturation ratio are characterized by a higher relative density, but also by a rougher surface compared to the other specimens and it was more difficult to remove the excess powder. These issues can be attributed to the oversaturation of binder, resulting in bad surface finishing and bonding of excessive powder [46] [30].
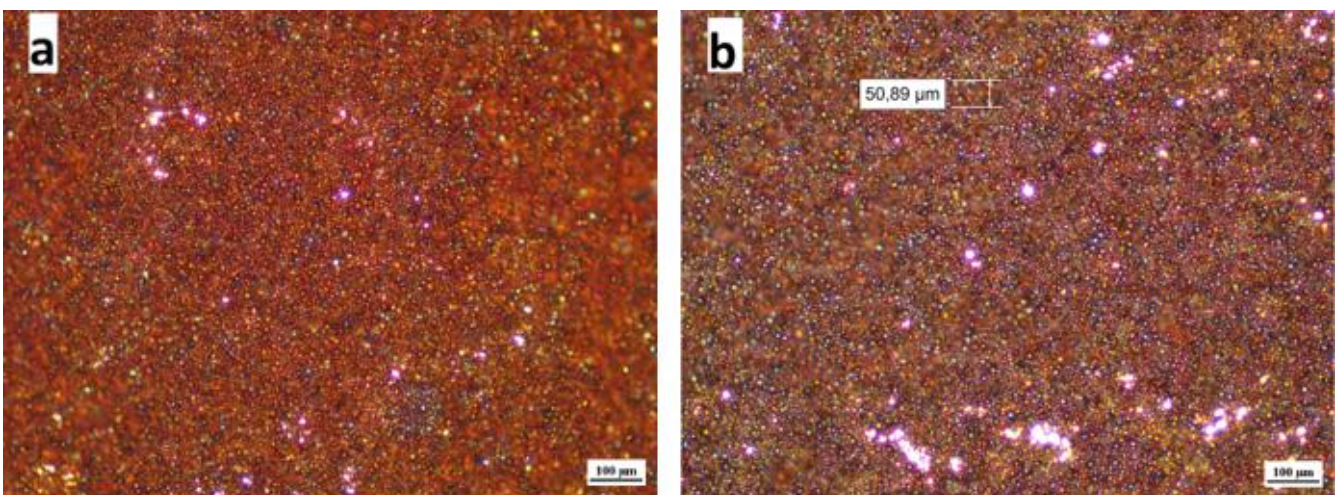
Figure 73 - Optical microscopy image of (a) top and (b) lateral surface of green specimens.

3.3. Production and characterization of brown parts

3.3.1. Debinding

After the debinding process, the specimens appear to be very dark, meaning that oxidation of copper has occurred. This is due to the presence of oxygen contamination in the chamber atmosphere and to residual oxygen in the binder. In Figure 74 a debinded specimen printed with 90% binder saturation is shown.

Figure 74 - Brown specimen after debinding treatment.

The purpose of debinding treatment is the elimination of residual polymeric binder from the part. At moderate temperature, the conventional carbothermic reaction occurs [66]:

$$2CuO + C \rightarrow Cu_2O + CO \tag{22}$$
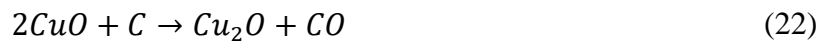
The reaction 22 cannot effectively take place at room temperature due to thermodynamic constraints, because the formation enthalpy of CO is largely reduced with the increase of temperature, and consequently lowering the reaction enthalpy. For example, the reaction enthalpy is -23 kJ at 27 °C but becomes -67 kJ at 227 °C [67].

The standard Gibbs energy (in kJ) for reaction 22 can be calculated as following [67]:

$$\Delta G_T^\circ = -50.9 + 0.0255 T \log T - 0.186 T \tag{23}$$

With roughly calculations, it can be seen that the reaction is spontaneous and can occur at the temperature at which the debinding treatment is performed.

After the formation of CO, gaseous reduction occurs [66]:

$$2CuO + CO \rightarrow Cu_2O + CO_2 \tag{24}$$

The above reaction causes rapid formation of Cu_2O and a substantial heat release.

The maximum temperature reached in this thermal treatment is 470 °C, therefore no further reactions can occur, meaning that the formed oxide cannot be reduced, leaving the specimen with a dark color, usually attributed to copper oxide.

Generally, the oxidation rate increases with increasing temperature and partial pressure of oxygen [68]. In this case, the temperature is moderate and the oxygen content is very low, since the atmosphere is almost totally argon, except for some infiltration. For this reason, the oxidation is not high.

3.3.2. DSC and TGA analysis

The curve obtained from differential scanning calorimetry represents the heat flux versus the temperature. Exothermic reactions are represented by positive peaks, while endothermic reactions correspond to negative peaks.
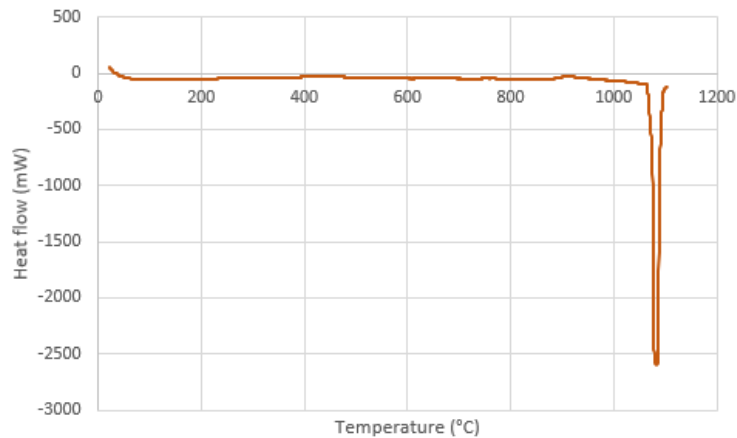
Figure 75 - DSC plot of debinded specimen.
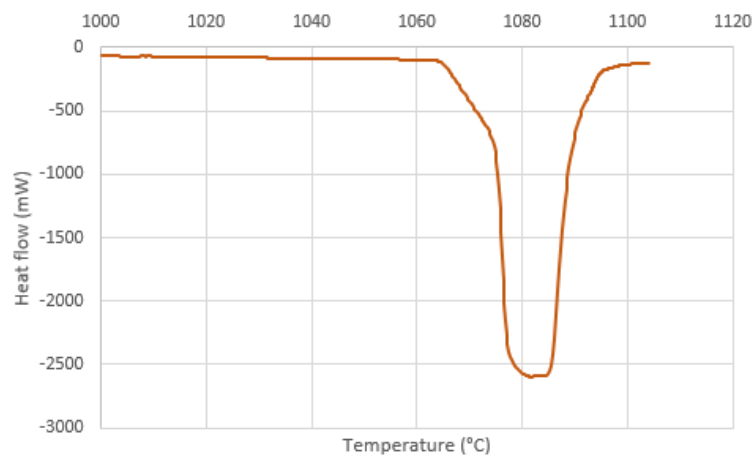
Figure 76 - Magnification of range between 1000 °C and 1100 °C of DSC plot of debinded specimen.

From Figure 75 a large negative peak can be seen at a temperature approximately of 1080 °C, corresponding to melting temperature of copper, defined as 1083 °C. A magnification of the range of temperature between 1000 °C and 1100 °C (Fig. 76) shows that the peak corresponds precisely to 1083 °C.
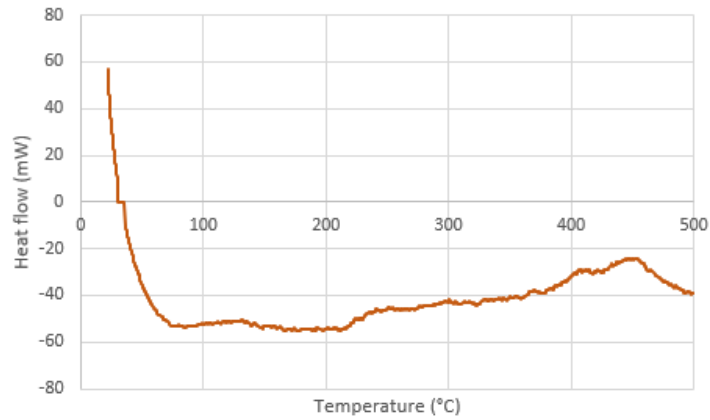
Figure 77 - Magnification of range of temperature between room temperature and 500 °C of DSC plot of debinded specimen.

Focusing on the range between room temperature and 500 °C (Fig. 77), a small exothermic peak can be identified around 450 °C.

From previous studies [66] and as previously mentioned in relation to oxidation occurred during debinding process, it is known that between 100 °C and 450 °C, there is elimination of residual binder from the specimen, followed by a reaction between carbon and copper oxide, leading to formation of CO, according to reactions:

$$2CuO + C \rightarrow Cu_2O + CO \tag{25}$$
$$2CuO + CO \rightarrow Cu_2O + CO_2 \tag{26}$$
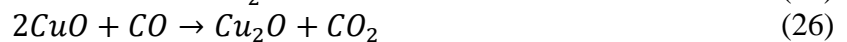
Finally, reduction of copper and formation of metal copper occur. It was found that the following exothermic reaction occurs at temperature close to 500 °C:

$$2Cu_2O + C \rightarrow 4Cu + CO_2 \tag{27}$$
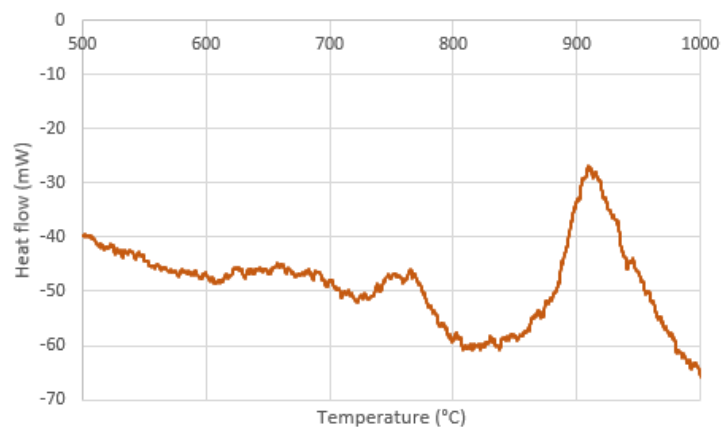
Figure 78 - Magnification of range between 500 °C and 1000 °C of DSC plot of debinded specimen.

In the range between 500 °C and 1000 °C, small fluctuations can be seen up to 900 °C, at which a significant exothermic peak was detected. This exothermic peak can be attributed to heat released during the rearrangement of particles and consequent sintering [69].

The curve obtained from thermogravimetric analysis shows the mass changes in the specimen in the temperature range of the experiment.
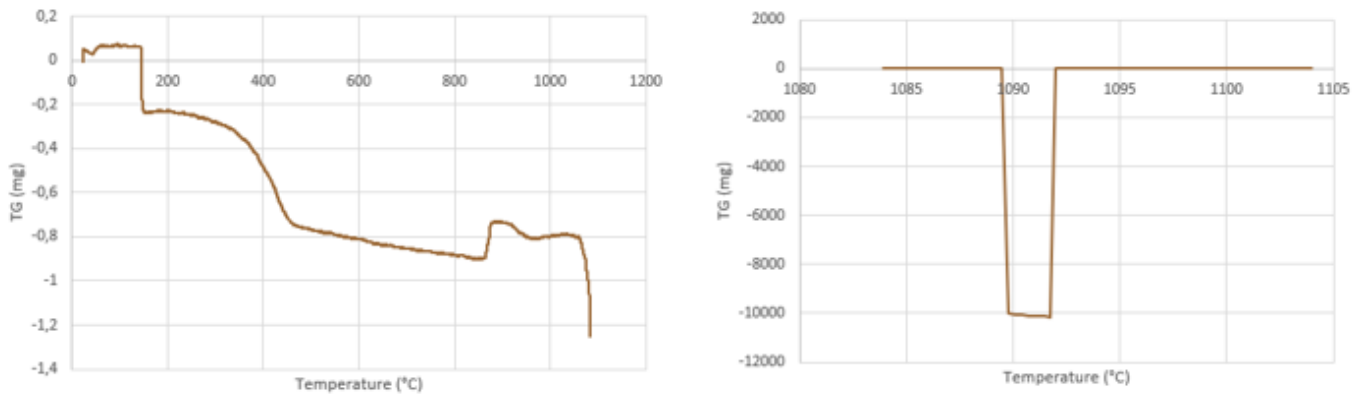
Figure 79 - Magnifications of TGA plot of debinded specimens: (left) in the range between room temperature and 1000 °C and (right) in the range between 1000 °C and 1100 °C.

At lower temperature, between room temperature and 150 °C, a mass gain occurred, probably due to an initial oxidation of the specimen. Then, the mass decreased significantly due to removal of residual binder between 200 °C and 450 °C and the reduction of oxides.
A huge mass loss occurred at approximately 1090 °C, in correspondence to the melting point of copper.

3.3.3. Dilatometry analysis

Figure 80 shows the temperature profile of the specimens in the range between room temperature and 100 °C. At the beginning of the test, the temperature increases slowly due to thermal inertia of the material.
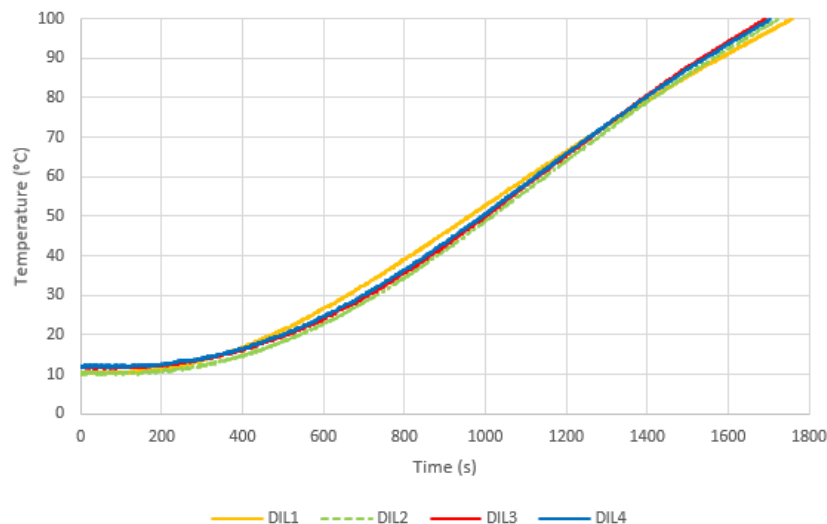
Figure 80 - Temperature profiles of dilatometry analysis of the specimens in the range between room temperature and 100 °C.

Figure 81 shows the trend of the linear coefficient of thermal expansion of the specimens as a function of temperature in the range between 50 °C and 200 °C. For the calculation of the discrete points, the raw data recorded in each dilatometry experiment were smoothed calculating the moving average with an output interval of 500 data points. Then, the values of CTE were calculated for different temperature intervals using Eq. 15 with temperature steps of 10 °C. Then, the mean CTE values were computed.

Table 14 - Mean CTE values of specimens.

Specimen	CTE (10^{-6} °C^{-1})
DIL1	13.64
DIL2	11.08
DIL3	5.69
DIL4	7.79
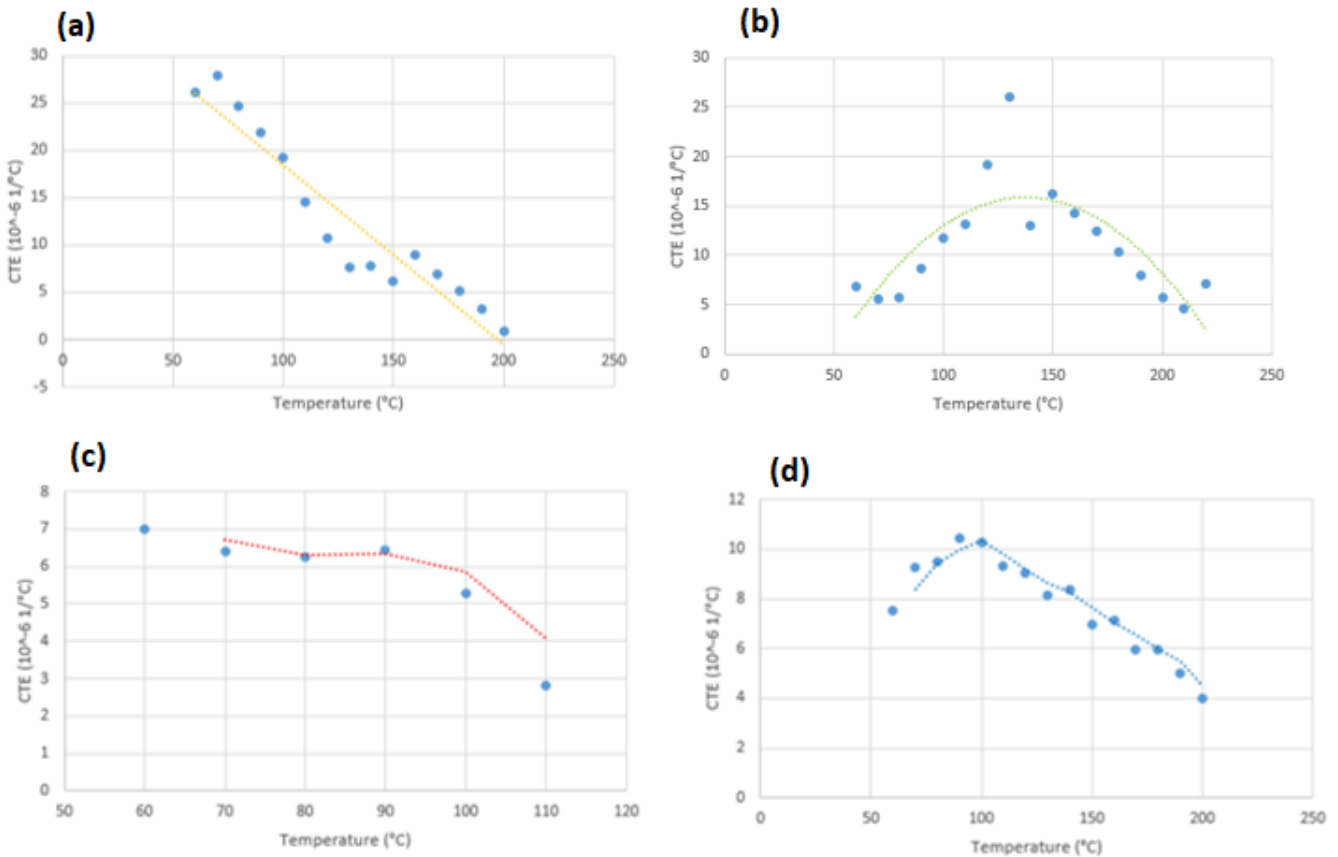
Figure 81 - CTE of (a) DIL1, (b) DIL2, (c) DIL3, and (d) DIL4.

The obtained values are similar to the ones reported in literature for pure copper [70]: in the range interested by the experiment, the linear CTE assumes values between $0.19 \cdot 10^{-6}$ °C^{-1} and $21.9 \cdot 10^{-6}$ °C^{-1}. Focusing of the CTE values corresponding to specific temperature, it can be seen that the values are larger than what is typically reported in literature and this can be attributed to the large temperature range covered by dilatometry experiment, as also reported by Wheat et al. [71], who performed dilatometry experiments to study the sintering behavior of pure titanium printed via binder jetting.

The rule of mixture can be used to determine the coefficient of thermal expansion (α_{eff}) of a porous component [72]. A binder jetted part consists of a copper metal matrix and a volume occupied by gas after binder elimination. The α_{eff} can be written as:

$$\alpha_{eff} = \alpha_1 V_1 + \alpha_2(1 - V_1) \tag{28}$$

where V_i indicated the volume fraction of each material and α_i is the corresponding coefficient of thermal expansion. In this case, the coefficient of thermal expansion α_1 is the one of the copper matrix, which corresponds to $17 \cdot 10^{-6}\,°C^{-1}$, a common value that can be found in literature. The specimens have a fractional density of around 50% with respect to bulk copper, and the remaining volume is gas with $\alpha_2 = 0$. Therefore, the CTE of binder jetted parts can be estimated as:

$$\alpha_{BJ} = \alpha_{Cu} V_{Cu} = 17 \cdot 10^{-6}°C^{-1} \cdot 0.5 = 8.5 \cdot 10^{-6}°C^{-1} \tag{29}$$

The theoretical value is similar to the computed ones; thus, it can be assumed that calculations are correct.

The dilatometric curves were plotted with the deformation as a function of temperature. From the dilatometric curve of the specimen treated in argon up to 1050 °C, DIL1 (Fig. 82, left), it can be seen the first thermal event occurs in the range between 350 °C and 400 °C, which likely corresponds to the pyrolysis of the residual binder, since 450 °C is the typical temperature used for isothermal holding for debinding process. The second thermal event occurs in the range between 550 °C and 600 °C, which may be associated with the beginning of neck formation between contacting powder particles. At 700 °C, the curves assumes negative values of deformation, indicating the start of the shrinkage and densification process. After 900 °C, a significant boost of shrinkage occurs due to volume diffusion. The final value of linear shrinkage is -4.28%, very low with respect to the desired one.

Even in case of the specimen treated in vacuum up to 1050 °C, DIL2 (Fig. 82, right), the first thermal event occurs around 350-400 °C, where the residual binder burns off. Neck formation happens at 600 °C and the curve assumes negative values at 750 °C, after which shrinkage occurs. The shrinkage increases drastically after 900 °C, reaching the final value of -10.22%, significantly higher than the value obtained in argon.
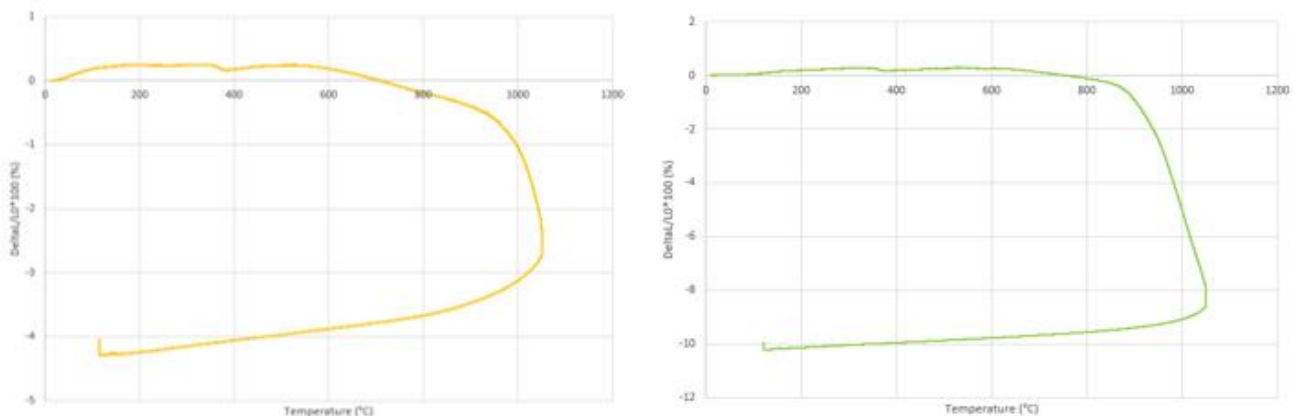
Figure 82 - Dilatometric curves of (left) DIL1 and (right) DIL2.

The other two specimens were treated in vacuum up to 900 °C, but for a different holding time. In both cases the thermal events are the same: in the range between 350 °C and 400 °C the residual binder burns off, after 600 °C neck formation starts and densification occurs after 800 °C. The specimen kept at 900 °C for only 1 hour has a final shrinkage value of -6.81%, while the one kept for 3 hours reached a final linear shrinkage of -9.9%. This shows that a longer time maintenance at the peak temperature is required.
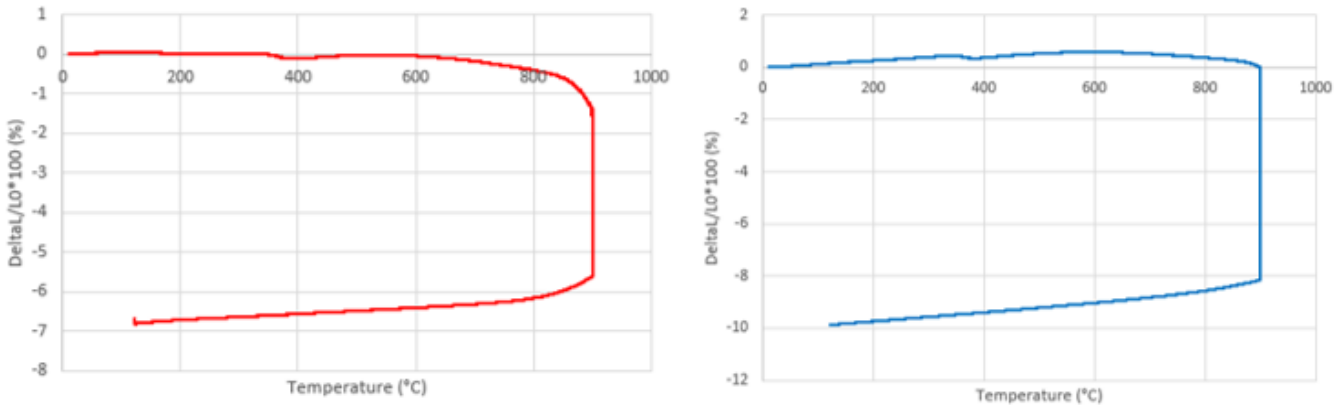
Figure 83 - Dilatometric curves of (left) DIL3 and (right) DIL4.

In Table 15 the linear shrinkages of the specimens are reported.

Table 15 - Linear shrinkage values of specimens after dilatometry analysis.

Specimen	Linear shrinkage (%)
DIL1	-4.28
DIL2	-10.22
DIL3	-6.81
DIL4	-9.9

The shrinkage rate dependence on temperature was calculated:

$$-\frac{d\left(\Delta L/L_0\right)}{dt} = -\frac{\Delta L_2/L_0 - \Delta L_1/L_0}{t_2 - t_1} \tag{30}$$

The negative sign is included to obtain positive values for shrinkage rate.
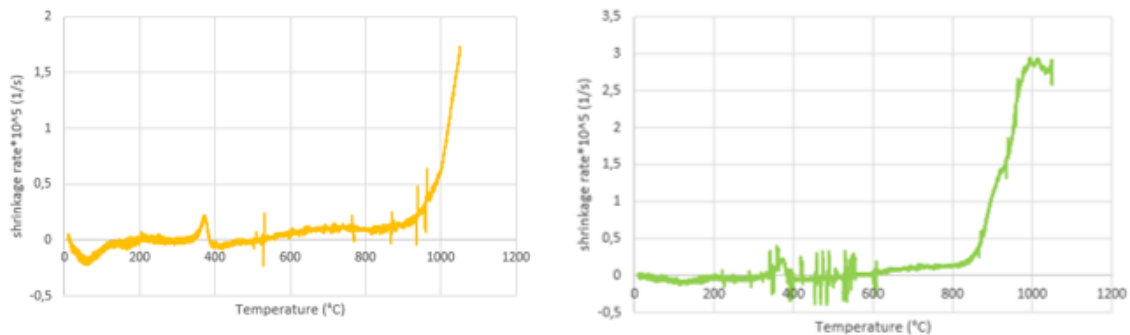
Figure 84 - Shrinkage rates of (left) DIL1 and (right) DIL2.

In Figure 84 the shrinkage rates of DIL1 and DIL2 are shown.

In both cases, the shrinkage rate is negative up to 200 °C, indicating a starting thermal expansion of the specimens. Then, shrinkage rate becomes slightly positive, reaching a peak around 400 °C due to pyrolysis of residual binder. After 600 °C, the rate increases weakly due to particle rearrangement and initial necking, and increases radically after 900 °C, meaning that a stronger densification occurs (intermediate/final stage sintering). The main differences between the specimens treated in two different atmospheres are the amount of linear shrinkage and, therefore, the shrinkage rate: the part treated in vacuum is characterized by larger densification. This is likely due to gas removal which allows to fully densify the material without formation of pressurized closed spherical pores.
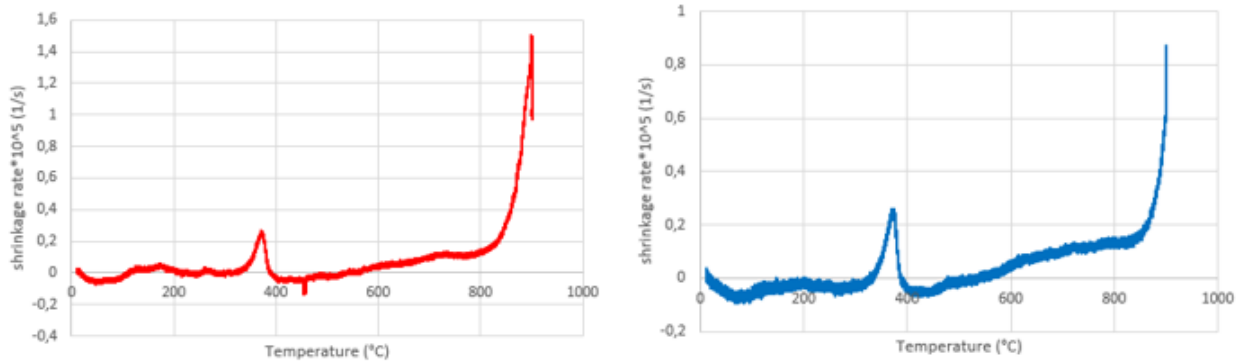
Figure 85 - Shrinkage rates of (left) DIL3 and (right) DIL4.

In Figure 85 the shrinkage rates of DIL3 and DIL4 are shown.

Both specimens were treated in vacuum up to 900 °C, but the holding time was different. The thermal events of the part are the same as DIL1 and DIL2 but the shrinkage is not as much of the one indicated by the previous analysis, because the major densification occurs after 900 °C.

In Table 16 the maximum shrinkage rates for each sample are displayed.

Table 16 - Maximum shrinkage rates of specimens during dilatometry analysis.

Specimen	Maximum shrinkage rate (10^5 1/s)	Temperature (°C)
DIL1	1.73	1050
DIL2	2.94	995
DIL3	1.48	899
DIL4	0.93	899

After the dilatometry analysis, the specimens appear to be lighter (Fig. 86), indicating that reduction of oxides and removal of binder have occurred.
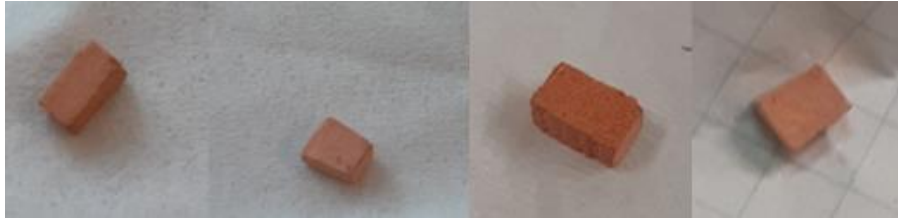
Figure 86 - Brown specimens after dilatometry analysis.

Previous studies [64] affirm that copper oxide can be completely reduced to metallic copper by out gassing under ultra-high vacuum condition (10^{-9} Torr) at a temperature higher than 700 °C.

Lee et al. [73] studied the reduction mechanism of copper when vacuum annealing was performed on partially-oxidized and fully-oxidized copper films and their evaluations can be applied to this dilatometric study to explain the reason why the specimens are no more oxidized.
The authors performed an X-ray photoelectron spectroscopy (XPS) to evaluate the composition of the specimens.
After 300 °C, the peak corresponding to tenorite (CuO) completely disappears, like mentioned before and after 400 °C the peak associated with cuprite (Cu_2O) is no longer detectable. At temperatures higher than 400 °C, the signal of metallic copper becomes dominant.
The spectrum of carbon is very interesting, since before annealing two kinds of carbon were identified: graphite and carbonate. The signal associated with carbonate decreases steadily to zero between 80 and 300 °C, while graphite does not change up to 200 °C and increases up to the maximum value, corresponding to 400 °C, due to carbon diffusion from the bulk.
Carbon may be involved with copper reduction. First, superficial CuO decomposes into Cu_2O according to the following reaction:

$$2CuO + 2Cu \rightarrow 2Cu_2O \tag{31}$$

The reaction 31 is spontaneous, since the difference of free energy is negative, for example ΔG at 380 K is -42.8 kJ/mol.
Then, oxygen atoms from copper oxide probably recombine with carbon on the surface, forming gaseous CO and CO_2 which are desorbed into vacuum. The chemical reaction occurring can be described as following, like previously mentioned in the discussion about differential scanning calorimetry:

$$2Cu_2O + C \rightarrow 4Cu + CO_2 \tag{32}$$

This explanation is valid even in the case of this work, since the carbon is given by the residual binder not completely burnt off with the debinding process.

The relative density of the specimens was calculated as mentioned before and the results are displayed in Table 17.

Specimen	Average volume (cm^3)	Average density (g/cm^3)	Average relative density (%)
DIL1	0.016	8.22	92.16
DIL2	0.034	7.34	82.31
DIL3	0.033	6.54	73.28
DIL4	0.041	6.18	69.24

The obtained values are clearly not very reliable due to the fact that the analyzed specimens were extremely small and open porosities were present. These open pores absorb liquid when the samples are immersed, altering the measurement of density, as can be seen in case of DIL1: it showed a significant small shrinkage compared to the other specimens, but the value of relative density is higher.

For this reason, the computed values reliability is limited.

3.3.4. Optical analysis of dilatometry samples

Figure 87 shows the microstructure of the specimen treated in argon up to 1050 °C (DIL1). A lack of sintering can be observed in some regions of the sample and it may be caused by insufficient holding time at 1050 °C. This justifies the low value of linear shrinkage and the fact that the computed value of density is not reliable due to high porosity and the small volume of the sample.
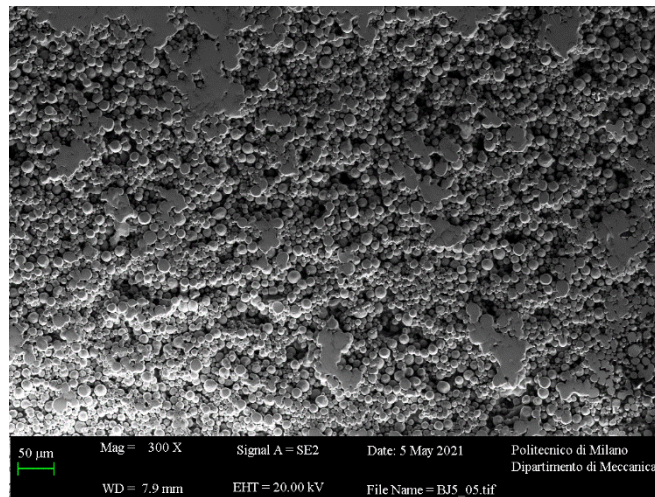
Figure 87 - SEM image showing microstructure of DIL1.
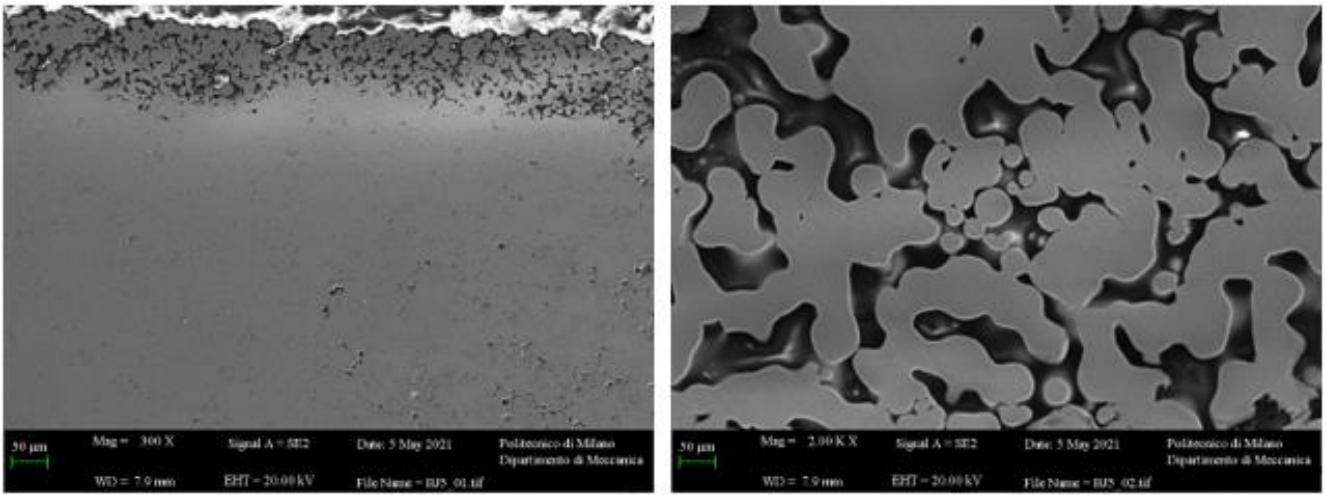
Figure 88 - SEM images showing (left) the edge of the specimen and (right) the open porosity filled with resin.

In Figure 88 (left) a focus of the edge is displayed. ImageJ software was used to measure the length of this porous edge: the average value of distance was approximately 100 µm, indicating the fact that the part had a poor surface finishing. This open porosity is disadvantageous for the specimen because, as can be seen from Figure 88 (right), they were completely filled by the resin.

From the EDS analysis performed on the area, the content of copper were 99.5%, indicating an almost complete oxide reduction during the dilatometry experiment.
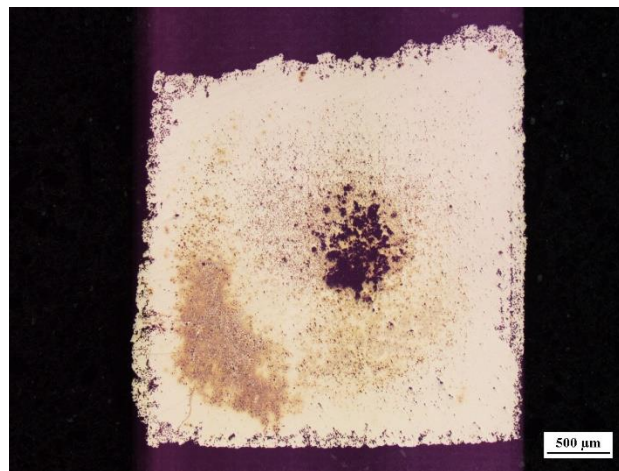
Figure 89 - Optical image of specimen DIL2.

The specimen treated in vacuum up to 1050 °C (DIL2) is characterized by a large porosity at the core (Fig. 89). This region is constituted by particles which did not have time to sinter likely due to the insufficient holding time at peak temperature and to the internal thermal gradient which allowed extensive diffusive mechanisms only at the peripheral regions of the sample. The SEM micrographs (Fig. 90) confirm the insufficient sintering in the central part of the sample and show pores full of resin at the edges, like the previous specimen. EDS analysis confirmed the reduction of copper oxide, being the weight percentage of oxygen 0.35%.
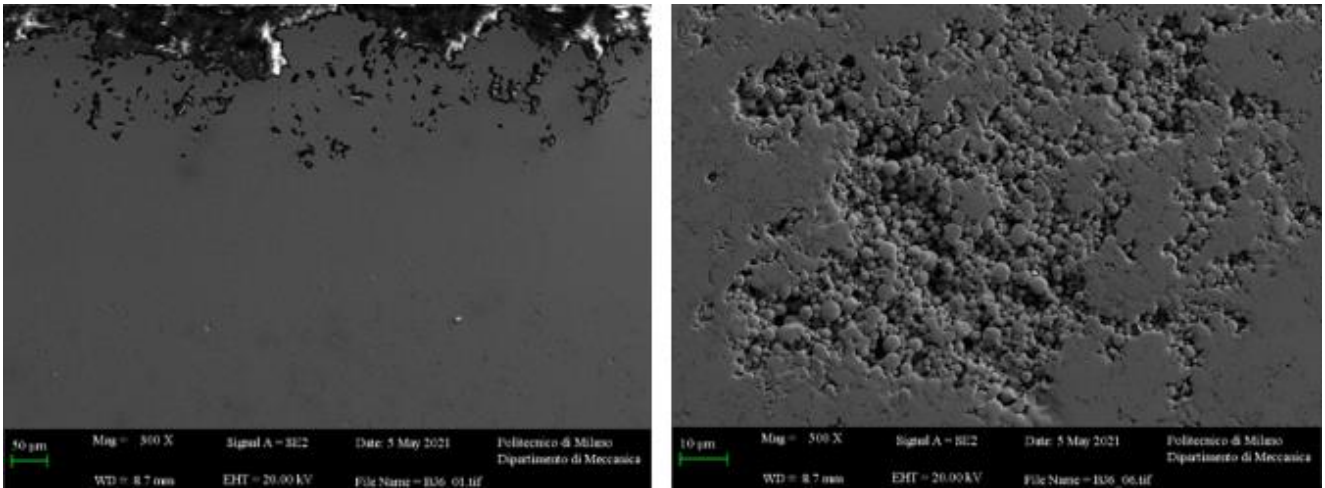
Figure 90 - SEM micrographs of specimen DIL2: (left) the edge and (right) central region.
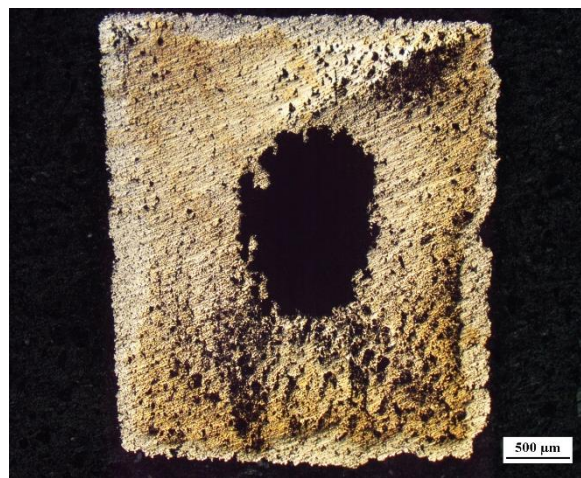
Figure 91 - Optical picture of specimen DIL3.

From the picture taken with optical microscope (Fig. 91) of the specimen treated up to 900 °C and with a holding time of 1 hour (DIL3), a huge central hole can be observed. Larger magnification and SEM micrographs (Fig. 92) reveal the presence of unsintered particles and other contaminants retained by the pore. This is an indication of the insufficient temperature, that did not allow to achieve final stage sintering with the removal of the internal porosity.
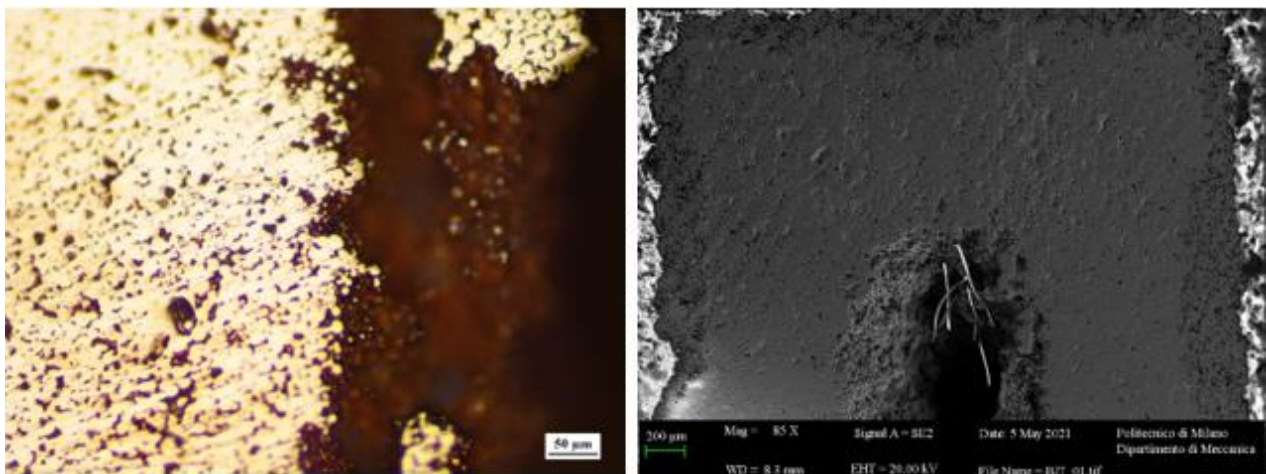
Figure 92 - Optical picture (left) and SEM micrograph (right) of specimen DIL3.

The last specimen, treated in vacuum up to 900 °C and with a holding time of 3 hours (DIL4), displayed an incomplete sintering process with extended residual porosity. It can be noticed in Fig. 93 that pores seem to be particularly concentrated along parallel lines corresponding to the layer-by-layer deposition of the printing process.
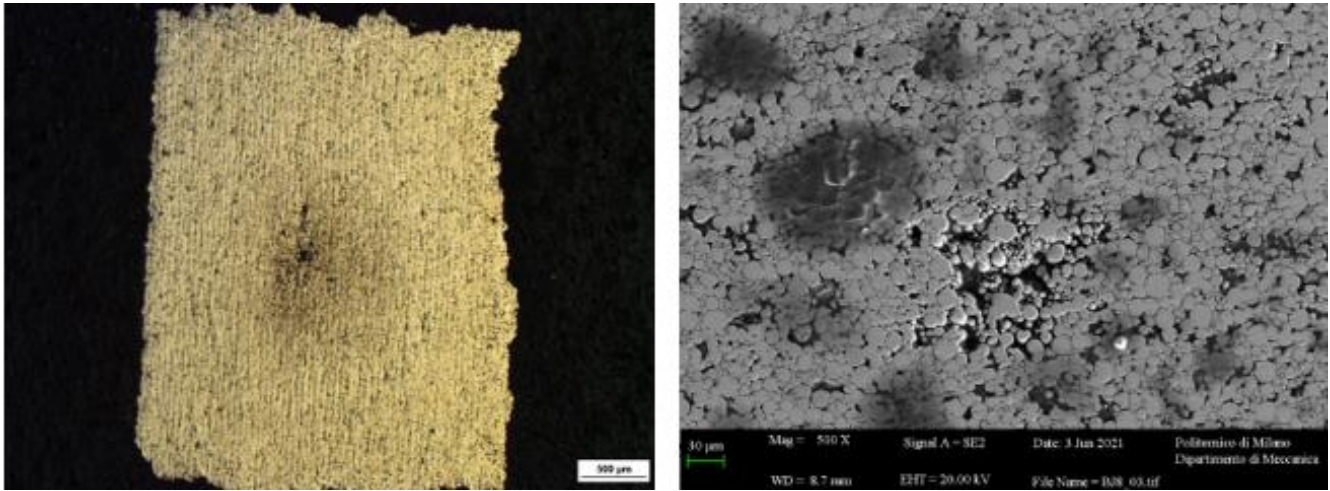
Figure 93 - Optical picture (left) and SEM micrograph on the central porosity (right) of specimen DIL4.
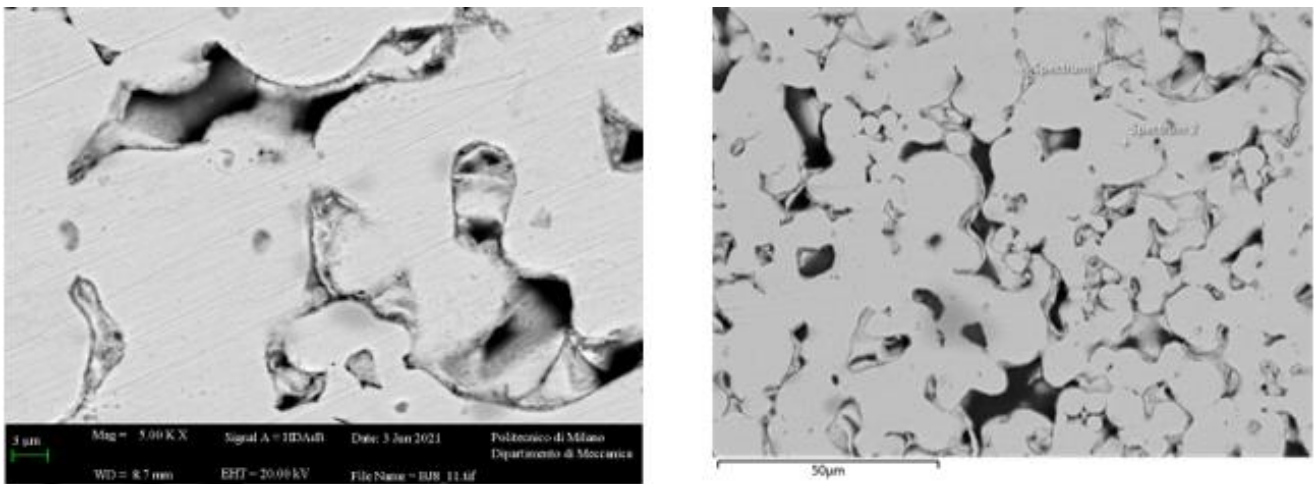
Figure 94 - SEM magnifications of the porosities of specimen DIL4.

From the analysis performed after the dilatometry analysis on the brown parts, some assumptions about the sintering treatment can be done.
First of all, 900 °C is not a sufficient to obtain adequate densification of the parts, even with a holding time of 3 hours, because the maximum shrinkage occurs around 950-1000 °C.
The temperature should be higher than 950 °C and a holding time is required because the specimen treated up to 1050 °C with no maintenance were characterized by regions which did not undergo sintering.

Concerning the atmosphere, vacuum guarantees higher linear shrinkage with respect to inert gases. This may be due to the fact that in vacuum gases are removed from the pores, allowing a better diffusion on material, while in argon gases remain trapped inside some pores, lowering the value of final density.

Juan [74] studied the effects of sintering atmosphere on the final density of 316L stainless steel binder jetted parts. He discovered that performing sintering in vacuum led to a 10% higher density compared to sintering in argon at the same temperature. This is a confirmation of the fact that vacuum allows degassing of pores, leading to a complete densification because no gas remained trapped inside, while in case of argon, residual porosity is stabilized by pore pressurization, slowing the densification process and promoting coalescence of pores.

3.4. Production and characterization of sintered parts

3.4.1. Thermal treatment in hydrogen atmosphere

After the chosen thermal treatment, the parts appear to be lighter, meaning that reduction of copper oxide has occurred.

The relative density and shrinkage were calculated and the obtained results are different from the expected values.

Table 18 - Computed values of volume and density of sintered parts.

Specimen	Average volume (mm^3)	Average density (kg/m^3)	Average relative density (%)
BS90	715.67	4296.88	47.96
BS100	716.99	4687.09	52.31
BS110	732.24	4780.67	53.36

Table 19 - Computed values of volumetric shrinkage of sintered parts.

Specimen	Difference in volume (mm^3)	Difference in relative density (%)	Shrinkage (%)
BS90	-47.69	+1.78	6.25
BS100	-46.83	+2.46	6.13
BS110	-39.24	+1.39	5.09

It is clear that suitable densification did not occur during the thermal treatment, as the density increased by less than 3% compared to the green density.

Table 20 - Linear shrinkage of sintered parts.

Specimen	Shrinkage (%)		
	X	Y	Z
BS90	0.33	2.07	3.98
BS100	1.97	1.85	2.44
BS110	1.08	1.75	2.35

Shrinkage in the lateral (X and Y) and build (Z) directions is reported in the Table 20. It is a confirmation of the results reported in previous studies, according to which the shrinkage of binder

jetted parts is larger in the build direction rather than in the lateral directions [38]. This can be attributed to the anisotropic distribution of porosity in green parts, since particles are not consolidated across layers as well as they are within a layer due to limited binder diffusion in the powder bed [37].

After a visual inspection, the samples look still in the green state and this is confirmed by the optical analysis of the specimens. Figure 95 shows the optical microscopy images of the lateral surface of sintered binder jetted specimens. Individual particles can still be distinguished, meaning that the thermal treatment was not sufficient to induce diffusion and necking between contacting particles. The only difference between these pictures and the micrograph of green samples is the fact that powder layer can no longer be recognized, indicating that particle rearrangement occurred during the treatment.
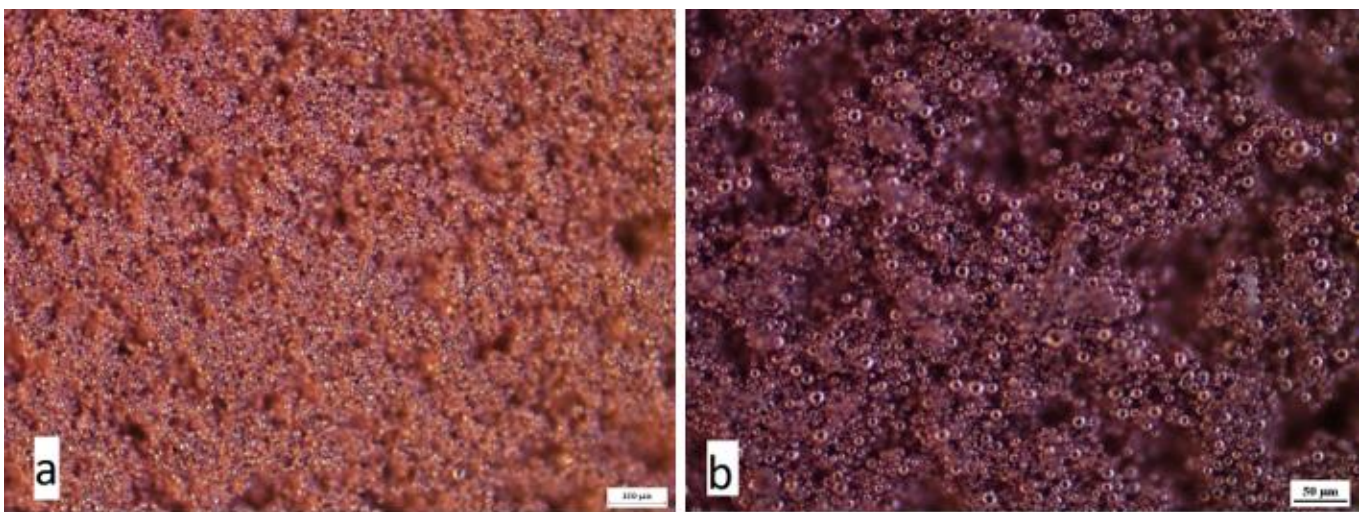
Figure 95 - Optical microscopy images of lateral surface of sintered specimens with (a) 25x and (b) 200x magnification.
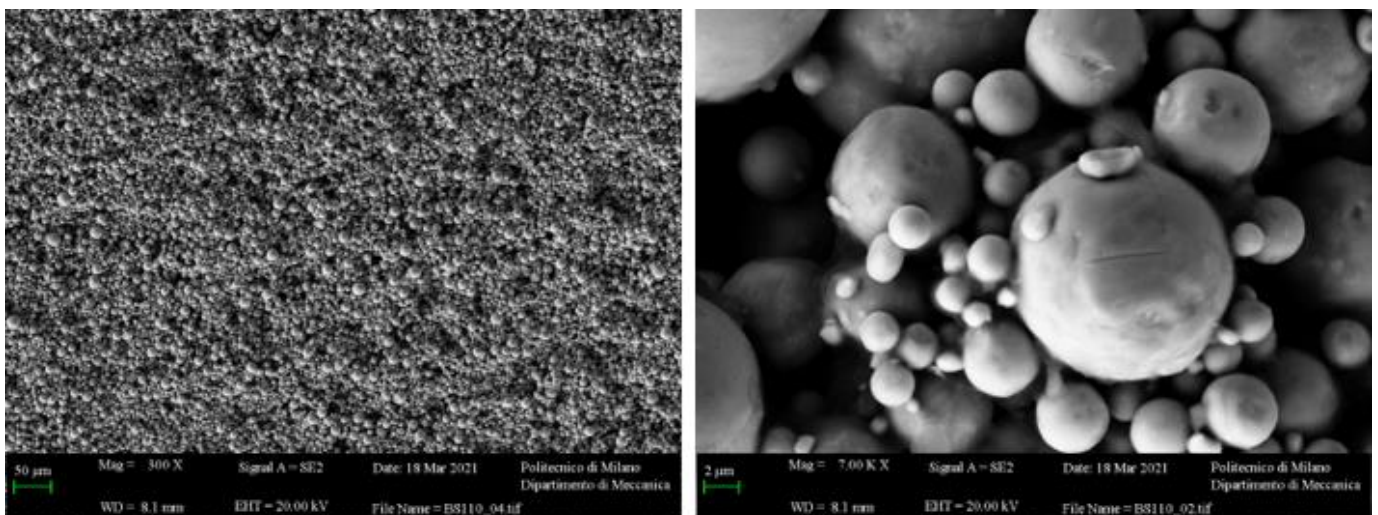
Figure 96 - SEM micrographs of sintered specimens.

Figure 96 shows the SEM micrographs of a "sintered" binder jetting specimen. Individual particles can be detected and amorphous material can be observed between particles and on the surface of bigger particles in the image with higher magnification. This amorphous phase is residual polymer which was not completely removed during the debinding step. This is confirmed by the high carbon content detected by EDS analysis reported in Table 21. The carbon content increases with the increasing of binder saturation, indicating that it could come not only from the resin and other contaminants, but also from the polymer.

Small amounts of aluminum and silicon were detected, coming from polymeric binder and grinding papers, respectively, due to the fact that the samples were not fully sintered, so they tended to absorb moisture and contaminants.

Table 21 - Results of EDS analysis performed on sintered specimens.

Specimen	Cu (weight%)	O (weight%)	C (weight%)	Al (weight%)	Si (weight%)
BS90	96.8	0.3	2.9	-	-
BS100	93.5	0.7	5.4	0.3	-
BS110	89.2	1.3	7.7	0.3	1.5

The sintered specimens have a lower oxygen content (see Table 21) compared to the one detected in the cured powder, indicating that the reducing atmosphere employed in the sintered process reduced the copper oxides formed during curing in air.

Reduction of copper oxide in the presence of hydrogen is an expected reaction, that occurs even at moderate temperature due to the fact that it is autocatalytic, with copper as catalyst [75] and takes place at the copper-copper oxide interface [76].

Cuprite is the most present oxidized phase found in cured powders, as can be seen from XRD analysis, and it is reported [77] that the reduction of Cu_2O is achieved above 250 °C, described by the following reaction:

$$Cu_2O_{(s)} \rightarrow 2Cu_{(s)} + \frac{1}{2}O_{2(g)} \tag{33}$$

The control of oxygen partial pressure is achieved by the reaction of oxygen with hydrogen, leading to the formation of water:

$$H_{2(g)} + \frac{1}{2}O_{2(g)} \leftrightarrow H_2O_{(g)} \tag{34}$$

The overall chemical reaction can be written as:

$$CuO_{(s)} + H_{2(g)} \rightarrow Cu_{(s)} + H_2O_{(g)} \tag{35}$$
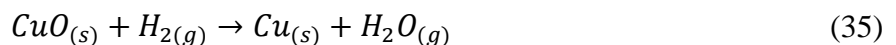
The results obtained from the measurement of the density and microscopic analysis suggest that the performed sintering treatment is not sufficient to obtain adequate densification level, for this reason the temperature should be increased. This also confirms the results obtained from dilatometry analysis.

3.4.2. Thermal treatment in inert atmosphere

After the thermal treatment, the specimens appear to be dark, indicating that oxidation occurred. However, when they were embedded in resin, in the samples treated in the graphite crucible the oxide crust was not noticeable anymore, as it was very thin. The reason of the formation of the oxide can be attributed to the fact that the alumina tube is not perfectly closed and some oxygen infiltrates in the chamber.

In Figure 98, some images of the specimen treated in argon without graphite are shown.
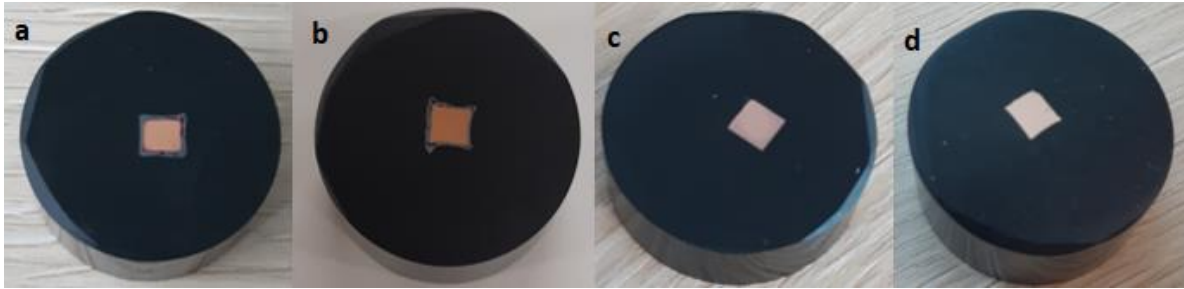
Figure 97 - Resin embedded specimens after thermal treatment.
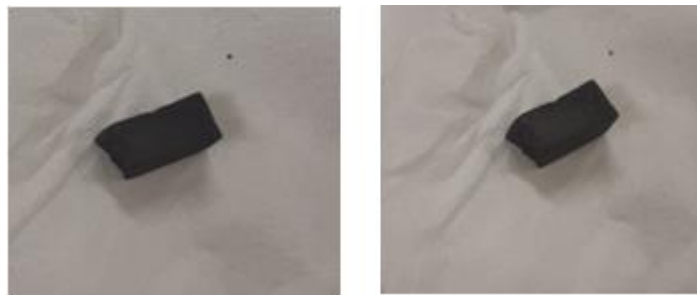
Figure 98 - Images of specimens treated in argon without graphite.

 The thickness of the oxide crust was measured with ImageJ software and it was found that the average value of thickness is approximately 500 μm. Moreover, a lot or pores are present.
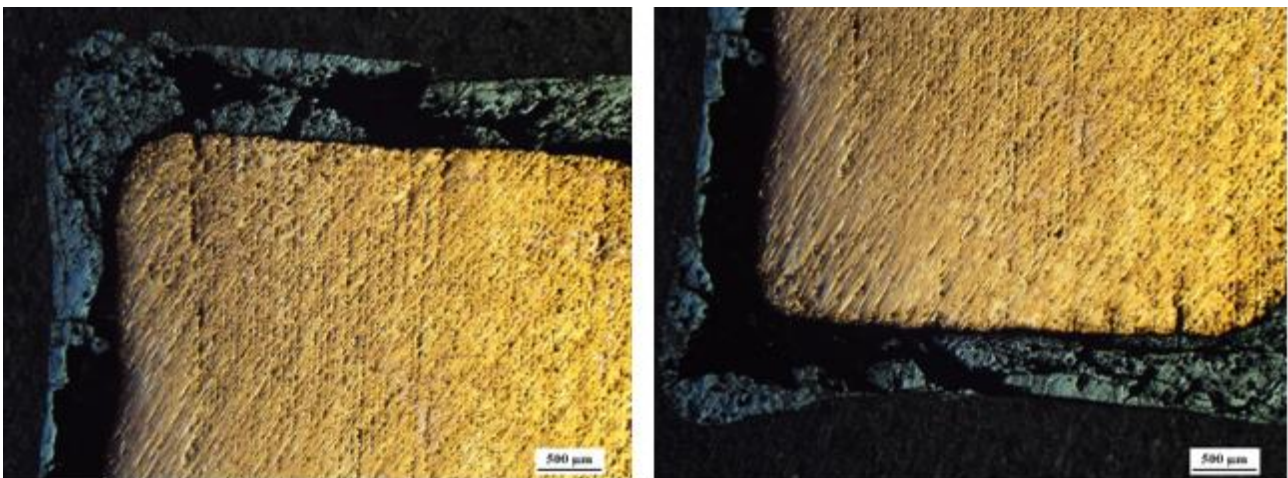
Figure 99 - Optical images of showing the dark crust of oxide.

The specimen was observed with SEM and analyzed with EDS.
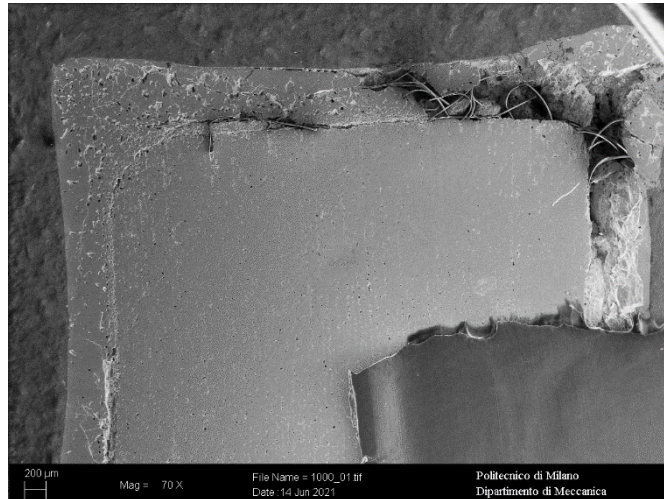
Figure 100 - SEM image showing impurities present in the pores in the oxide crust.
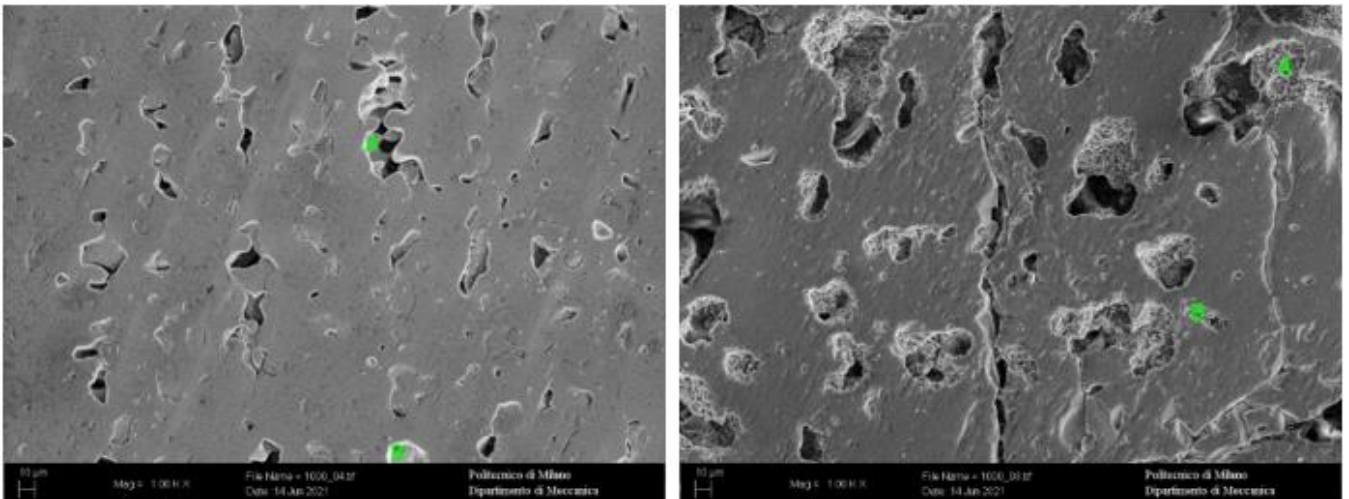
Figure 101 - SEM micrographs of (left) inner region and (right) oxidized crust.

Figure 101 (left) shows an image of the inner region of the specimen and in Figure 101 (right) a magnification of the oxidized crust is shown. The results of EDS analysis are reported in Tables 22 and 23.

Table 22 - Results of EDS analysis performed on the inner region of the specimen.

Site of analysis	Cu (%wt)	O (%wt)	C (%wt)
A	98.97	0.3	0.73
B	93.24	0.68	6.09
Matrix	91.27	-	8.73

Site of analysis	Cu (%wt)	O (%wt)	C (%wt)
A	84.18	5.03	10.8
B	95.08	1.22	3.71
Matrix	85.31	8.04	6.65

It is clear how the crust has a very high percentage of oxygen, confirming the presence of copper oxide.

The matrix of the inner region of the specimen is basically only copper, with some carbon which probably comes from resin or other impurities, like the diamond paste used for polishing.

In Figure 102 some photos taken with optical microscope of the specimen G1, in presence of graphite, are shown.
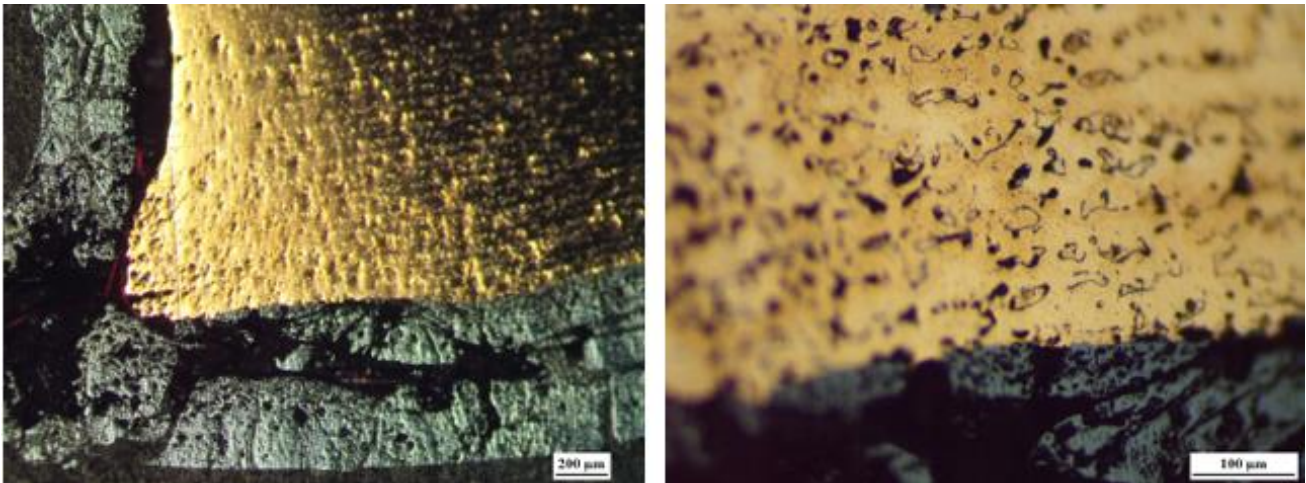
Figure 102 - Optical images of specimen G1.

The black crust is still present, but in this case, it measured approximately 300 μm. Also, this sample has less and smaller pores.

Three different EDS analysis were performed on G1: the first one on the inner region (Fig. 103 (a)), the most regular and less porous, the second one in an irregular and porous region close to the edge (Fig. 103 (b)) and the last one on the dark crust (Fig. 103 (c)).

Figure 103 - SEM micrographs of specimen G1: (a) inner region, (b) porous region close to the edge, and (c) dark crust.

The results of EDS analysis are reported in the tables below.

Table 24 - Results of EDS analysis performed on the inner region of the specimen G1.

Site of analysis	Cu (%wt)	O (%wt)	C (%wt)	Cl (%wt)
A	80.93	3.16	15.04	0.87
B	90.09	-	9.91	-
Matrix	100	-	-	-

Table 25 - Results of EDS analysis performed on the porous region of the specimen G1.

Site of analysis	Cu (%wt)	O (%wt)	C (%wt)	Cl (%wt)	Ca (%wt)
A	53.55	8.14	38.31	-	-
B	66.27	7.33	24.17	1.25	0.99
C	85.05	9.52	5.43	-	-
Matrix	100	-	-	-	-

Site of analysis	Cu (%wt)	O (%wt)	C (%wt)
A	91.15	8.85	-
B	83.03	9.83	7.14
C	88.75	11.25	-
Matrix	92.63	7.37	-

The inner region of G1 is fully copper (100%), except for some impurities in the pores. The edges are characterized by irregularities and contain more pores compared to the inner region, in which contaminations remain trapped, like Ca, coming from the resin, and Cl.

Even in this specimen, the dark crust has a very high percentage of oxygen, indicating the presence of copper oxide.

In the Figure 104 some pictures taken with optical microscope of the specimen G2, the one treated in argon inside the graphite crucible, are shown.
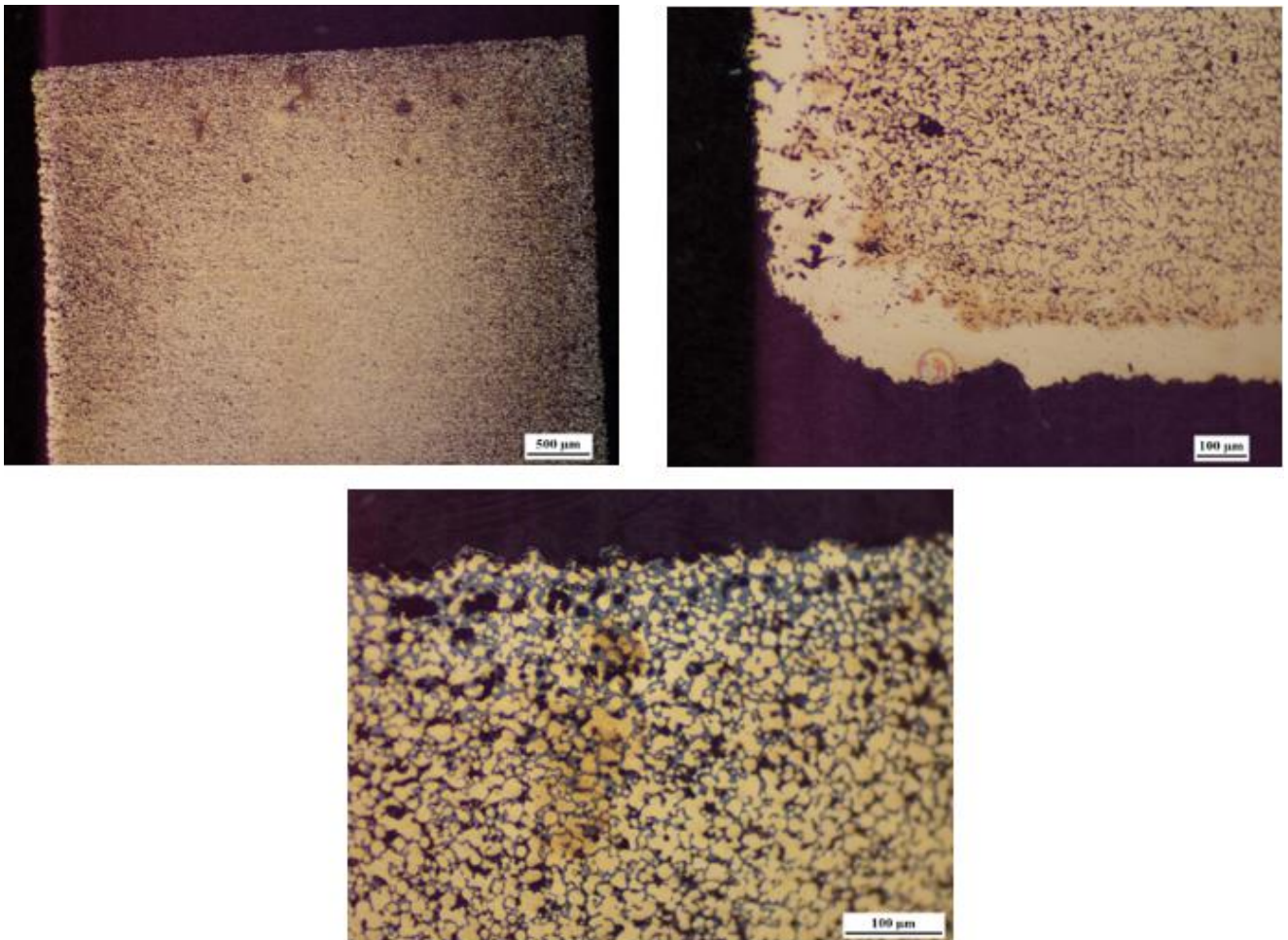
Figure 104 - Optical images of specimen G2.

The black crust cannot be seen anymore, indicating a good reduction of copper, but the edges of the specimen are irregular and contain a lot of pores.
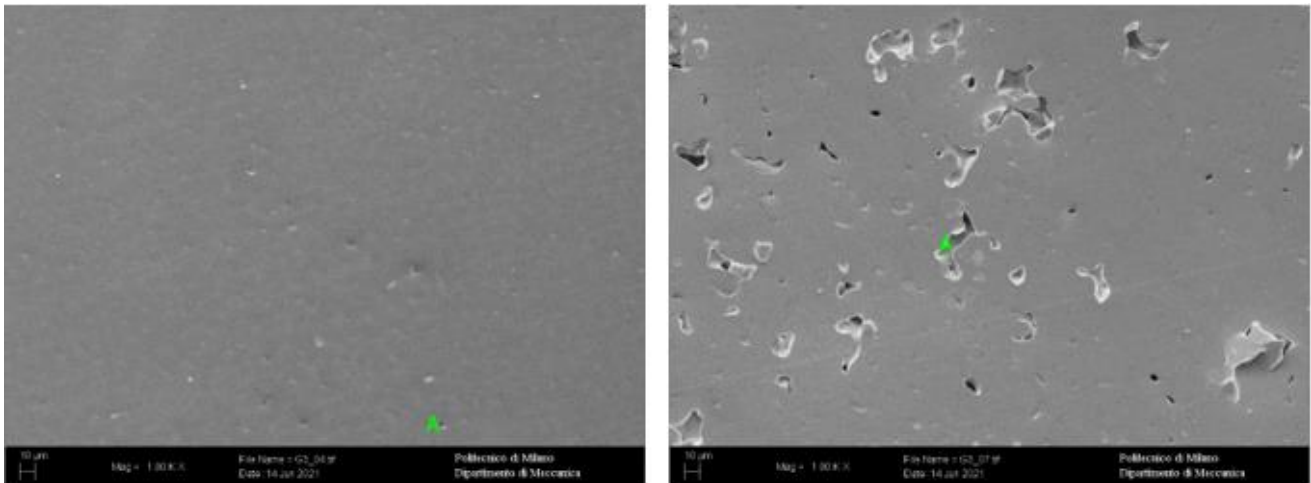
Figure 105 - SEM micrographs of specimen G2: (left) inner region and (right) irregular edge.

EDS analysis was performed on two regions of G2: in the regular inner region and in the irregular and porous edge. The results of EDS are reported in the tables below.

Table 27 - Results of EDS analysis performed on the inner region of the specimen G2.

Site of analysis	Cu (%wt)	O (%wt)	C (%wt)
A	65.18	4.26	30.56
Matrix	92.08	-	7.92

Table 28 - Results of EDS analysis performed on the irregular edge of the specimen G2.

Site of analysis	Cu (%wt)	O (%wt)	C (%wt)
A	80.01	11.58	8.41
B	92.74	2.01	5.25
Matrix	100	-	-

It is possible to conclude that G2 is also fully copper (100%), except for some impurities in the pores, which are concentrated on the edges.

The specimen G3 treated in air and inside the graphite crucible appears to have undergone a more effective densification, except for a crack, that could be caused during polishing or by an alignment of pores, as can be seen in Figure 106.
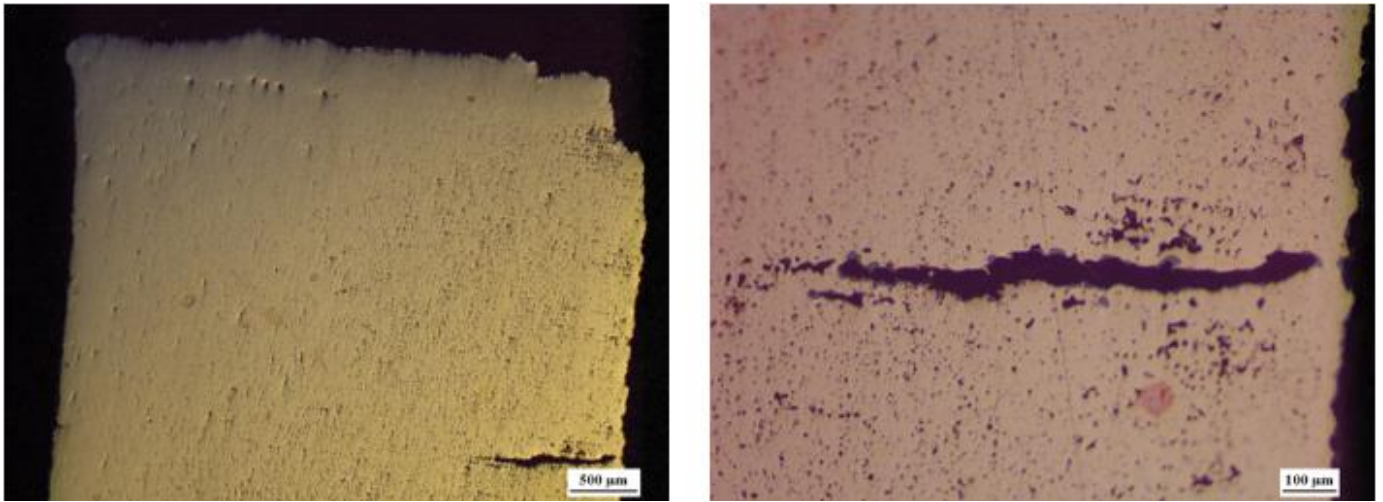
Figure 106 - Optical images of the specimen G3.

Three different EDS analysis were performed on G3: the first one on the inner region (Fig. 107 (a)), the most regular and less porous, the second one in an irregular and porous region close to the edge (Fig. 107 (b)) and the last one on the crack (Fig. 107 (c)).
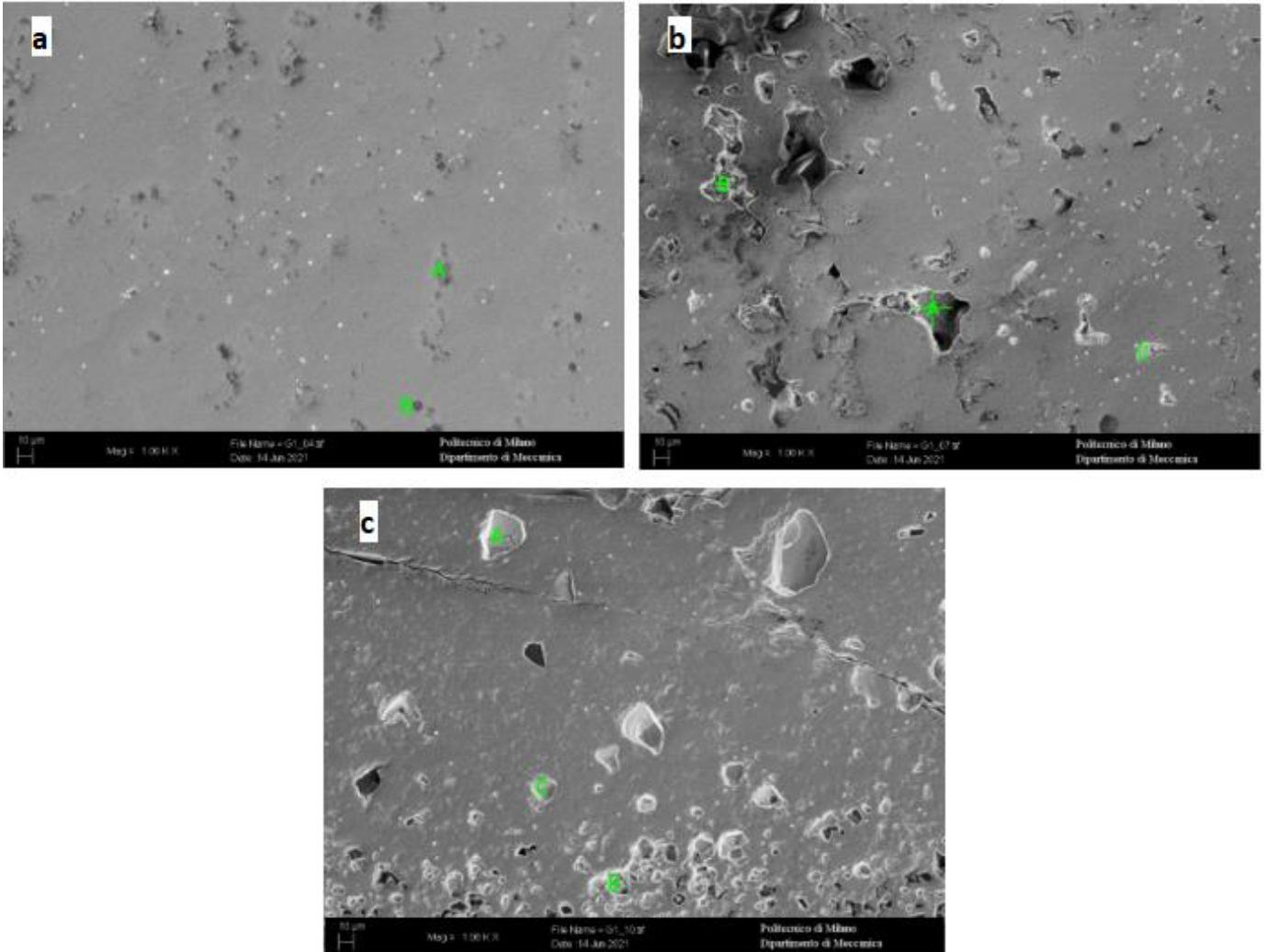The results of EDS analysis are reported in the tables below.
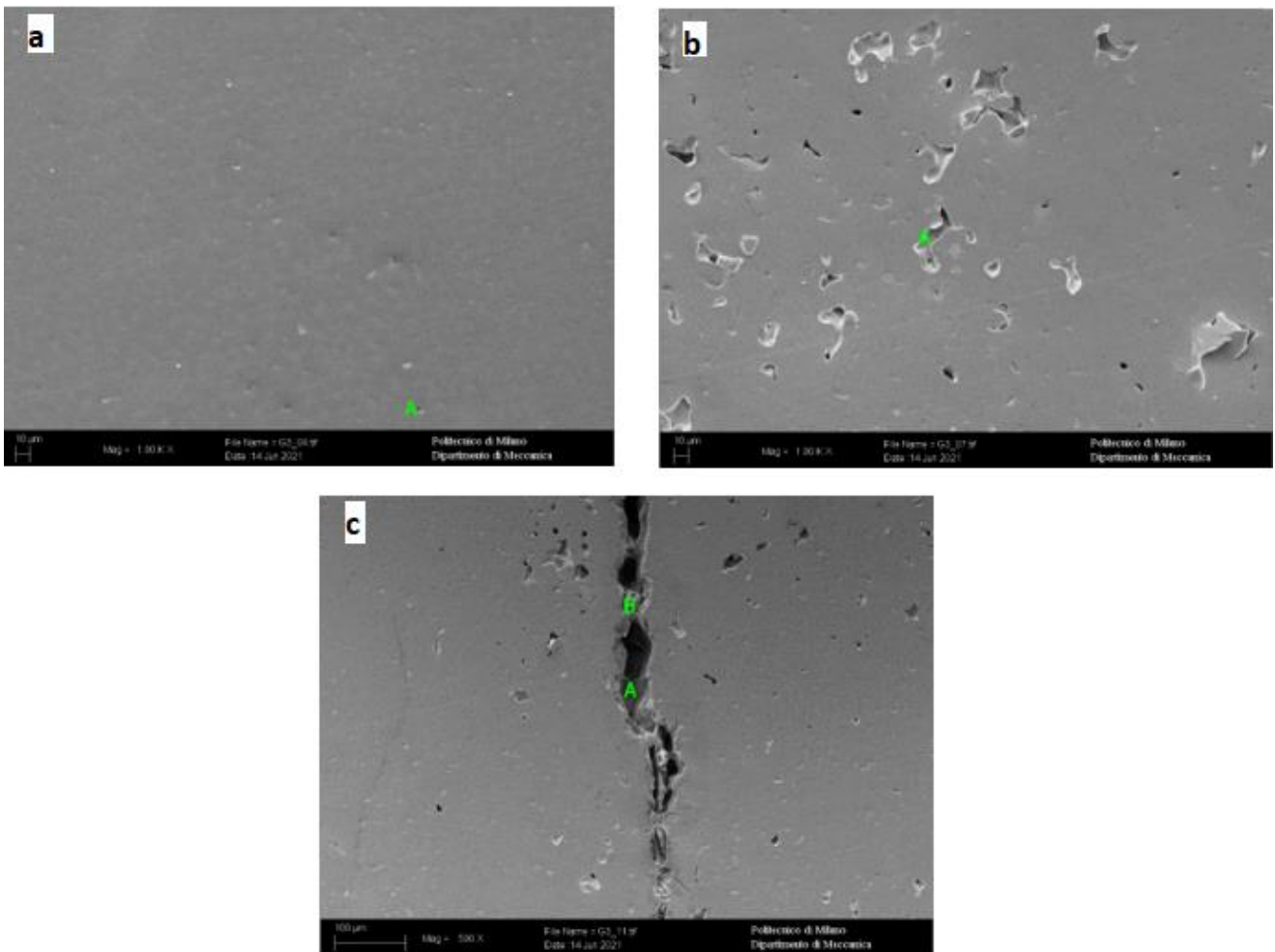
Figure 107 - SEM micrographs of the specimen G3: (a) inner region, (b) irregular region close to the edge, and (c) crack.

Table 29 - Results of EDS analysis performed on the inner region of the specimen G3.

Site of analysis	Cu (%wt)	O (%wt)	C (%wt)
A	88.92	-	11.08
Matrix	100	-	-

Table 30 - Results of EDS analysis performed on the porous region of the specimen G3.

Site of analysis	Cu (%wt)	O (%wt)	C (%wt)
A	95.29	-	4.71
Matrix	100	-	-

Table 31 - Results of EDS analysis performed on the crack of the specimen G3.

Site of analysis	Cu (%wt)	O (%wt)	C (%wt)	Ca (%wt)
A	39.22	13.75	46.32	0.71
B	42.29	6.91	50.47	0.33
Matrix	100	-	-	-

Even G3 is almost pure copper, except for some impurities in the pores, which are much less than the previous samples.

Like mentioned before, the responsible of the reduction of oxide is the carbon, in this case the graphite.
Liu et al. [66] investigated the reduction of copper oxide with graphite by performing a dry, high-energy ball-milling process. They found out that, in according with previous studies [78], when temperature is greater than 300 °C, the reduction sequence is CuO to Cu_2O to Cu. However, at low temperatures or in case of large content of carbon, the reduction is direct, going from CuO to Cu, without the formation of Cu_2O.
First of all, when the temperature is moderately high, the following reaction occurs, involving tenorite and the graphite and leading to the formation of cuprite and carbon monoxide:

$$2CuO + C \rightarrow Cu_2O + CO \tag{36}$$

Then, after the formation of CO, the following reaction occurs:

$$2CuO + CO \rightarrow Cu_2O + CO_2 \tag{37}$$

If the temperature increases significantly, reduction to metallic copper can happen:

$$2Cu_2O + C \rightarrow 4Cu + CO_2 \tag{38}$$
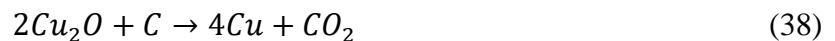
In the performed thermal treatments, in the case of the first specimen, graphite is not present, so the carbon is given only by the small amount of residual binder and for this reason the reduction of copper oxide is not complete, but a very thick oxidized crust remains, hindering the densification of the inner region.

The specimen G1, even if a piece of graphite is present, has still the oxide crust due to the fact that the tube is not perfectly sealed and some air is present inside the chamber.

To avoid the formation of a thick crust, the specimens need to be put inside a graphite crucible and covered with a piece of graphite to create a closed environment full of carbon, which reacts and acts as a reducing agent.

It is possible to affirm that 1000 °C is a suitable temperature to obtain adequate values of density, but a holding time of 3 hours is necessary to achieve sintering, as resulted from dilatometry analysis.

Air is a great atmosphere if the specimen is surrounded by graphite because it reacts with oxygen and forms carbon monoxide or carbon dioxide:

$$C + \frac{1}{2}O_2 \rightarrow CO \tag{39}$$
$$C + O_2 \rightarrow CO_2 \tag{40}$$

The formation of CO and CO_2 gives a boost to reduction of copper, consequently obtaining specimens made by pure copper and with less pores, since the presence of oxides severely hinders the densification of the part.

For this reason, it is possible to perform thermal treatments in air, which is easier and less expensive compared to inert or hydrogen atmosphere or vacuum.

Conclusions

In this work, pure copper parts were fabricated with Binder Jetting Additive Manufacturing, starting from a fine gas atomized powder, with the goal of finding the best printing parameters and the best post-processing thermal treatment in order to obtain fully density.

The printing parameters were chosen according to previous studies, varying the binder saturation and the curing time. It was found that 90% and 100% values of binder saturation are both suitable to obtain adequate values of density, while 110% gives oversaturation problems, as bad surface finishing. Regarding curing process, EDS analysis revealed that the amount of oxygen (around 2-3%) is approximately constant regardless of the curing time, meaning that 6 hours curing at 180 °C can be performed to obtain more resistant green parts.

Dilatometry experiments were performed on debinded specimens to study the sintering behavior of BJ copper parts and identify the best thermal treatment.
From these analyses, it was observed that the most significant densification process occurs in the range between 950 °C and 1000 °C and reduction of copper oxides takes place.
900 °C is not a sufficient value of temperature to achieve sintered part and a holding time at peak temperature is required even at 1050 °C, to allow the diffusion of material and to close all the remaining pores, inside of which impurities like oxide tend to accumulate.
Moreover, specimens treated in vacuum are characterized by larger densification compared to the argon-treated ones, because vacuum allows degassing of pores, while in case of argon, gases remain trapped inside the pores, slowing the densification process and promoting coalescence of pores.
The reduction of copper oxides can be attributed to the presence of residual binder in the specimen, specifically to carbon, which reacts with Cu_2O, forming CO and CO_2, reducing to metallic copper.
At moderate high temperature, Cu_2O is the only copper oxide present because CuO, also known as tenorite, decomposes completely into cuprite above 300 °C.
All the previously mentioned reduction mechanisms were confirmed with DSC and TG analysis of debinded specimen.

A first sintering treatment was performed in 50:50 H_2/N_2 atmosphere at 900 °C for 3 hours, according to literature, but the parts did not show any densification, confirming the results obtained from dilatometry analyses.
In addition, separating and performing debinding and sintering step in different atmospheres (the former in argon and the latter in vacuum) should improve the final density values.

Finally, the possibility of a sintering treatment in argon and in air in presence of graphite was investigated as alternatives to more complex and expensive procedures. If the part is placed inside a closed graphite crucible the reduction is radically enhanced, in particular in air, and sintering process is successful at 1000 °C for 3 hours.

Future studies should focus on refining the thermal treatments to guarantee higher values of density, in particular by varying conditions like temperature, holding time and atmosphere. Additionally, the effect of processing parameters and different thermal cycles on the final mechanical and physical properties, such as electrical conductivity, should be explored because they are crucial for applications like electronic devices.

References

[1] J. R. Davis, ASM Specialty Handbook: Copper and Copper Alloys, ASM International, 2001.

[2] J. Smart and A. Smith, "Effect of certain fifth-period elements on some properties of high-purity copper," in *Transactions of the Metallurgical Society of AIME, vol. 152*, p. 103.

[3] T. Massalski, "Binary Alloy Phase Diagram," ASM, 1986, p. 943.

[4] J. Zhang and W. Richardson, "Copper Compounds," in *Ullmann's Encyclopedia of Industrial Chemistry*, 2016.

[5] ASM International, Powder Metal Technologies and Applications, 1998.

[6] E. Beştek, "Powder Metallurgy Processes and Making Metal Powder," 2020.

[7] W. Brian James, "Powder Metallurgy Methods and Applications," in *ASM Handbook, vol. 7, Powder Metallurgy*, Samal, P.; Newkirk, J., 2015.

[8] F. Santos da Silva, N. Cinca, S. Dosta, I. Garcia Cano, A. Benedetti and J. Guilemany, "Cold gas spray coatings: Basic principles, corrosion protection and application," in *Eclética Química Journal, vol. 42*, 2017.

[9] Z. Fang, Sintering of Advanced Materials, Woodhead Publishing, 2010.

[10] H. E. Exner and E. Arzt, "Sintering Processes," in *Sintering Key Papers*, Dordrecht, Springer, 1990, pp. 2628-2654.

[11] F. Calignano, D. Manfredi, E. Ambrosio, S. Biamino, M. Lombardi, E. Atzeni, A. Salmi, P. Minetola, L. Iuliano and P. Fino, "Overview on Additive Manufacturing Technologies," in *Proceedings of the IEEE, vol. 105*, 2017, pp. 593-612.

[12] ISO/ASTM 52910:2018(E), Additive manufacturing — Design — Requirements.

[13] E. Herderick, "Progress in Additive Manufacturing," in *The Journal of The Minerals, Metals & Materials Society, vol. 67, no. 3*, The Minerals, Metals & Materials Society, 2015, pp. 580-581.

[14] M. Qian, "Metal Powder for Additive Manufacturing," in *The Journal of The Minerals, Metals & Materials Society, vol. 67, no. 3*, The Minerals, Metals & Materials Society, 2015, pp. 536-537.

[15] S. Babu and R. Goodridge, "Additive Manufacturing," in *Materials Science and Technology, vol. 31, no. 8*, 2015, pp. 881-883.

[16] N. Isa, N. Saude, M. Ibrahim, S. Hamid and K. Kamarudin, "A Study on Melt Flow Index on Copper-ABS for Fused Deposition Modeling (FDM) Feedstock," in *Applied Mechanics and Materials*, 2015, pp. 8-12.

[17] D. Li, D. Sutton, A. Burgess, D. Graham and P. Calvert, "Conductive copper and nickel lines via reactive inkjet printing," in *Journal of Materials Chemistry, vol. 19*, 2009.

[18] T. Öhlund, A. Mechler, M. Hummelgård, J. Bäckström, H. Nilsson and H. Olin, "Inkjet Fabrication of Copper Patterns for Flexible Electronics: Using Paper with Active Precoatings," in *ACS Applied Materials & Interfaces, vol.7*, 2015.

[19] H. Jun, E. Lee and S. Ryu, "Synthesis and characterization of copper ink and direct printing of copper patterns by inkjet printing for electronic devices," in *Current Applied Physics, vol. 20*, 2020.

[20] J. Kang, H. Kim, J. Ryu, H. Hahn, S. Jang and J. Joung, "Inkjet printed electronics using copper nanoparticle ink," in *Journal of Materials Science: Materials in Electronics, vol. 21*, 2010, pp. 1213-1220.

[21] G. Mladenov, E. Koleva, L. Koleva and V. Dzharov, "State of the art of additive manufacturing by selective electron beam melting," in *Electrotechnica & Electronica (E+E), vol. 51* , 2016, pp. 14-34.

[22] S. Jadhav, L. Goossens, Y. Kinds, B. Hooreweder and K. Vanmeensel, "Laser-based powder bed fusion additive manufacturing of pure copper," in *Additive Manufacturing, vol. 42*, 2021.

[23] W. King, H. Barth, V. Castillo, G. Gallegos, J. Gibbs, D. Hahn, C. Kamath and A. Rubenchik, "Observation of keyhole-mode laser melting in laser powder-bed fusion additive manufacturing," in *Journal of Processing Technology, vol. 214*, 2014, pp. 2915-2925.

[24] D. Tiberto, U. Klotz, F. Held and G. Wolf, "Additive manufacturing of copper alloys: influence of process parameters and alloying elements," in *Materials Science and Technology, vol. 35*, 2019, pp. 969-977.

[25] R. Guschlbauer, S. Momeni, F. Osmanlic and C. Körner, "Process development of 99.95% pure copper processed via selective electron beam melting and its mechanical and physical properties," in *Materials Characterization, vol. 143*, 2018.

[26] J. Gardan, "Additive manufacturing technologies: state of the art and trends," in *International Journal of Production Research*, 2015, pp. 3118-3132.

[27] S. Yadav, C. Paul, A. Jinoop, A. Rai and K. Bindra, "Laser Directed Energy Deposition based Additive Manufacturing of Copper: Process Development and Material Characterizations," in *Journal of Manufacturing Processes, vol. 58*, 2020, pp. 984-997.

[28] Y. Hagedorn, "Laser additive manufacturing of ceramic components: Materials, processes and mechanisms," in *Laser Additive Manufacturing*, 2017, pp. 163-180.

[29] A. Mostafaei, A. Elliott, J. Barnes, F. Li, W. Tan, C. Cramer, P. Nandwana and M. Chmielus, "Binder jet 3D printing—Process parameters, materials, properties, modeling, and challenges," in *Progress in Material Science*, 2020.

[30] S. Mirzababaei and S. Pasebani, "A Review on Binder Jet Additive Manufacturing of 316L Stainless Steel," in *Journal of Manufacturing and Materials Processing, 3(3), 82*, 2019.

[31] "B243 – 19, Standard Terminology of Powder Metallurgy".

[32] M. Li, W. Du, A. Elwany, Z. Pei and C. Ma, "Metal Binder Jetting Additive Manufacturing: A Literature Review," in *Journal of Manufacturing Science and Engineering, vol. 142*, American Society of Mechanical Engineers, 2020.

[33] A. Lores, N. Azurmendi, I. Agote and E. Zuza, "A review on recent developments in binder jetting metal additive manufacturing: materials and process characteristics," in *Powder Metallurgy, vol. 62, no. 5*, 2019, pp. 267-296.

[34] Y. Bai and C. Williams, "An exploration of binder jetting of copper," *Rapid Prototyping Journal,* vol. 21, pp. 177-185, 2015.

[35] H. Miyanaji, D. Ma, M. Atwater, K. Darling, V. Hammond and C. Williams, "Binder jetting additive manufacturing of copper foam structures," 2019.

[36] A. Kumar, J. Wang, Y. Bai, S. Huxtable and C. Williams, "Impacts of process-induced porosity on material properties of copper made by binder jetting additive manufacturing," 2019.

[37] A. Averardi, C. Cola, S. Zeltmann and N. Gupta, "Effect of particle size distribution on the packing of powder beds: A critical discussion relevant to additive manufacturing," in *Materials Today Communications, vol. 24*, 2020.

[38] H. Miyanaji, K. Rahman, D. Ma and C. Williams, "Effect of fine powder particles on quality of binder

jetting parts," 2020.

[39] Y. Bai, G. Wagner and C. Williams, "Effect of Particle Size Distribution on Powder Packing and Sintering in Binder Jetting Additive Manufacturing of Metals.," in *Journal of Manufacturing Science and Engineering, vol. 139, no. 8*, 2017.

[40] Y. Bai and C. Williams, "Binder jetting additive manufacturing with a particle-free metal ink as a binder precursor," *Materials & Design,* vol. 147, pp. 146-156, 2018.

[41] M. Ziaee and N. Crane, "Binder jetting: A review of process, materials, and methods," in *Additive Manufacturing, vol. 28*, 2019, pp. 781-801.

[42] B. Derby, "Inkjet Printing of Functional and Structural Materials: Fluid Property Requirements, Feature Stability and Resolution," in *Annual Review of Materials Research, vol. 40*, 2010, pp. 395-414.

[43] Y. Bai and C. Williams, "The effect of inkjetted nanoparticles on metal part properties in binder jetting additive manufacturing," in *Nanotechnology, vol. 29, no. 39*, 2018.

[44] Y. Bai, C. Wall, H. Pham, A. Esker and C. Williams, "Characterizing Binder–Powder Interaction in Binder Jetting Additive Manufacturing Via Sessile Drop Goniometry," in *Journal of Manufacturing Science and Engineering, vol. 141*, 2018.

[45] K. Hapgood, J. Litster, S. Biggs and T. Howes, "Drop penetration into porous powder beds," in *Journal of Colloid and Interface Science, vol. 253*, 2002.

[46] H. Chen and Y. Zhao, "Process parameters optimization for improving surface quality and manufacturing accuracy of binder jetting additive manufacturing process," *Rapid Prototyping Journal,* vol. 22, pp. 527-538, 2016.

[47] M. Vaezi and K. Chua, "Effects of layer thickness and binder saturation level parameters on 3D printing process," in *The International Journal of Advanced Manufacturing Technology, vol. 53*, 2011, pp. 275-284.

[48] H. Miyanaji and L. Yang, "Equilibrium Saturation in Binder Jetting 3D Printing Process: Theoretical Model vs. Experimental Observations," 2016.

[49] H. Miyanaji, S. Zhang and L. Yang, "A new physics-based model for equilibrium saturation determination in binder jetting additive manufacturing process," in *International Journal of Machine Tools and Manufacture, vol. 124*, 2017.

[50] H. Miyanaji, N. Momenzadeh and L. Yang, "Effect of printing speed on quality of printed parts in Binder Jetting Process," in *Additive Manufacturing, vol. 20*, 2017.

[51] J. Benson and E. Snyders, "The need for powder characterisation in the additive manufacturing industry and the establishment of a national facility," in *The South African Journal of Industrial Engineering, vol. 26*, 2015.

[52] A. Strondl, O. Lyckfeldt, H. Brodin and U. Ackelid, "Characterization and Control of Powder Properties for Additive Manufacturing," in *The Journal of the Minerals, vol. 67*, Metals & Materials Society, 2015, pp. 549-554.

[53] K. Higashitani, H. Makino and S. Matsusaka, Powder Technology Handbook, Fourth Edition, Taylor & Francis Group, 2020.

[54] K. Luke and A. Silva, "Advanced in Particle Characterization - Benefits and Applications," in *35th International Conference on Cement Microscopy*, 2013.

[55] E. Olson, "Particle Shape Factors and Their Use in Image Analysis," in *Journal of GXP Compliance*, 2011,

vol. 15, n. 3, pp. 85-96.

[56] Y. Sun, S. Gulizia, C. Oh, C. Doblim, Y. Yang and M. Qian, "Manipulation and Characterization of a Novel Titanium Powder Precursor for Additive Manufacturing Applications," in *The Journal of the Minerals*, Metals & Materials Society, 2015.

[57] M. Li, W. Du, A. Elwany, Z. Pei and C. Ma, "Metal Binder Jetting Additive Manufacturing: A Literature Review," in *Journal of Manufacturing Science and Engineering, vol. 142*, American Society of Mechanical Engineers, 2020.

[58] Setaram, "Labsys evo".

[59] Linseis, "Dilatometry. DIL L76. DIL L75 PT Horizontal. DIL L75 PT Vertical.," in *https://www.linseis.com/wp-content/uploads/2020/09/Linseis-Dilatometer-Vertical-and-Horizontal-Analyzer-v7.pdf*.

[60] T. Khasanshin and A. Aleksandrov, "Thermodynamic properties of ethanol at atmospheric pressure," in *Journal of engineering physics, vol. 47*, 1984, pp. 1046-1052.

[61] M. Eslami, F. Golestani-Fard, H. Saghafian and A. Robin, "Study on tribological behavior of electrodeposited Cu-Si3N4 composite coatings," in *Materials and Design*, 2014.

[62] M. Kooti, "Fabrication of Nanosized Cuprous Oxide Using Fehling's Solution," in *Scientia Iranica*, 2010.

[63] S. Sathyanathan, S. Karthikeyan and K. Jayamoorthy, "FTIR and multivariate analysis to study the effect of bulk and nano copper oxide on peanut plant leaves," in *Journal of Science: Advanced Materials and Devices, vol. 1*, 2016.

[64] S. Choudhary, J. Sarma, S. Pande, S. Ababou-Girard, P. Turban, B. Lepine and S. Gangopadhyay, "Oxidation mechanism of thin Cu films: A gateway towards the formation of single oxide phase," in *AIP Advances 8*, 2018.

[65] N. Raship, M. Sahdan, F. Adriyanto, M. Nurfazliana and A. Bakri, "Effect of annealing temperature on the properties of copper oxide films prepared by dip coating technique," in *AIP Conference Proceedings 1788*, 2017.

[66] L. Liu, T. Zhang, K. Cui and Y. Dong, "Reduction of copper oxide with graphite by mechanical alloying," in *Journal of Materials Research, vol.14*, 1999, pp. 4062-4069.

[67] K. Tokumitsu, "Reduction of metal oxides by mechanical alloying method," in *Solid State Ionics*, 1997, pp. 25-31.

[68] V. Belousov and A. Klimashin, "High-temperature oxidation of copper," in *Russian Chemical Reviews, vol. 82*, 2013.

[69] J. Mittal and K. Lin, "Exothermic low temperature sintering of Cu nanoparticles," in *Materials Characterization*, 2015, vol. 109, pp. 19-24.

[70] K. Wang and R. Reeber, "Thermal Expansion of Copper," in *High Temperature and Materials Science, vol. 35*, 1996, pp. 181-186.

[71] E. Wheat, G. Shanbhag and M. Vlasea, "The Master Sinter Curve and Its Application to Binder Jetting Additive Manufacturing," in *Journal of Manufacturing Science and Engineering, vol. 142*, 2020, pp. 1-37.

[72] S. Johnston, D. Frame, R. Anderson and D. Storti, "Strain Analysis of Initial Stage Sintering of 316L SS Three Dimensionally Printed Components," in *Internation Solid Freeform Fabrication Symposium*, 2004.

[73] S. Lee, N. Mettlach, N. Nguyen, Y. Sun and J. White, "Copper oxide reduction through vacuum

annealing," in *Applied Surface Science, vol. 206*, 2002, pp. 102-109.

[74] H. Juan, "Effect of Temperature Ratio (ts/tm) and Time on the Sintering Behavior of Metallic 316L Stainless Steel Coupons Produced Using Jet-Binder Technology".

[75] J. Lewis, "The Reduction of Copper Oxide by Hydrogen," in *Journal of Chemical Society*, 1932.

[76] R. Pease and H. Taylor, "Reduction of cupric oxide by hydrogen," in *Journal of the American Chemical Society*, 1921.

[77] Y. Champion, F. Bernard, N. Millot and P. Perriat, "Sintering of copper nanopowders under hydrogen: An in situ X-ray diffraction analysis," in *Materials Science and Engineering: A, vol. 360*, 2003, pp. 258-263.

[78] E. Goldstein and R. Mitchell, "Chemical kinetics of copper oxide reduction with carbon monoxide," in *Proceedings of the Combustion Institute, vol. 33*, 2011, pp. 2803-2810.

[79] A. Clearfield, J. Reibenspies and N. Bhuvanesh, "Principles and applications of powder diffraction," John Wiley and Sons, Ltd., 2008.